

# Lawrence Berkeley National Laboratory

## Recent Work

### Title

Physics of Laser-driven plasma-based acceleration

### Permalink

<https://escholarship.org/uc/item/3rx3c289>

### Authors

Esarey, Eric  
Schroeder, Carl B.

### Publication Date

2003-06-30

# Physics of Laser-Driven Plasma-Based Accelerators

Eric Esarey and Carl B. Schroeder

*Center for Beam Physics, Accelerator and Fusion Research Division,  
Ernest Orlando Lawrence Berkeley National Laboratory, University of California, Berkeley, CA 94720*  
(Dated: June 30, 2003)

The physics of plasma-based accelerators driven by short-pulse lasers is reviewed. This includes the laser wakefield accelerator, the plasma beat wave accelerator, the self-modulated laser wakefield accelerator, and plasma waves driven by multiple laser pulses. The properties of linear and nonlinear plasma waves are discussed, as well as electron acceleration in plasma waves. Methods for injecting and trapping plasma electrons in plasma waves are also discussed. Limits to the electron energy gain are summarized, including laser pulse diffraction, electron dephasing, laser pulse energy depletion, as well as beam loading limitations. The basic physics of laser pulse evolution in underdense plasmas is also reviewed. This includes the propagation, self-focusing, and guiding of laser pulses in uniform plasmas and plasmas with preformed density channels. Instabilities relevant to intense short-pulse laser-plasma interactions, such as Raman, self-modulation, and hose instabilities, are discussed. Recent experimental results are summarized.

## I. INTRODUCTION

Laser-driven plasma-based accelerators were originally proposed by Tajima and Dawson in 1979 [1]. John Dawson, the father of plasma-based accelerators, who passed away in 2001, was responsible for many of the key developments in this field, including the plasma beat wave accelerator, the laser wakefield accelerator, and the photon accelerator [1–3]. In addition, he was one of the early pioneers of particle-in-cell simulation of plasmas [4–6], which is now an important tool in the study of plasma-based accelerators. During his lifetime, the field of plasma-based accelerators has grown into a world-wide research effort with ongoing experimental programs in France, Germany, Japan, the UK, and the United States, to name a few [7]. Much of this growth is due to the rapid development of chirp-pulse amplification (CPA) laser technology, pioneered by G. Mourou and his colleagues [8–10], making readily available compact sources of intense, high power, ultrashort laser pulses.

Plasma-based accelerators are of great interest because of their ability to sustain extremely large acceleration gradients. The accelerating gradients in conventional radio-frequency linear accelerators (linacs) are currently limited to roughly 100 MV/m, partly due to breakdown that occurs on the walls of the structure. Ionized plasmas, however, can sustain electron plasma waves with electric fields in excess of the nonrelativistic wavebreaking field [11]  $E_0 = cm_e\omega_p/e$ , or

$$E_0(\text{V/m}) \simeq 96\sqrt{n_0(\text{cm}^{-3})}, \quad (1)$$

where  $\omega_p = (4\pi n_0 e^2/m_e)^{1/2}$  is the electron plasma frequency,  $n_0$  is the ambient electron number density,  $m_e$  and  $e$  are the electron rest mass and charge, respectively, and  $c$  is the speed of light in vacuum. For example, a plasma density of  $n_0 = 10^{18} \text{ cm}^{-3}$  yields  $E_0 \simeq 100 \text{ GV/m}$ , which is approximately three orders of magnitude greater than that obtained in conventional linacs. Accelerating gradients on the order of 100 GV/m

have been inferred in plasma-based accelerator experiments [12, 13].

In addition to extremely large accelerating gradients, plasma-based accelerators have the potential to produce extremely short electron bunches. The length of the accelerating wave in a plasma-based accelerator is approximately the plasma wavelength  $\lambda_p = 2\pi c/\omega_p = 2\pi/k_p$ , or

$$\lambda_p(\mu\text{m}) \simeq 3.3 \times 10^{10}/\sqrt{n_0(\text{cm}^{-3})}, \quad (2)$$

e.g.,  $\lambda_p \simeq 30 \mu\text{m}$  for  $n_0 = 10^{18} \text{ cm}^{-3}$ . A high-quality electron bunch produced by a plasma-based accelerator would have a bunch duration  $\tau_b < \lambda_p/c$ , i.e., a duration  $\tau_b < 100 \text{ fs}$  for  $n_0 = 10^{18} \text{ cm}^{-3}$ . Laser-driven, plasma-based accelerators, which are typically driven by femtosecond laser pulses, are intrinsically sources of femtosecond electron bunches.

An important parameter in the discussion of intense laser-plasma interactions is the laser strength parameter  $a_0$ , defined as the peak amplitude of the normalized vector potential of the laser field,  $\mathbf{a} = e\mathbf{A}/m_e c^2$ . The laser strength parameter is related to the peak intensity  $I_0$  and power  $P = \pi r_0^2 I_0/2$  by  $I_0 = (\pi c/2)(m_e c^2 a_0/e\lambda)^2$ , which yields

$$a_0^2 \simeq 7.3 \times 10^{-19} [\lambda(\mu\text{m})]^2 I_0(\text{W/cm}^2), \quad (3)$$

and  $P(\text{GW}) \simeq 21.5(a_0 r_0/\lambda)^2$ , where a linearly polarized laser field with a Gaussian radial profile is assumed, e.g.,  $\mathbf{a} = a_0 \exp(-r^2/r_0^2) \cos(kz - \omega t) \mathbf{e}_x$  with  $r_0$  the laser spot size at focus,  $\lambda = 2\pi/k$  the laser wavelength, and  $\omega = ck$  the laser frequency in vacuum. Furthermore, the peak laser electric field amplitude is given by  $E_L = m_e c \omega a_0/e$ , i.e.,  $E_L(\text{TV/m}) \simeq 3.21 a_0/\lambda(\mu\text{m})$ . Physically,  $\mathbf{a} = \mathbf{p}_\perp/m_e c$  is the normalized transverse “quiver” momentum of a plasma electron in the laser field, as indicated by conservation of transverse canonical momentum in the one-dimensional (1D) limit ( $r_0 \gg \lambda$ ). When  $a_0 \gtrsim 1$ , the electron quiver motion is highly relativistic and the laser-plasma interaction is nonlinear. Highly

relativistic electron motion ( $a_0 \gtrsim 1$ ) requires laser intensities  $I \gtrsim 10^{18} \text{ W/cm}^2$  for wavelengths of  $\lambda \simeq 1 \mu\text{m}$ . Such intensities are routinely produced by compact, solid-state laser systems based on the technique of CPA.

The laser acceleration of electrons in vacuum and gases is intrinsically limited by diffraction, electron slippage, ionization, and the smallness of the laser wavelength [14, 15]. In vacuum, the motion of an electron in a laser field is determined by the Lorentz force equation

$$d\mathbf{u}/dct = \partial\mathbf{a}/\partial ct - (\mathbf{u}/\gamma) \times (\nabla \times \mathbf{a}), \quad (4)$$

where  $\mathbf{u} = \mathbf{p}/m_e c$  is the normalized electron momentum and  $\gamma = (1 + u^2)^{1/2}$  is the relativistic Lorentz factor. Roughly speaking, the first term on the right-hand side of the above equation describes the linear response of the electron to the electric field  $\mathbf{E}$  of the laser and is responsible for “direct” laser acceleration; whereas the second term describes the nonlinear response to the  $\mathbf{v} \times \mathbf{B}$  force and is responsible for “ponderomotive” laser acceleration. Typically, the axial (in the  $z$ -direction of laser propagation) ponderomotive force is written as  $F_{pz} \simeq -(m_e c^2/\gamma)(\partial/\partial z)a^2/2$ , assuming  $\mathbf{u}_\perp = \mathbf{a}_\perp$ , which is exact in 1D.

When a laser field propagating along the  $z$ -axis is focused in vacuum, the laser spot size and intensity evolve via  $r_s = r_0(1 + z^2/Z_R^2)^{1/2}$  and  $I = I_0(r_0^2/r_s^2) \exp(-2r^2/r_s^2)$ , respectively, where  $Z_R = kr_0^2/2$  is the Rayleigh length, and a fundamental Gaussian mode is assumed. The finite laser spot size implies the existence of an axial component of the electric field of the laser via  $\nabla \cdot \mathbf{E} = 0$ , i.e.,  $E_z \sim (1/kr_0)E_\perp$ . The amplitude of this axial field can be very large, which suggests using the axial field directly for laser acceleration, with an energy gain for an electron propagating along the axis scaling as  $\int dz(v_z E_z)$ . The phase velocity, however, of the optical field along the axis is greater than  $c$  and is approximately  $v_p/c \simeq 1 + 1/(kZ_R)$  near the focus. Since  $v_p > c$ , electrons with  $v_z \lesssim c$  will phase slip with respect to the accelerating field and decelerate. This will occur over a dephasing length  $L_d$ , which for highly relativistic electrons is  $\sim Z_R$ , i.e., the dephasing length is on order of the diffraction length.

This phase slippage argument forms the basis for the so-called Lawson-Woodward (LW) theorem [16–18], which states that under certain restrictive conditions no net electron energy gain is possible using laser fields. The LW theorem assumes (i) the region of interaction is infinite, (ii) the laser fields are in vacuum with no walls or boundaries present, (iii) the electron is highly relativistic ( $v_z \simeq c$ ) along the acceleration path, (iv) no static electric or magnetic fields are present, and (v) nonlinear effects (e.g., ponderomotive,  $\mathbf{v} \times \mathbf{B}$ , and radiation reaction forces) are neglected.

One or more of the assumptions of LW theorem must be violated in order to achieve a nonzero net energy gain. For example, one can introduce optics to limit the laser-electron interaction to approximately a region of length  $2Z_R$  about the focus, such that minimal phase

slippage occurs [14, 19]. The maximum energy gain due to direct acceleration by the  $E_z$  field is then given by  $\Delta W(\text{MeV}) \simeq 31\sqrt{P(\text{TW})}$ , where a first-order Laguerre-Gaussian mode has been assumed [14]. Although substantial energy gains are possible with high laser power, this is problematic in practice, since this method requires that optics be placed near the focus and are susceptible to laser damage at high intensity. Furthermore, the electron beam must pass through a small aperture in the optics, which can limit the amount of charge that can be accelerated [15].

Alternatively, finite energy gains can be achieved by introducing a background of gas into the interaction region, as in the inverse Cherenkov accelerator [20]. The gas can reduce the phase velocity of the laser field to less than  $c$ , reducing the slippage. Furthermore, in principle, diffraction can be overcome by relying on optical guiding (self-focusing) in the gas [21]. Nevertheless, ionization of the gas, which occurs at a relatively low laser intensity  $\sim 10^{14} \text{ W/cm}^2$  and increases the phase velocity, remains a fundamental limitation to the accelerating field in gas-filled devices.

In addition to direct laser acceleration, finite energy gains can also result from the nonlinear or ponderomotive force. Since the ponderomotive force scales inversely with electron energy and proportional to the laser intensity,  $F_p \sim (1/\gamma)\nabla a^2$ , this mechanism is most efficient at low electron energies and high laser intensities. Simulations [22, 23] and experiments [24] have shown that by focusing a high intensity laser pulse onto a low density gas jet (essentially, a source of electrons at rest), ponderomotive acceleration can result in the production of a electrons with energies in the range of a few MeV with a large energy spread and a high degree of scattering. Simulations [25] indicate that when a moderate energy electron beam intersects with a very intense laser pulse at a small angle, a significant fraction of the electrons can be accelerated to energies in excess of 100 MeV (for  $a \sim 10$ ) through a combination of direct and ponderomotive acceleration. Other ponderomotive acceleration schemes include the vacuum beat wave accelerator [14], which relies on the ponderomotive force of the beat wave produced by two co-propagating laser pulses, and the inverse free-electron laser [26, 27], which relies on the beat wave produced by a laser pulse propagating through a magnetic wiggler field. Again, a major limitation to these schemes is the  $1/\gamma$  scaling of ponderomotive force.

A fundamental limitation to all concepts that rely on electron acceleration through the direct interaction (linear or nonlinear) with the laser field is the smallness of the laser wavelength, typically on the order of a micron. For example, a first-order Laguerre-Gaussian mode has a quarter wavelength phase region for which the laser field is both accelerating and focusing. To accelerate an electron bunch while maintaining a small energy spread and emittance, it is desirable that a high quality bunch be injected into the proper phase region of the laser field with a bunch length small compared to a  $\lambda/4$  (corresponding

to 0.8 fs for  $\lambda = 1\ \mu\text{m}$ ). Conventional accelerators typically produce electron bunches with durations  $\gtrsim 1$  ps. On possibility may be to pre-bunch a conventional electron bunch at the laser wavelength using an inverse free-electron laser, as has been experimentally demonstrated [26], and use this as an injector into a second stage of a laser accelerator [27].

Plasma-based accelerators can overcome many of the fundamental limitations that restrict laser acceleration in vacuum and gases. For example, ionization and breakdown is not a limitation, since the plasma can be fully pre-ionized. Diffraction can be overcome through self-focusing and with preformed plasma channels. In plasma-based accelerators, acceleration is the result of the axial field of the plasma wave and not the laser field directly. The phase velocity of the plasma wave is typically equal to the group velocity of the laser pulse and is less than  $c$ . Although the plasma wave is excited by the ponderomotive force of the laser field, the  $1/\gamma$  scaling of the ponderomotive force is not a limitation, since for the plasma electrons  $\gamma \sim 1$ . In effect, the plasma acts as a transformer, converting the transverse laser field into the axial electric field of the plasma wave. Furthermore, the accelerating wavelength is the plasma wavelength  $\lambda_p$ , which is 10–1000 times the laser wavelength, and in many cases equal to the laser pulse length. The injection of ultrashort electron bunches into a single period of a plasma wave maybe possible using laser injection methods. Plasma-based methods are, however, subject to their own intrinsic limitations, such as restrictions arising from electron dephasing, pump depletion, and laser-plasma instabilities.

This report provides an overview of the physics and issues relevant to laser-driven plasma-based accelerators, including the plasma beat wave accelerator (PBWA) [1, 2, 28–31], the laser wakefield accelerator (LWFA) [1, 32–35], the self-modulated LWFA [12, 36–45], and LWFA driven by multiple laser pulses [46–50]. These configurations are shown schematically in Fig. 1. The remainder of this report is organized as follows. Section II discusses the basic models used to describe plasma wave generation in the cold fluid limit. Included is a discussion of nonlinear plasma waves, wavebreaking, and plasma wave phase velocity, as well as the trapping and acceleration of electrons by the plasma wave. Section III describes the various laser-driven plasma-based acceleration configurations, specifically, the LWFA, the PBWA, the self-modulated LWFA, and wakefields driven by multiple pulses. Included is a brief discussion of diffraction, dephasing, and pump depletion, which can limit the single-stage energy gain. The injection of ultrashort electron bunches into plasma waves using laser triggered injection or density gradients is discussed in Sect. IV. Methods for optically guiding laser pulses in plasmas are discussed in Sect. V, including relativistic self-focusing, preformed density channels, ponderomotive self-channel, and plasma wave effects. Section VI describes a few of the more relevant laser-plasma instabilities, including back-

ward and forward Raman scattering, self-modulation, and laser-hosing. Throughout this report recent experimental results are mentioned. A summary is presented in Sect. VII.

## II. PLASMA WAVES AND ACCELERATION

Calculation of the plasma wakefields generated by nonevolving drive laser beams is straightforward. Analytical solutions exist in the three-dimensional (3D) linear regime and in the 1D nonlinear regime. In the 3D nonlinear regime, the use of numerical codes is usually required. The full problem, which includes the self-consistent evolution of the drive laser beams, is sufficiently complicated to require simulation. Various aspects of the propagation and transport of the drive beams will be discussed in subsequent sections. Before discussing specific laser-plasma-based accelerator configurations (e.g., PBWA, LWFA, self-modulated LWFA, and wakefields driven by multiple pulses), the physical forces that drive wakefields (i.e., space charge and ponderomotive forces) and the mathematical models used to describe wakefield generation will be briefly discussed. In the following, it is convenient to use the normalized electrostatic  $\phi = e\Phi/m_e c^2$  and vector  $\mathbf{a} = e\mathbf{A}/m_e c^2$  potentials.

### A. Ponderomotive Force

In laser-driven plasma-based accelerators, wakefields are driven via the ponderomotive force. The ponderomotive force [51] can be derived by considering the electron momentum equation in the cold fluid limit,

$$d\mathbf{p}/dt = -e[\mathbf{E} + (\mathbf{v} \times \mathbf{B})/c], \quad (5)$$

where  $d/dt = \partial/\partial t + (\mathbf{v} \cdot \nabla)$ . The electric and magnetic fields of the laser can be written as  $\mathbf{E} = -\partial\mathbf{A}/\partial ct$  and  $\mathbf{B} = \nabla \times \mathbf{A}$ , where the vector potential of the laser is polarized predominately in the transverse direction, e.g.,  $\mathbf{A} = A_0 \cos(kz - \omega t)\mathbf{e}_\perp$ . In the linear limit  $|a| = e|A|/m_e c^2 \ll 1$ , the leading order electron motion is the quiver momentum  $\mathbf{p}_q = m_e c \mathbf{a}$ , as indicated by  $\partial\mathbf{p}_q/\partial t = -e\mathbf{E}$ . Letting  $\mathbf{p} = \mathbf{p}_q + \delta\mathbf{p}$ , the second order motion is given by

$$\begin{aligned} d\delta\mathbf{p}/dt &= -[(\mathbf{p}_q/m_e) \cdot \nabla]\mathbf{p}_q - \mathbf{p}_q \times (c\nabla \times \mathbf{a}) \\ &= -m_e c^2 \nabla(a^2/2). \end{aligned} \quad (6)$$

Hence,  $\mathbf{F}_p = -m_e c^2 \nabla(a^2/2)$  is the 3D ponderomotive force in the linear limit ( $a^2 \ll 1$ ). The ponderomotive force can also be viewed as the radiation pressure (i.e., the gradient of the electromagnetic energy density).

In the 1D nonlinear regime, conservation of canonical momentum implies  $\mathbf{u}_\perp = \mathbf{a}_\perp$ , i.e.,  $\mathbf{a}_\perp$  is the normalized quiver momentum. Hence, in 1D, the nonlinear ponderomotive force is given by  $F_{pz} = -(m_e c^2/2\gamma)\partial a_\perp^2/\partial z$ . In

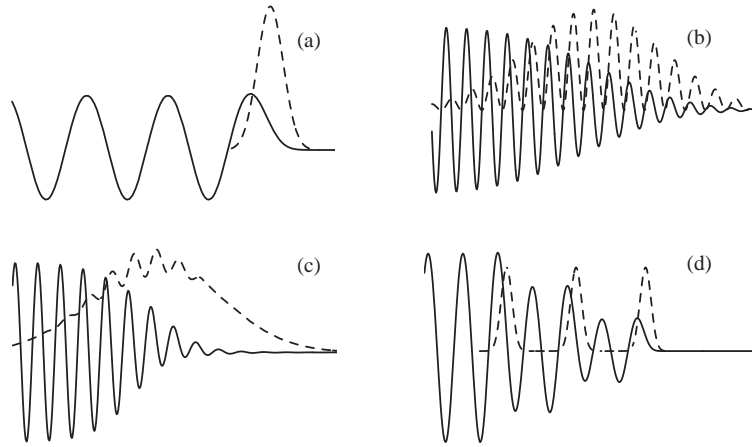


FIG. 1: Schematic of laser-driven plasma-based accelerators: (a) laser wakefield accelerator (LWFA), (b) plasma beat wave accelerator (PBWA), (c) self-modulated laser wakefield accelerator (SM-LWFA), and (d) resonant laser pulse train. Shown are the excited plasma wave potentials (*solid lines*) and right-moving laser intensity envelopes (*dashed lines*)

the 3D nonlinear regime, the leading order transverse motion of the electron is still the quiver motion,  $\mathbf{u}_\perp \simeq \mathbf{a}_\perp$ , provided that the laser pulse is propagating in an underdense plasma and has a sufficiently broad spot size,  $r_0 \gtrsim \lambda_p \gg \lambda$ . Defining  $\delta\mathbf{u} = \mathbf{u} - \mathbf{a}$ , the fluid momentum equation can be written as [36, 52, 53]

$$\partial\delta\mathbf{u}/\partial ct = \nabla(\phi - \gamma), \quad (7)$$

which is exact under the assumption that the quantity  $\nabla \times \delta\mathbf{u}$  is initially (prior to the passage of the laser pulse) zero. Here,  $\nabla\phi$  is the space-charge force and  $\nabla\gamma$  represents the generalized nonlinear ponderomotive force,  $\mathbf{F}_{pN} = -m_e c^2 \nabla\gamma$ .

### B. Linear Regime

In the linear, 3D regime, wakefield generation can be examined using the cold fluid equations, i.e., the Poisson equation, the continuity equation, and the fluid momentum equation. For example, the plasma wave generated in an initially uniform plasma is described by [32, 33, 54]

$$(\partial^2/\partial t^2 + \omega_p^2) \delta n/n_0 = c^2 \nabla^2 a^2/2, \quad (8)$$

$$(\partial^2/\partial t^2 + \omega_p^2) \phi = \omega_p^2 a^2/2, \quad (9)$$

where  $\delta n/n_0$  is the normalized density perturbation associated with the electrostatic wake  $\phi$  in the limit  $a^2 \ll 1$ . The solutions for the density perturbation ( $|\delta n/n_0| \ll 1$ ) and electric field of the wake are given by

$$\delta n/n_0 = (c^2/\omega_p) \int_0^t dt' \sin \omega_p(t-t') \nabla^2 a^2(\mathbf{r}, t')/2, \quad (10)$$

$$\mathbf{E}/E_0 = -c \int_0^t dt' \sin \omega_p(t-t') \nabla a^2(\mathbf{r}, t'). \quad (11)$$

Equations (10) and (11) describe plasma waves generated at the frequency  $\omega_p$  and are valid far from wavebreaking,  $E \ll E_0$ , where  $E_0 = m_e c \omega_p / e$  is the cold nonrelativistic wavebreaking field (1). Solutions to (10) indicate that wakefields will be generated most efficiently when the envelope scale length, which characterizes the axial gradient in the normalized laser intensity  $a^2$ , is on the order of the plasma wavelength  $\lambda_p = 2\pi c/\omega_p$ . The radial extent of the wake is on the order of the laser spot size  $r_s$ .

In addition to the axial wakefield  $E_z$ , transverse wakefields  $E_r$  and  $B_\theta$  will be generated. The transverse wakefields are related to the axial wakefield by the Panofsky-Wenzel theorem [55, 56],  $\partial E_z/\partial r = \partial(E_r - B_\theta)/\partial(z - ct)$ . A relativistic particle with axial velocity  $v_z \simeq c$  which is being accelerated by a wakefield with phase velocity  $v_p \simeq c$  will experience a radial force proportional to  $E_r - B_\theta$ . Notice that if  $E_z \sim \exp(-2r^2/r_s^2) \cos[k_p(z - ct)]$ , then  $E_r - B_\theta \sim (4r/k_p r_s^2) \exp(-2r^2/r_s^2) \sin[k_p(z - ct)]$  and the radial force is zero along the axis. Typically, for an electron displaced from the axis, there is a phase region of the wake of width  $k_p |\Delta(z - ct)| = \pi/4$  for which a relativistic electron will experience simultaneous axial accelerating and radial focusing forces.

### C. Nonlinear Regime

Wakefield generation in the nonlinear 1D regime can be examined by assuming that the drive beam is nonevolving, i.e., the drive beam is a function of only the coordinate  $\xi = z - v_p t$ , where  $v_p \leq c$  is the phase velocity of the plasma wave. For laser drivers,  $v_p \simeq v_g$ , where  $v_g$  is the laser pulse group velocity. The 1D limit applies to broad drivers,  $k_p r_\perp \gg 1$ , where  $r_\perp$  is the characteristic radial dimension of the drive beam. Using the fluid momentum and continuity equations, the Poisson equation

$\partial^2\phi/\partial\xi^2 = k_p^2(n/n_0 - 1)$  can be written as [46, 57, 58]

$$k_p^{-2} \frac{\partial^2\phi}{\partial\xi^2} = \gamma_p^2 \left\{ \beta_p \left[ 1 - \frac{(1+a^2)}{\gamma_p^2(1+\phi)^2} \right]^{-1/2} - 1 \right\}, \quad (12)$$

where  $\gamma_p = (1 - \beta_p^2)^{-1/2}$  and  $\beta_p = v_p/c$ . The axial electric field of the wake is given by  $E_z = -E_0\partial\phi/\partial\xi$ . In the limit  $\gamma_p^2 \gg 1$ , (12) simplifies to [59–62]

$$k_p^{-2} \frac{\partial^2\phi}{\partial\xi^2} = \frac{(1+a^2)}{2(1+\phi)^2} - \frac{1}{2}. \quad (13)$$

Analytical solutions can be found for square laser pulse profiles [59–62]. As the plasma wave amplitude becomes nonlinear, (12) and (13) indicate that the plasma wave steepens and its period lengthens, as is discussed in Sect. II E.

In the two-dimensional (2D) and 3D nonlinear regimes, simulations are usually required. One possible approach is to use a nonlinear quasi-static fluid model [36, 52], which is discussed in Sect. V. An alternative approach is to use 2D and 3D particle simulations [63–66].

## D. Wavebreaking

Plasmas are capable of supporting large amplitude, electrostatic waves with phase velocities near the speed of light. Such waves can be used to accelerate charged particles. In the linear regime, the electric field of a plasma wave in a plasma-based accelerator has the form  $E_z = E_{\max} \sin[\omega_p(z/v_p - t)]$ , where  $v_p \simeq c$  is the phase velocity. The peak field amplitude  $E_{\max}$  of the plasma wave can be very high and can be estimated from the Poisson equation  $\nabla \cdot \mathbf{E} = 4\pi e(n_0 - n_e)$ . A simple estimate for the maximum field amplitude is given by assuming all of the plasma electrons are oscillating with a wavenumber  $k_p = \omega_p/c$ . This gives  $(\omega_p/c)E_{\max} = 4\pi en_0$ , or  $E_{\max} = E_0$ , where  $E_0 = cm_e\omega_p/e$  is the nonrelativistic wavebreaking field [11].

It is possible for the maximum amplitude of a nonlinear plasma wave to exceed the value  $E_0$ . Using the nonlinear, relativistic, cold fluid equations in 1D, it is possible to show that the maximum amplitude of a plasma wave is given by [67, 68]

$$E_{\text{WB}} = \sqrt{2}(\gamma_p - 1)^{1/2} E_0, \quad (14)$$

which is referred to as the relativistic wavebreaking field, where  $\gamma_p = (1 - v_p^2/c^2)^{-1/2}$  is the relativistic Lorentz factor associated with the phase velocity of the plasma wave. As an example, consider a laser-driven accelerator with a plasma density of  $n_0 \simeq 10^{16} \text{ cm}^{-3}$ . The plasma wave phase velocity is approximately the group velocity of the laser,  $\gamma_p \simeq \omega/\omega_p$ , where  $\omega$  is the frequency of the laser. For a laser wavelength of  $1 \mu\text{m}$ ,  $\gamma_p \simeq 300$  and  $E_{\text{WB}} \simeq 25E_0$ .

Fluid equations can be used to describe a coherent plasma wave as long as the electron fluid velocity  $v_e$  is less

than the phase velocity of the wave,  $v_e < v_p$ . In the 1D cold fluid limit, the nonlinear plasma wave is described by (12). As the wave amplitude increases,  $v_e$  increases. The wave is said to “break” when  $v_e \rightarrow v_p$ , at which point the plasma density becomes singular,  $n \rightarrow \infty$ . Mathematically, wavebreaking occurs in a cold, 1D plasma when  $E_{\max} \rightarrow E_{\text{WB}}$ , where  $E_{\text{WB}}$  is given by (14).

The above value for the wavebreaking field was based on cold fluid theory. Thermal electron effects, however, can lead to a reduction in the wavebreaking field. In a warm plasma, the electron distribution has a thermal spread about its mean fluid velocity  $v_e$ . Roughly speaking, a large fraction of the electron distribution will become trapped in the plasma wave when  $|v_e + v_{\text{th,eff}}| \rightarrow v_p$ , where  $v_{\text{th,eff}}$  is an effective thermal velocity spread. This leads to wavebreaking. Using warm, relativistic fluid theories, expressions for the thermal wavebreaking field amplitude  $E_{\text{th}}$  have been derived [69, 70] of the form

$$E_{\text{th}} = (m_e c^2 / 3T)^{1/4} f_{\text{th}}(\gamma_p, T) E_0, \quad (15)$$

where  $f_{\text{th}}(\gamma_p, T)$  is a slowly varying function of  $\gamma_p$  and the electron temperature  $T$  with a typical magnitude on the order of unity  $f_{\text{th}}(\gamma_p, T) \sim 1$ . Katsouleas and Mori [69] give  $f_{\text{th}}^2 = \ln(2\gamma_p^{1/2}\beta_{\text{th}}^{1/4})$  for  $\gamma_p\beta_{\text{th}}^{1/2} \gg 1$ , where  $\beta_{\text{th}} = 3T/m_e c^2$ . Thermal effects will limit the wave amplitude if the warm wavebreaking field is less than the cold wavebreaking field,  $E_{\text{th}} < E_{\text{WB}}$ . As an example,  $\gamma_p \simeq 300$  and  $T = 10 \text{ eV}$  give a thermal wavebreaking limit of  $E_{\text{th}} \simeq 12E_0$ , which is approximately one-half that of the cold wavebreaking result  $E_{\text{WB}}$ .

The above expressions for the wavebreaking field were based on 1D theories. Wavebreaking in 3D has not been thoroughly investigated and general expressions for the maximum field amplitude are not known. Particle-in-cell simulations [71, 72] in 2D have demonstrated the generation of plasma waves with amplitudes on the order of  $E_0$ . Simulations [73] based on nonlinear, 2D axisymmetric fluid equations have shown wave amplitudes in excess of  $E_0$ . The transverse structure of the plasma wave and curvature of the wake phase fronts can lead to 2D wavebreaking [74], as discussed in Sect. II E.

## E. Nonlinear Plasma Waves

In the linear regime,  $E_{\max} \ll E_0$ , the plasma wave is a simple sinusoidal oscillation with frequency  $\omega_p$  and an arbitrary phase velocity  $v_p$  (the phase velocity is determined by the driver), e.g.,  $\phi = \phi_0 \cos[\omega_p(z/v_p - t)]$ . When  $E_{\max} \gtrsim E_0$ , the plasma wave becomes highly nonlinear. In the 1D cold fluid limit, the nonlinear plasma wave is described by (12). In the region behind the drive beam,  $a^2 = 0$ , an analysis of (12) indicates that the electrostatic potential oscillates between  $\phi_{\min} \leq \phi \leq \phi_{\max}$  and the axial electric field oscillates between  $-E_{\max} \leq E \leq E_{\max}$ . The values  $\phi_{\min}$  and  $\phi_{\max}$ , denoted by  $\phi_m$ , are given by

[68]

$$\phi_m = \hat{E}_{\max}^2/2 \pm \beta_p \left[ (1 + \hat{E}_{\max}^2/2)^2 - 1 \right]^{1/2}, \quad (16)$$

where  $\hat{E}_{\max} = E_{\max}/E_0$  and the  $\pm$  give  $\phi_{\max}$  and  $\phi_{\min}$ , respectively. Wavebreaking occurs when the density becomes singular. From (12), this occurs when  $(1 + \phi) \rightarrow 1/\gamma_p$ . At wavebreaking,  $\phi_{\min} = 1/\gamma_p - 1$ , and (16) implies  $E_{\max} = \sqrt{2}(\gamma_p - 1)^{1/2}E_0 \equiv E_{\text{WB}}$ .

For  $E_{\max}/E_0 \gtrsim 1$ , (12) indicates that the electric field departs from a simple sinusoidal form [59–62, 67]. In particular, the electric field exhibits the characteristic “sawtooth” profile associated with wave steepening and the density oscillations become highly peaked (as illustrated in Fig. 5 of Sect. III A). Furthermore, the period of the nonlinear plasma wave increases as the amplitude increases. The nonlinear plasma wavelength in the limit  $\gamma_p \gg 1$  is given by [59–62]

$$\lambda_{Np} = \lambda_p \begin{cases} 1, & E_{\max}/E_0 \ll 1, \\ (2/\pi)E_{\max}/E_0, & E_{\max}/E_0 \gg 1 \end{cases} \quad (17)$$

where  $E_{\max}$  is the peak electric field of the plasma wave and  $\lambda_p = 2\pi/k_p = 2\pi c/\omega_p$ .

The lengthening of the plasma wave period can be important in plasma-based accelerators. For example, in the PBWA, the plasma wave is driven at a constant beat frequency  $\Delta\omega = \omega_1 - \omega_2 \simeq \omega_p$ . As the wave grows, however, the effective plasma frequency decreases,  $\omega_{p,\text{eff}} = 2\pi c/\lambda_{Np}$ . Hence, the driver (i.e., the laser beat wave) becomes out of phase with the nonlinear plasma wave. This leads to saturation of the plasma wave amplitude in the PBWA [75, 76]. Alternatively, if the plasma wave is to be driven to large amplitudes by a series of individual laser pulses, the change in the nonlinear plasma period can affect the optimal spacing between pulses as well as the optimal duration of the pulses [48].

The increase in the plasma wavelength with increasing wave amplitude has an additional effect on nonlinear 2D plasma waves. Consider a plasma wave which is driven more strongly on-axis than it is off-axis. This would be the case in a laser driven accelerator, where the laser intensity peaks on-axis and typically has a Gaussian radial profile. On-axis, the plasma wave amplitude is maximum and, in the nonlinear regime, the plasma wavelength on-axis is larger than it is off-axis. Thus, the plasma wavelength varies as a function of radius  $\lambda_{Np}(r)$ . This causes the wavefronts of the plasma wave to become curved and take on a “horseshoe” shape. For a plasma wave of fixed amplitude, the farther back within the plasma wave train, the more curved the plasma wave front, i.e., after  $\ell$  periods, the phase front at large radii is located at  $\ell\lambda_p$ , whereas on-axis, the phase front is located at  $\ell\lambda_{Np}(r=0)$ . This effect has been observed in 2D nonlinear fluid simulations [36, 52, 73] and 2D particle simulations [71, 72, 74].

The curvature effects of the plasma wave phase fronts described above can lead to 2D wavebreaking. Specifically, when the curvature radius of the phase front is

on the order of the electron fluid displacement, trapping occurs and the regular structure of the plasma wave is destroyed (i.e., 2D wavebreaking) [74]. For a fixed amplitude nonlinear 2D wake (i.e., neglecting wake damping), 2D wavebreaking will always occur at a sufficiently long distance behind the driver. The larger the wake amplitude, the shorter the distance behind the driver is the onset point of 2D wavebreaking. A similar effect can occur for linear (or nonlinear) plasma waves in a plasma channel. In a plasma channel, the plasma density is minimum on axis, hence the plasma wavelength is longer on-axis than off-axis. This leads to wake wavefront curvature, and the curvature increases with distance behind the driver until the point of 2D wavebreaking is reached, as described above.

## F. Electron Acceleration and Dephasing

An electron can be accelerated along the  $z$ -axis by an electrostatic plasma wave of the form  $E_z = E_{\max} \sin \omega_p(z/v_p - t)$ . As the electron is accelerated, its velocity will increase and approach the speed of light,  $v_z \rightarrow c$ . If the phase velocity of the plasma wave is constant with  $v_p < c$ , the electrons will eventually outrun the plasma wave and move into a phase region of the plasma wave which is decelerating. This limits the energy gain of the electron in the plasma wave and is commonly referred to as electron dephasing. The dephasing length  $L_d$  is defined as the length the electron must travel before it phase slips by one-half of a period with respect to the plasma wave. For a highly relativistic electron,  $v_z \simeq c$ , the dephasing time  $t_d$  is given by  $\omega_p(c/v_p - 1)t_d = \pi$ , i.e.,  $L_d = ct_d \simeq \gamma_p^2 \lambda_p$ , assuming  $\gamma_p \gg 1$ . The maximum energy gain after a dephasing length [1, 2] is given approximately by  $W_{\max} \simeq eE_{\max}L_d \simeq 2\pi\gamma_p^2(E_{\max}/E_0)m_e c^2$ , assuming  $E < E_0$ .

In a 1D plasma wave, electron trapping, acceleration, and dephasing can be studied by examining the electron orbits in phase space  $(u, \psi)$ , where  $u = p/m_e c$  is the normalized momentum and  $\psi = k_p \xi = k_p(z - v_p t)$  is the phase. In the linear regime, the plasma wave is described by a sinusoidal electrostatic potential  $\phi = \phi_0 \cos \psi$ , where  $\phi_0 = E_{\max}/E_0$  is the amplitude. The phase region  $-\pi < \psi < 0$  is accelerating. Consider an electron injected into the plasma wave with  $v_z < v_p$  at  $\psi = 0$ . Initially, the electron is slipping backward with respect to the plasma wave. If the initial electron velocity is too low, the electron does not gain sufficient energy and  $v_z < v_p$  at  $\psi = -\pi$ . Hence, the electron would be untrapped and would continue to slip backward through the plasma wave. If, however, the electron has a sufficiently high initial velocity such that  $v_z > v_p$  as the electron approaches  $\psi \rightarrow -\pi$ , the electron will be trapped and execute closed orbits in the  $-\pi < \psi < \pi$  phase region. The separatrix, which separates the region of trapped and untrapped orbits in phase space, is shown schematically in Fig. 2 for a small amplitude plasma wave.

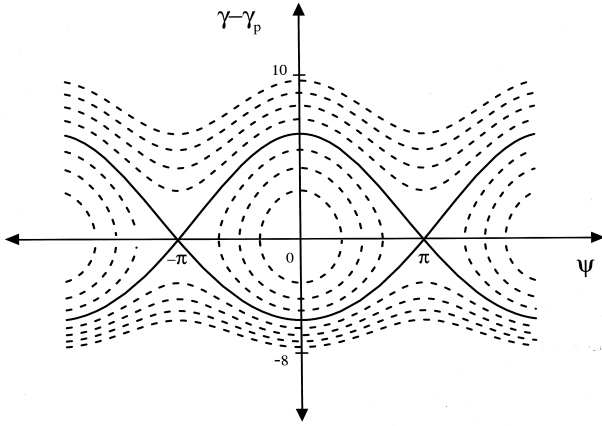


FIG. 2: Single particle orbits in phase space  $(\gamma, \psi)$  for an electron in a small amplitude, sinusoidal plasma wave with a normalized potential given by  $\phi = \phi_0 \cos \psi$ , with  $\gamma_p = 20$  and  $\phi_0 = 10^{-3}$ . Solid curve is separatrix

The motion of a test electron in a 1D nonlinear plasma wave is described by the Hamiltonian [68]

$$H(u, \psi) = \gamma - \beta_p u - \phi(\psi), \quad (18)$$

where  $H(u, \psi) = \text{constant}$  along a given electron orbit and  $\phi = \phi(\psi)$  is the solution to (12), which oscillates between  $\phi_{\min} \leq \phi \leq \phi_{\max}$  and is related to  $E_{\max}$  by (16). In particular, the separatrix  $\gamma_s(\psi)$  characterizing the test electron orbits in  $(\gamma, \psi)$  phase space is given by  $H(\gamma_s, \psi) = H(\gamma_p, \psi_{\min})$ , where  $\phi(\psi_{\min}) = \phi_{\min}$ .

Figure 3 shows several separatrices for  $\gamma_p = 20$  and for different values of the plasma wave amplitude, characterized by the parameter  $\epsilon$ , where  $\phi_{\max} = (2\gamma_p^2 - 1)\epsilon/\gamma_p - 1$ , for  $\epsilon = 0.03, 0.04, 0.1, 0.3$  and  $0.9$  ( $\epsilon = 1$  corresponds to wavebreaking). This corresponds to values of the peak electric field  $E_{\max}$  given by  $E_{\max}/E_0 = 0.18, 0.47, 1.5, 3.2$ , and  $5.8$ , respectively (at wavebreaking,  $E_{\text{WB}}/E_0 = 6.2$ ). The value  $\epsilon = 0.03$  corresponds to the innermost curve and  $\epsilon = 0.9$  corresponds to the outermost curve. These curves were obtained [68] by plotting  $H(\gamma_s, \psi) = H(\gamma_p, \psi_{\min})$  after numerically solving (12) for  $\phi = \phi(\psi)$  with the initial conditions  $\partial\phi/\partial\xi = 0$  and  $\phi = \phi_{\max}$  at  $\psi = 0$ . The width of the separatrix  $\Delta\psi_s$  corresponds to the nonlinear plasma wavelength,  $\lambda_{Np} = \Delta\psi_s/k_p$ , given by (17). As the plasma wave amplitude increases, the nonlinear wavelength increases.

For small wave values, e.g.,  $\epsilon = 0.03$ , the separatrix is nearly symmetric (as would be the case for a linear, sinusoidal plasma wave). Notice that for  $\epsilon = 0.03$ ,  $\gamma_{\min} > 1$ , indicating that an electron injected with  $v = v_{\min} > 0$  at  $\psi = 0$  would be trapped, where  $v_{\min} = (1 - \gamma_{\min}^{-2})^{1/2}$ . As the wave amplitude increases,  $\gamma_{\min}$  decreases to the point  $\gamma_{\min} = 1$ , corresponding approximately to the curve  $\epsilon = 0.04$  in Fig. 3. Hence, a test electron which is at rest at  $\psi = 0$  would be trapped. This does not mean that the background plasma electrons will be trapped. The background electrons are undergoing the plasma wave fluid

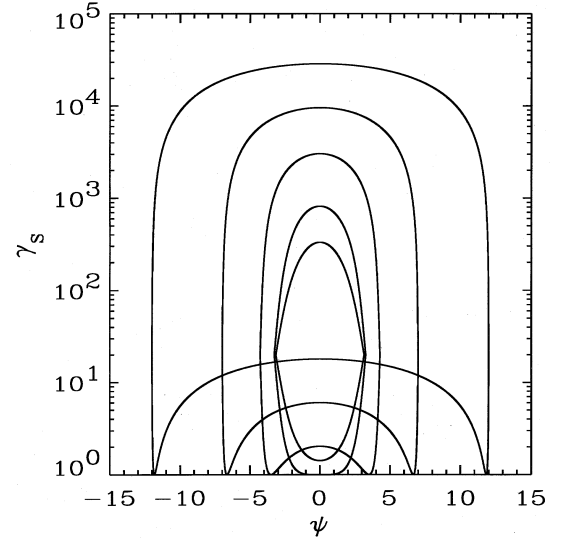


FIG. 3: The separatrix  $\gamma_s(\psi)$  plotted for several values of the plasma wave amplitude  $\epsilon = 0.03, 0.04, 0.1, 0.3$ , and  $0.9$  ( $\epsilon = 1$  corresponds to wavebreaking), with  $\gamma_p = 20$ . The value  $\epsilon = 0.03$  corresponds to the innermost curve and  $\epsilon = 0.9$  corresponds to the outermost curve

oscillation and are flowing backward (opposite to  $v_p$ ) at the phase  $\psi = 0$  with the maximum fluid velocity. Increasing  $\epsilon$  further causes  $\gamma_{\min}$  (at  $\psi = 0$ ) to increase. This implies that a test electron at  $\psi = 0$  with  $v = -|v_{\min}|$  would be trapped. Further increasing  $\epsilon$  causes  $v_{\min}$  to become more negative. Wavebreaking occurs when  $\epsilon = 1$ , at which point  $\gamma_{\min} = \gamma_p$ ,  $v_{\min} = -v_p$ , and, hence, all of the plasma electrons become trapped in the wave.

The maximum energy  $\gamma_{\max}$  and minimum energy  $\gamma_{\min}$ , denoted by  $\gamma_m$ , for an electron on the separatrix are given by [68]

$$\gamma_m = \gamma_p(1 + \gamma_p\Delta\phi) \pm \gamma_p\beta_p [(1 + \gamma_p\Delta\phi)^2 - 1]^{1/2}, \quad (19)$$

where  $\Delta\phi = \phi_{\max} - \phi_{\min}$ , i.e.,  $\Delta\phi = 2\beta_p[(1 + \hat{E}_{\max}^2/2)^2 - 1]^{1/2}$ , as indicated by (16). In the limits  $\gamma_p\Delta\phi \gg 1$  and  $\gamma_p^2 \gg 1$ ,  $\gamma_{\max} \simeq 2\gamma_p^2\Delta\phi$  and  $\gamma_{\min} \simeq \Delta\phi/2 + 1/(2\Delta\phi)$ . In particular, the maximum energy of a trapped electron is given by [68]

$$\gamma_{\max} \simeq 2\gamma_p^2 \begin{cases} \hat{E}_{\max}^2, & \text{for } \hat{E}_{\max}^2 \gg 2, \\ 2\hat{E}_{\max}, & \text{for } 2 \gg \hat{E}_{\max}^2 \gg 1/4\gamma_p^2, \end{cases} \quad (20)$$

where  $\hat{E}_{\max} = E_{\max}/E_0$ . The limit  $\hat{E}_{\max}^2 \ll 2$  corresponds to the well-known limit for linear, sinusoidal plasma waves [1, 2, 77]. When  $\hat{E}_{\max}^2 \gg 2$ , however,  $\gamma_{\max} \simeq 2\gamma_p^2\hat{E}_{\max}^2$ , which implies that higher electron energies can be obtained for electrons trapped in nonlinear plasma waves. The nonlinear regime where  $\hat{E}_{\max} > 1$  has been observed in simulations of the self-modulated LWFA [71–73] and laser wakefields driven by multiple pulses [47, 48, 50]. At wavebreaking ( $\epsilon = 1$ ,  $E_{\max} = E_{\text{WB}}$ ), (19) indicates that [68]  $\gamma_{\max} = 4\gamma_p^3 - 3\gamma_p$ .

A rough estimate for the dephasing length is given by  $W_{\max} = m_e c^2 \gamma_{\max} = e E_{\max} L_d$ . This yields

$$L_d = \gamma_p^2 \lambda_{Np} \begin{cases} 2/\pi, & \hat{E}_{\max} \ll 1, \\ 1/2, & \hat{E}_{\max} \gg 1, \end{cases} \quad (21)$$

where  $\lambda_{Np}$  is given by (17). The actual dephasing length [78] requires the simultaneous solution of the equation of motion and (12).

As an example, consider a LWFA with  $n_0 = 2.8 \times 10^{18} \text{ cm}^{-3}$  and  $\lambda = 1 \mu\text{m}$ , i.e.,  $\gamma_g \simeq \gamma_p \simeq 20$  and  $E_0 \simeq 160 \text{ GV/m}$ . In the limit  $\hat{E}_{\max}^2 \gg 2$ , (20) yields  $W_{\max} \simeq 400 \hat{E}_{\max}^2$ , where  $W_{\max} \simeq m_e c^2 \gamma_{\max}$ . At wave-breaking,  $E_{\text{WB}} \simeq 6.2 E_0$  and  $W_{\max} \simeq 16 \text{ GeV}$ . Notice that  $\gamma_{\max} \simeq 4 \gamma_p^3 E_{\max} / E_{\text{WB}}$ , assuming  $\gamma_p^2 \gg 1$  and  $\gamma_p (E_{\max} / E_{\text{WB}})^2 \gg 1$ . Hence, for a fixed value of  $E_{\max} / E_{\text{WB}}$ ,  $\gamma_{\max} \propto n_0^{-3/2}$  and substantially higher single-stage energy gains can be achieved by operating at lower densities.

It should be noted that the above results are obtained from 1D theory and assume a constant amplitude plasma wave. An evolving plasma wave amplitude and 2D effects could alter these results. For example, Mora [77] has shown that the effects of laser diffraction can lead to a more restrictive trapping condition for linear plasma waves.

### G. Plasma Wave Phase Velocity

The phase velocity of the plasma wave is important for determining the minimum injection energy, the maximum energy gain, and the dephasing length. Neglecting the evolution of the drive beam as it propagates, the phase velocity of the plasma wave is equal to the group velocity of the drive laser.

In the linear regime, the group velocity of a laser pulse in a plasma can be determined from the 1D dispersion relation,  $\omega^2 = c^2 k^2 + \omega_p^2$ . This yields  $v_g = c(1 - \omega_p^2 / \omega^2)^{1/2}$  and  $\gamma_g = (1 - v_g^2 / c^2)^{-1/2} = \omega / \omega_p$ . Nonlinear corrections to the group velocity in 1D have been analyzed by Decker and Mori [79]. In the long pulse, underdense  $\omega_p / \omega \ll 1$  limit, the nonlinear group velocity is  $(\omega / \omega_p)[(\gamma_{\perp} + 1)/2]^{1/2}$ , where  $\gamma_{\perp} = (1 + a_0^2/2)^{1/2}$  is the relativistic Lorentz factor associated with the quiver motion of the electrons in the laser field.

The group velocity of a laser pulse is also reduced by 3D effects. For example, consider a laser pulse in vacuum undergoing Rayleigh diffraction. The evolution of the spot size (or radius) of a Gaussian laser beam evolves according to  $r_s = r_0(1 + z^2/Z_R^2)^{1/2}$ , where  $r_0$  is the minimum spot size at the focal point  $z = 0$ , and  $Z_R = kr_0^2/2$  is the Rayleigh length. In effect, the photons are traveling at approximately a diffraction angle  $\theta_d = r_0/Z_R$  with respect to the  $z$ -axis. Hence, the axial group velocity is reduced by  $v_g \simeq c \cos \theta_d \simeq c(1 - \theta_d^2/2)$ . A more detailed

calculation indicates that, in the linear regime, the 3D group velocity is given by [80]

$$\gamma_g \simeq (\omega_p^2 / \omega^2 + 2c^2 / \omega^2 r_0^2)^{-1/2}. \quad (22)$$

In effect, the linear 3D dispersion relation is given by  $\omega^2 - c^2 k^2 = \omega_p^2 + 2c^2 / r_0^2$  (for a matched laser pulse in a plasma channel,  $\omega^2 - c^2 k^2 = \omega_p^2 + 4c^2 / r_0^2$ ). For tightly focused laser pulses, this 3D correction can significantly limit the group velocity. As an example, consider a laser pulse, with a  $\lambda = 1 \mu\text{m}$  wavelength and  $r_0 = 10 \mu\text{m}$  spot size, propagating in a plasma of density  $n_0 = 10^{16} \text{ cm}^{-3}$ . In 1D,  $\gamma_g \simeq 330$ , however, the finite spot size reduces the group velocity such that  $\gamma_g \simeq 44$ .

Distortions of the pulse driving the plasma wave can also affect the plasma wave phase velocity. In the LWFA in the 1D limit, it has been shown that the wake phase velocity is approximately equal to the group velocity associated with the position of the peak of intensity profile [79]. Furthermore, the plasma wave can lead to locally enhanced diffraction and focusing, which distorts the pulse profile and reduces the plasma wave phase velocity [81].

### H. Photon Acceleration

In addition to accelerating electrons, a plasma wave can be used to upshift the frequency of a properly phased, low intensity, short laser pulse, as shown schematically in Fig. 4 (often referred to as photon acceleration) [3, 82]. Consider a plasma wave with an electron density perturbation of the form  $\delta n = -\delta n_0 \sin k_p \zeta$ , where  $\zeta = z - ct$ , and a low intensity, “witness” laser pulse centered about  $\zeta = 0$  with a pulse length  $L \ll \lambda_p$ . The local density at the front of the pulse,  $n(\zeta = L/2)$ , will be less than that at the back of the pulse,  $n(\zeta = -L/2)$ . Since the local phase velocity of the laser pulse is given by  $\beta_p = v_p/c \simeq 1 + \omega_p^2(\zeta)/2\omega^2$ , where  $\omega_p^2(\zeta) \propto n(\zeta)$ , the phase velocity at the pulse front is less than that at the back of the pulse, i.e.,  $v_p(L/2) < v_p(-L/2)$ . Hence, the phase peaks at the back move faster than those at the front and the pulse wavelength decreases (the pulse frequency increases). For small shifts, the laser wavelength will evolve according to  $\lambda \simeq \lambda_0 + z \Delta \beta_p$ , where  $\Delta \beta_p = \lambda_0 d\beta_p/d\zeta < 0$  is the difference in phase velocity between adjacent phase peaks,  $z$  is the propagation distance, and  $\lambda_0 = 2\pi c/\omega_0$  is the initial laser wavelength. Hence, the frequency shift is given by  $\omega/\omega_0 \simeq 1 - z d\beta_p/d\zeta$ , where  $d\beta_p/d\zeta \simeq (\omega_p^2/2\omega_0^2)d(\delta n/n_0)/d\zeta$ . A more detailed calculation indicates that the frequency will be upshifted according to [82]

$$\frac{\omega}{\omega_0} \simeq \left( 1 + \frac{\omega_p^2}{\omega_0^2} \frac{\delta n_0}{n_0} k_p z \cos k_p \zeta \right)^{1/2}, \quad (23)$$

where nonlinear effects and phase slippage between the laser pulse and plasma wave (i.e., dephasing) have been neglected.

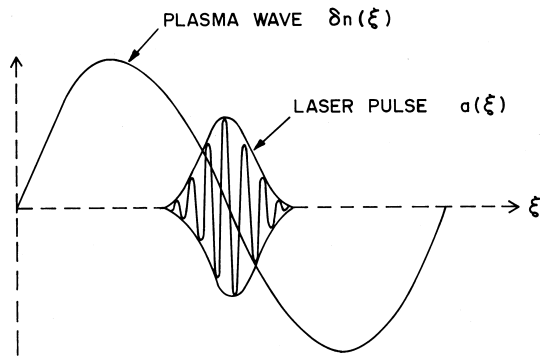


FIG. 4: Schematic of laser pulse frequency upshifting by a plasma wave with  $v_p \simeq v_g \simeq c$  (pulse moving to the right). Positive frequency shifts require the laser pulse to be centered about regions of the wave with a decreasing density

Typically, the plasma wave induced frequency shifts are small. For example, consider a laser with  $\lambda = 1 \mu\text{m}$  and  $r_0 = 30 \mu\text{m}$ , propagating in a plasma of density  $n_0 = 10^{18} \text{cm}^{-3}$  ( $\lambda_p = 30 \mu\text{m}$ ). After propagating one Rayleigh length  $z = Z_R$ ,  $\omega/\omega_0 \simeq 1 + \delta n_0/3n_0$ . Small frequency shifts, however, can be detected and this process can be useful for diagnosing the wakefield [83, 84]. Large frequency shifts require long propagation distances and large plasma wave amplitudes. For example, after one electron dephasing length  $L_d = \lambda_p \omega^2/\omega_p^2$ ,  $\omega/\omega_0 = (1 + 2\pi\delta n_0/n_0)^{1/2}$ .

### III. LASER-PLASMA ACCELERATORS

#### A. Laser Wakefield Accelerator

In the laser wakefield accelerator (LWFA) [1, 32, 33], a single, short ( $\lesssim 1$  ps), ultrahigh intensity ( $\gtrsim 10^{18} \text{W/cm}^2$ ) laser pulse drives a plasma wave. The wakefield is driven most efficiently when the laser pulse length is approximately the plasma period  $L \sim \lambda_p$ . The LWFA was first proposed by Tajima and Dawson [1]. Prior to 1988, the technology for generating ultra-intense, picosecond laser pulses did not exist and only the PBWA concept appeared feasible (which relied on long pulses of modest intensity). The LWFA was later re-invented independently by Gorbunov and Kirsanov [32] and by Sprangle et al. [33]. This roughly coincides to the time when CPA was applied to compact solid-state lasers and a table-top, terawatt laser system was first demonstrated by Mourou and co-workers [8]. The nonlinear theory of the LWFA in 1D was developed by Bulanov et al. [59], Sprangle et al. [60, 61], and Berezhiani and Murusidze [62]. The nonlinear theory of the LWFA in 2D, including the self-consistent evolution of the laser pulse, was analyzed by Sprangle et al. [36, 52].

As an intense laser pulse propagates through an underdense plasma,  $\lambda^2/\lambda_p^2 \ll 1$ , the ponderomotive force

associated with the laser pulse envelope,  $F_p \sim \nabla a^2$ , expels electrons from the region of the laser pulse. If the length scale  $L_z$  of the axial gradient in the pulse profile is approximately equal to the plasma wavelength,  $L_z \sim \lambda_p$ , the ponderomotive force excites large amplitude plasma waves (wakefields) with phase velocities approximately equal to the laser pulse group velocity [see Fig. 1(a)]. For a typical axially symmetric laser pulse (e.g., a Gaussian profile), the wakefield amplitude will be maximum when  $L \simeq \lambda_p/2$ , where  $L = c\tau_L$  is laser pulse length. The precise value of  $L$  which maximizes the wake amplitude will depend on the shape of the axial pulse profile. Following are some examples.

#### 1. Linear regime, sine pulse.

Consider a LWFA driven by a circularly polarized laser pulse with a normalized intensity  $a^2 = a_0^2 \exp(-2r^2/r_s^2) \sin^2(\pi\zeta/L)$  for  $0 < \zeta < L$ , where  $\zeta = z - ct$  and  $a_0^2 \ll 1$ . Solutions to (11) indicate that the wakefield amplitude is maximum for pulse lengths  $L \simeq \lambda_p$ . Behind the pulse,  $\zeta < 0$ , the axial electric field and density perturbation of the wake are given by [54]

$$\frac{E_z}{E_0} = \frac{\pi}{4} a_0^2 \exp\left(-\frac{2r^2}{r_s^2}\right) \cos k_p \zeta, \quad (24)$$

$$\frac{\delta n}{n_0} = \frac{\pi}{4} a_0^2 \left[ 1 + \frac{8}{k_p^2 r_s^2} \left( 1 - \frac{2r^2}{r_s^2} \right) \right] \exp\left(-\frac{2r^2}{r_s^2}\right) \sin k_p \zeta, \quad (25)$$

for the case  $L = \lambda_p$ . For linear polarization, averaging over the fast oscillation yields (24) and (25) with  $a_0^2$  replaced with  $a_0^2/2$ . Notice that a tightly focused laser pulse with  $k_p^2 r_s^2/8 < 1$  will result in a larger density perturbation  $\delta n/n_0$  on-axis, whereas the axial electric field  $E_z$  on-axis is unchanged in comparison to the 1D values.

#### 2. Linear regime, Gaussian pulse.

For the case of a circularly polarized, Gaussian pulse profile,  $a^2 = a_0^2 \exp(-\zeta^2/L^2)$ , the wakefield amplitude behind the pulse ( $\zeta^2 \gg L^2$ ) is given by [32]

$$E_{\text{max}}/E_0 = (\sqrt{\pi} a_0^2/2) k_p L \exp(-k_p^2 L^2/4), \quad (26)$$

assuming  $a_0^2 \ll 1$ . Equation (26) explicitly shows the dependence of the wake amplitude on the pulse length  $L$ . In particular, the wake amplitude achieves a maximum value of  $E_{\text{max}}/E_0 = a_0^2(\pi/2e)^{1/2} \simeq 0.76a_0^2$  when  $L = \lambda_p/\pi\sqrt{2}$ .

#### 3. Nonlinear regime, square pulse.

Consider a circularly polarized laser pulse with a square axial profile in the 1D limit  $r_0^2 \gg \lambda_p^2$ . The wakefield amplitude is maximum when  $L \simeq \lambda_{Np}/2$ , where  $\lambda_{Np}$

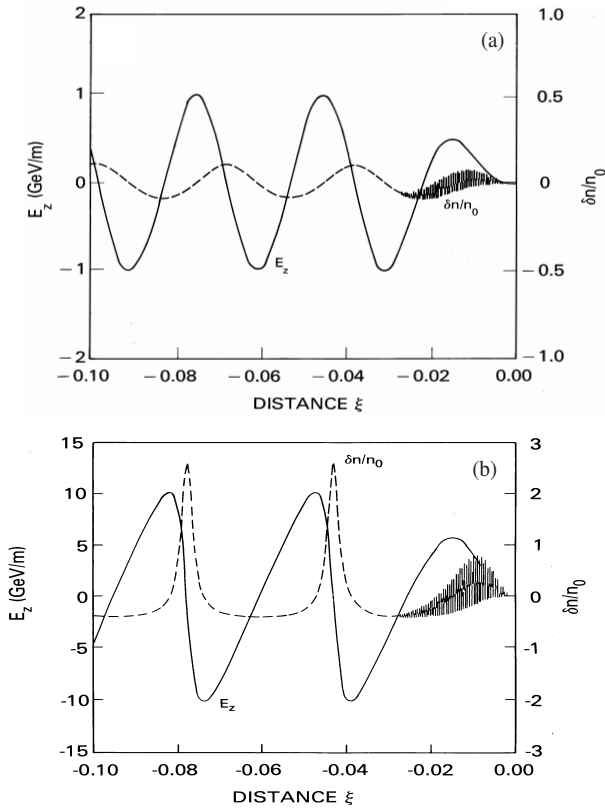


FIG. 5: Density variation  $\delta n/n_0$  (dashed curve) and the axial electric field  $E_z$  (solid curve) in an LWFA driven by a laser pulse located in the region  $-L \leq \zeta \leq 0$  (the pulse is moving to the right), where  $L = \lambda_p = 0.03$  cm, for (a)  $a_0 = 0.5$  and (b)  $a_0 = 2.0$

is the nonlinear plasma wavelength (17), and is given by [59–62]

$$E_{\max}/E_0 = a_0^2(1 + a_0^2)^{-1/2}, \quad (27)$$

where  $a_0^2 = 3.6 \times 10^{-19} \lambda^2 (\mu\text{m}) I_0 (\text{W}/\text{cm}^2)$  (for linear polarization, replace  $a_0^2$  with  $a_0^2/2$ ). Notice that  $E_{\max} \propto \lambda_p^{-1} \sim L^{-1}$ . Hence, the wakefield amplitude can be increased by operating at high densities and shorter pulse lengths. At high densities, however, the laser pulse group velocity is reduced and electron dephasing can limit the energy gain, as discussed in Sect. II F.

#### 4. Nonlinear regime, sine pulse.

As an example of nonlinear plasma wave behaviour, (12) has been solved numerically [60, 61] for a linearly polarized laser of the form  $a^2 = a_0^2 \sin^2(\pi\zeta/L) \cos^2(k\zeta)$  for  $-L < \zeta < 0$  (and zero otherwise), with  $L = \lambda_p$  and  $\lambda = 1 \mu\text{m}$ . The ambient plasma density is  $n_0 = 1.2 \times 10^{16} \text{ cm}^{-3}$ , which yields  $L = \lambda_p = 300 \mu\text{m}$  ( $\tau_L = L/c = 1$  ps). A mildly relativistic case  $a_0 = 0.5$  ( $I_0 = 3.5 \times 10^{17} \text{ W}/\text{cm}^2$ ) is shown in Fig. 5(a), and a

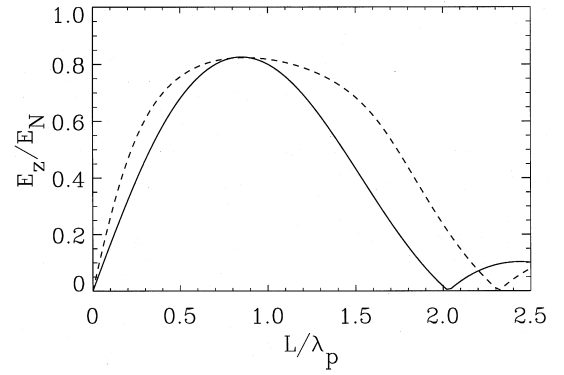


FIG. 6: Amplitude of axial electric field  $E_z$  plotted as a function of laser pulse length  $L$  for the LWFA examples shown in Fig. 5. The laser pulse envelope is given by  $a = a_0 \sin(\pi|\zeta|/L)$  for  $-L \leq \zeta \leq 0$  with  $a_0 = 0.5$  (solid curve) and  $a_0 = 2.0$  (dashed curve). The plasma density is held constant at  $n_0 = 1.2 \times 10^{16} \text{ cm}^{-3}$  ( $\lambda_p = 0.03$  cm)

highly relativistic case  $a_0 = 2$  ( $I_0 = 5.6 \times 10^{18} \text{ W}/\text{cm}^2$ ) is shown in Fig. 5(b). Figure 5 shows the density variation  $\delta n/n_0 = n/n_0 - 1$  and the axial electric field  $E_z$ , with  $E_{\max} \simeq 1$  GV/m in Fig. 5(a) and  $E_{\max} \simeq 10$  GV/m in Fig. 5(b). Note that the rapid oscillations in the plasma density at one-half the laser wavelength are due to a fast component of the ponderomotive force at twice the laser frequency, i.e.,  $a^2 \sim 1 + \cos(2k\zeta)$ . The nonlinear effects of wave steepening and period lengthening are clearly evident in Fig. 5(b).

Because the plasma wave is driven by a single laser pulse with  $L \simeq \lambda_p$ , the wakefield amplitude is relatively insensitive to uncertainties in the pulse duration and the plasma uniformity. This is shown in Fig. 6, where the peak wakefield amplitude  $E_{\max}$  is shown as a function of the pulse length  $L$ , at a fixed density and intensity. The parameters are identical to the sine profile laser pulse examples shown in Figs. 5(a) and 5(b) (i.e., for  $a_0 = 0.5$  and  $a_0 = 2$ ), only now the pulse length  $L$  is varied. Plotted in Fig. 6 is the wakefield amplitude normalized to  $E_N = E_0(a_0^2/2)(1 + a_0^2/2)^{-1/2}$ , which is the maximum wakefield amplitude for a square pulse profile. Notice that the electric field amplitude is maximum for  $L \simeq 0.75 \lambda_p$  and is fairly insensitive to changes in the pulse length. Also, the curve for the  $a_0 = 2$  case is broader because of an increase in the nonlinear plasma wavelength.

To summarize the optimal pulse length conditions for the square, sine, and Gaussian pulse profiles discussed above, it is convenient to express the pulse length in terms of the full-width-half-maximum (FWHM) length  $L_{\text{FWHM}}$  and the root-mean-square (RMS) length  $L_{\text{RMS}}$  of the pulse intensity profile. For the square pulse, the wakefield is maximum  $E_{\max} = a_0^2 E_0$  when  $L_{\text{FWHM}} = 0.5 \lambda_p$  ( $k_p L_{\text{RMS}} = 0.91$ ). For the sine pulse, the wakefield is maximum  $E_{\max} = 0.82 a_0^2 E_0$  when  $L_{\text{FWHM}} = 0.5 \lambda_p$

( $k_p L_{\text{RMS}} = 1.1$ ). For the Gaussian pulse, the wakefield is maximum  $E_{\text{max}} = 0.76 a_0^2 E_0$  when  $L_{\text{FWHM}} = 0.37 \lambda_p$  ( $k_p L_{\text{RMS}} = 1$ ). These results assume  $a_0^2 \ll 1$  and circular polarization.

Furthermore, since the laser pulse in the LWFA is of short duration,  $L \simeq \lambda_p$ , various instabilities which can be detrimental to the propagation of long pulses can be reduced. Schemes that use long laser pulses,  $L \gg \lambda_p$ , such as the PBWA and the self-modulated LWFA, are subject to various instabilities, some of which are discussed in Sect. VI.

Perhaps the first experimental evidence for plasma wave generation by the LWFA mechanism was obtained by Hamster et al. [85]. In these experiments, the emission of terahertz radiation at the plasma frequency was observed when the plasma was driven by a laser pulse of length  $L \simeq \lambda_p$ . Specifically,  $\omega_p/2\pi = 4.6$  THz radiation was observed for a 0.1 ps laser pulse propagating in a plasma of density  $2 \times 10^{17} \text{ cm}^{-3}$ . This radiation is emitted presumably by the 2D electron plasma currents of the laser-induced wakefield. Direct measurement of plasma wave generated in the LWFA has been reported by researchers at Ecole Polytechnique [83] and at the University of Texas at Austin [84] by using probe pulses and optical interferometry techniques. In the Ecole Polytechnique experiments [83], a 120 fs duration, 800 nm wavelength laser pulse with a maximum energy of 40 mJ was focused to a maximum intensity of  $3 \times 10^{17} \text{ W/cm}^2$  in a plasma of density  $10^{17} \text{ cm}^{-3}$ . A pair of probe pulses, separated from each other by  $1.5 \lambda_p$ , were used to map out the wakefield by adjusting the delay between the pump and probe pulses. A plasma wave with a perturbed density of 30% to 100% was measured over several plasma periods behind the probe pulse. At the University of Texas [84], three probe pulses were used to measure the density perturbation at a fixed delay behind the pump pulse. By varying the ambient plasma density, the plasma wave amplitude was observed to vary in good agreement with theory.

Dewa et al. [34] have reported on the observation of electron acceleration in LFWA experiments, although with some controversy [86], with energies of 100 MeV (17 MeV injected from a linac) with a 2 TW laser system. Amiranoff et al. [35] have observed LWFA accelerated electrons with an energy gain of 1.6 MeV (3 MeV injected) using a 3.5 TW laser system. The peak longitudinal electric field was estimated to be 1.5 GV/m.

## B. Plasma Beat Wave Accelerator

In the plasma beat wave accelerator (PBWA) [1, 2, 28, 75, 87, 88], two long pulse laser beams of frequencies  $\omega_1$  and  $\omega_2$  are used to resonantly excite a plasma wave. This is done by appropriately adjusting the laser frequencies and plasma density to satisfy the resonance condition  $\Delta\omega \equiv \omega_1 - \omega_2 \simeq \omega_p$ . When this is satisfied, large amplitude plasma waves can be generated. The PBWA

was first proposed by Tajima and Dawson [1] as an alternative to the laser wakefield accelerator, since compact, ultrashort pulse, ultrahigh power laser technology [9, 10] was not available in 1979. The PBWA was subsequently analyzed by the various researchers [2, 5, 76, 89–92]. (Resonant excitation of a plasma wave using two laser beams had been previously analyzed by Rosenbluth and Liu [75] for plasma heating applications.) To overcome the problem of dephasing between the accelerated electrons and the plasma wave, Katsouleas and Dawson [93] proposed the use of a transverse magnetic field. Tang et al. [76] described how the plasma wave amplitude could be increased by operating at an optimal frequency mismatch  $\Delta\omega_{\text{opt}}$ , such that  $\omega_1 - \omega_2 = \omega_p + \Delta\omega_{\text{opt}}$ . Since this early work, various aspects of the PBWA have been analyzed and simulated, such as the self-focusing of the laser beams by relativistic, plasma wave, and cascading effects [5, 91, 92, 94].

Consider two lasers beams with combined normalized vector potentials given by  $a = a_1 \cos(k_1 z - \omega_1 t) + a_2 \cos(k_2 z - \omega_2 t)$ , where  $k_{1,2}$  are the laser wavenumbers. The ponderomotive force  $\nabla a^2/2$  will have a resonant beat term  $(a^2)_{\text{res}} = a_1 a_2 \cos(\Delta k z - \Delta\omega t)$ , where  $\Delta k \equiv k_1 - k_2$ . In the linear regime, plasma wave generation is described by  $(\partial^2/\partial t^2 + \omega_p^2)\phi = \omega_p^2 (a^2)_{\text{res}}$ , and the ponderomotive beat term can resonantly drive a plasma wave when  $\Delta\omega \simeq \omega_p$ . When the resonance condition is exactly satisfied,  $\Delta\omega = \omega_p$ , secular growth of the plasma wave results,  $\phi = -\phi_s \sin(\Delta k z - \Delta\omega t)$ , where  $\phi_s = a_1 a_2 k_p |\zeta|/4$  and  $|\zeta| = |z - ct|$  is the distance behind the front of the laser beams. Hence, the amplitude of the plasma wave within the laser pulse is [75]

$$E_{\text{max}}/E_0 = a_1 a_2 k_p |\zeta|/4. \quad (28)$$

Furthermore, notice that the phase velocity of the plasma,  $v_p = \Delta\omega/\Delta k$ , is given by  $v_p/c \simeq 1 - \omega_p^2/(2\omega_1\omega_2)$  in the limit  $\omega_p^2/\omega_1^2 \sim \omega_p^2/\omega_2^2 \ll 1$ , i.e., the phase velocity of the plasma wave is approximately equal to the group velocity of the driving lasers.

In effect, the laser beat wave acts as a series of laser pulses, each of amplitude  $a_1 a_2$  and of duration  $\Delta\tau = 2\pi/\Delta\omega$ . Each of these pulses generates a wake of amplitude  $E_{\text{max}}/E_0 = \pi a_1 a_2/2$ . The total plasma wave amplitude generated by a laser beat wave of length  $L = N\lambda_p$  is  $E_{\text{max}}/E_0 = N\pi a_1 a_2/2$ , where  $N$  is the number of laser beat periods within the pulse.

The result given by (28) was based on linear plasma theory,  $|\phi| \ll 1$ . Various nonlinear effects were neglected. In particular, as discussed in Sect. II E, as the plasma wave amplitude increases the plasma wave period increases. Since the period of the beat wave is fixed, whereas the period of the plasma wave is increasing, the plasma wave will eventually become out of phase with the laser beat wave. This resonant detuning of the plasma wave from the beat wave will limit the amplitude of the plasma wave [75].

The nonlinear dynamics of the beat wave generation in 1D with  $\omega_p^2/\omega^2 \ll 1$  can be examined using the

nonlinear Poisson equation (13). Analysis of (13) indicates that the nonlinear plasma wavelength is given by  $\lambda_{Np} = (4/k_p)(1 + \phi_s)^{1/2} E_2(\varrho)$ , where  $\phi_s$  is the maximum amplitude of the plasma wave,  $\varrho = 1 - (1 + \phi_s)^{-2}$ , and  $E_2$  is the complete elliptic integral of the second kind. In the limit  $\phi_s^2 \ll 1$ ,  $\lambda_{Np} \simeq \lambda_p(1 + 3\phi_s^2/16)$ , which indicates that the nonlinear plasma wavelength increases as the plasma wave amplitude increases. Hence, in the limit  $\phi_s^2 \ll 1$ , the nonlinear plasma wave number is given by

$$k_{Np} \simeq k_p(1 - 3\phi_s^2/16). \quad (29)$$

The detuning and saturation of the plasma wave can be estimated as follows. The growth of the plasma wave will stop when the phase difference between the laser beat wave and the plasma wave is  $\pi/2$ , i.e.,  $\int d\zeta(k_p - k_{Np}) \simeq \pi/2$ . Using the linear result for the plasma wave amplitude,  $\phi_s = a_1 a_2 k_p |\zeta|/4$ , yields a detuning distance  $L_t = (2\pi/a_1^2 a_2^2)^{1/3} 4/k_p$ . Hence, the plasma wave amplitude will saturate after a distance  $L_t$  behind the front of the laser beam, which gives a plasma wave amplitude of  $\phi_{\text{sat}} = (2\pi a_1 a_2)^{1/3} = E_{\text{max}}/E_0$ . A more careful derivation [75] of resonant detuning yields a maximum value of the electric field at saturation of

$$E_{\text{max}}/E_0 = (16a_1 a_2/3)^{1/3}, \quad (30)$$

which assumes that the laser beat frequency is exactly equal to the ambient plasma frequency  $\Delta\omega = \omega_p$ . Saturation occurs because the plasma wave period increases as the wave grows. Hence, to partly compensate for the increasing nonlinear plasma period, the plasma wave can be driven to higher amplitudes by using a laser beat period which is slightly longer [76]. In other words, the beat frequency is slightly detuned such that  $\Delta\omega < \omega_p$ . Tang et al. [76] showed that the optimum detuning, which maximizes the plasma wave amplitude at saturation, is given by

$$\Delta\omega_{\text{opt}}/\omega_p = 1 - (9a_1 a_2)^{2/3}/8. \quad (31)$$

This gives a maximum saturation amplitude of

$$E_{\text{max}}/E_0 = 4(a_1 a_2/3)^{1/3}. \quad (32)$$

The above results are valid in the limit of weak pump amplitudes  $a_1 a_2 \ll 1$  for which the plasma wave is driven to saturation over a large number of beat periods. In the highly nonlinear regime,  $a_1 a_2 \gtrsim 1$ , however, the same general concepts apply to beat wave generation, i.e., the beat wave amplitude is limited by the increasing nonlinear plasma wavelength and the beat wave amplitude can be optimized by increasing the beat wave period such that  $\Delta\omega < \omega_p$ . To illustrate this, (13) is solved numerically [95] for a laser beat wave consisting of four beat periods, as shown in Fig. 7. The amplitudes of the lasers are  $a_1 = a_2 = a_0$ , with  $a_0 = 1.2$ , and linear polarization is assumed, such that  $(a_1 a_1)_s = a_0^2/2$ , where the subscript  $s$  refers to an averaging over the fast laser period. The ambient plasma density is  $n_0 = 10^{16} \text{ cm}^{-3}$  ( $\lambda_p = 330 \mu\text{m}$ ).

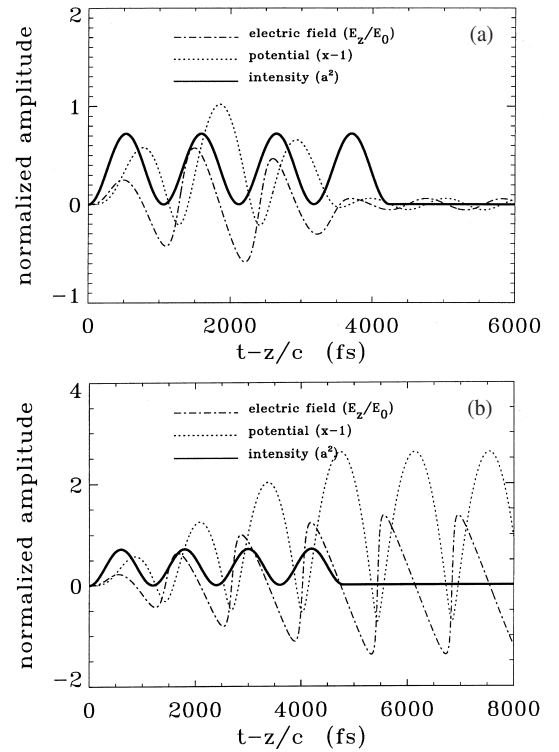


FIG. 7: Examples of PBWA consisting of four beat pulses with  $a_0 = 1.2$  in a plasma of density  $n_0 = 10^{16} \text{ cm}^{-3}$ : (a) without optimization  $\Delta\omega = \omega_p$ , showing the effects of detuning, and (b) with optimization  $\Delta\omega < \omega_p$ . Normalized intensity profile  $a^2$  (solid curve), wake potential  $\phi$  (dotted curve), and axial field  $E_z/E_0$  (dashed curve) versus  $t - z/c$ . Pulses are linearly polarized (moving to the left)

The case  $\Delta\omega = \omega_p$  is shown in Fig. 7(a), and it is clear that the plasma wave amplitude saturates (reaches maximum amplitude) after just the second beat pulse. The effect of the third and fourth beat pulses is to drive the plasma wave down to a low amplitude. In Fig. 7(b) the beat period has been optimized numerically such that the plasma wave amplitude after the fourth beat pulse is maximized, i.e., the beat period is increased  $\Delta\omega < \omega_p$  such that the length of the beat pulse is closer to the final nonlinear plasma wavelength  $\lambda_{Np}$ . This results in a dramatic increase in the final amplitude of the plasma wave electric field,  $E_{\text{max}} \simeq 1.4 E_0 = 13 \text{ GV/m}$ , in comparison to the  $\Delta\omega = \omega_p$  case.

In addition to resonant detuning, the plasma wave amplitude in the PBWA can be limited by laser-plasma instabilities. Experiments at Ecole Polytechnique observed saturation of the beat-generated plasma wave by a parametric coupling to ion waves [96]. In general, since the laser pulse lengths in the PBWA are long,  $L > \lambda_p$ , the beams are subject to various laser-plasma instabilities, which are discussed in Sect. VI.

The observation of plasma wave generation in the PBWA via Thomson scattering was first demonstrated by Clayton et al. [97] and later observed by several groups

[28, 87, 96]. Acceleration of background plasma electrons in the PBWA was first observed by Kitagawa et al. [28] using two lines of a CO<sub>2</sub> laser in a plasma of density  $10^{17} \text{ cm}^{-3}$ . Plasma electrons were trapped and accelerated to an energy in excess of 10 MeV. A plasma wave amplitude of  $\delta n/n_0 = 0.05$  was observed and an acceleration gradient of 1.5 GV/m was estimated. Clayton et al. [87] observed electron acceleration in a series of PBWA experiments performed at the University of California at Los Angeles (UCLA) using two lines of a CO<sub>2</sub> laser in a plasma of density  $9 \times 10^{15} \text{ cm}^{-3}$ . A 28 MeV energy gain was observed using a 2 MeV injected electron beam, corresponding to a gradient of 2.8 GV/m and a plasma wave amplitude of  $\delta n/n_0 = 0.28$ . The UCLA experiments were particularly well diagnosed and various laser-plasma interaction phenomena and instabilities have been observed [98–100]. In experiments at Ecole Polytechnique, Amiranoff et al. [31] observed acceleration in a PBWA experiment using two Nd laser lines in a plasma of density  $10^{17} \text{ cm}^{-3}$ . The energy of a 3.4 MeV injected electron beam was observed to increase by 1.4 MeV. A plasma wave amplitude of 2% and a gradient of 0.6 GV/m were observed. Plasma wave saturation and parametric coupling to ion waves were also observed in these experiments [31].

### C. Multiple Laser Pulses

In the previous section discussing the PBWA, it was pointed out that (i) the laser beat wave acted in effect as a series of short laser pulses, (ii) as the plasma wave grew the plasma period increased which led to a loss of resonance with respect to the laser beat pulses, and (iii) the beat period, i.e., the width of the beat pulses, could be adjusted and optimized to maximize the plasma wave amplitude. These general principles can be extended to describe plasma wave generation by a series of short laser pulses [46–50]. For example, the resonant laser-plasma accelerator [48] uses an optimized train of short laser pulses to drive a plasma wave, in which the width of each pulse and the spacing between pulses is independently controlled. By optimizing the pulse widths and interpulse spacings, resonance with the plasma wave can be maintained and saturation of the plasma wave by resonant detuning can be eliminated. A sequence of  $m$  pulses is optimized when the pulse widths and spacings are chosen to maximize the plasma wave amplitude.

For square pulses in the linear regime ( $a^2 \ll 1$  and  $E_{\text{max}}/E_0 \ll 1$ ), the optimum pulse train consists of  $m$  identical pulses, each of width  $L = \lambda_p/2$  and separated by a distance  $(2\ell + 1)\lambda_p/2$ , where  $\ell$  is an integer. The plasma wave amplitude will be  $m$  times the single pulse value,  $E_{\text{max}}/E_0 = ma_0^2$ . This result neglects nonlinear effects. In particular, as the nonlinear plasma wavelength increases, resonant detuning will eventually saturate the plasma wave amplitude.

In the nonlinear regime, however, resonance can only

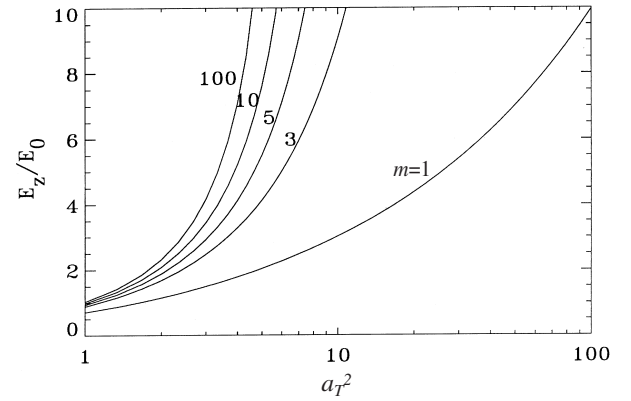


FIG. 8: Maximum electric field amplitude  $E_z/E_0$  versus  $a_T^2 = ma_0^2$ , for  $m = 1, 3, 5, 10,$  and  $100$  optimized square laser pulses with  $a_0 = 1$

be maintained by optimizing both the pulse widths and spacings of each individual pulse. In the 1D limit with  $\omega_p^2/\omega^2 \ll 1$ , this can be examined by solving (13). For square pulse profiles, analytic solutions can be obtained. It can be shown [49, 50] that the optimal width of the  $m$ th pulse  $L_m$ , the nonlinear wavelength  $\lambda_{Nm}$  of the wake behind the  $m$ th pulse, and the electric field amplitude  $E_{zm}$  of the wake behind the  $m$ th pulse are given by

$$L_m = (2/k_p)x_m^{1/2}E_2(y_m), \quad (33)$$

$$\lambda_{Nm} = (4/k_p)x_m^{1/2}E_2(\hat{y}_m), \quad (34)$$

$$E_{zm}/E_0 = x_m^{1/2} - x_m^{-1/2}, \quad (35)$$

where  $x_m = \gamma_{\perp 1}^2 \gamma_{\perp 2}^2 \cdots \gamma_{\perp m}^2$ ,  $\gamma_{\perp m}^2 = 1 + a_m^2$ ,  $a_m$  is the amplitude of the  $m$ th pulse,  $E_2$  is the complete elliptic integral of the second kind,  $y_m^2 = 1 - \gamma_{\perp m}^2 x_m^{-1/2}$  and  $\hat{y}_m^2 = 1 - x_m^{-1/2}$ . The optimal spacing between the end of the  $m$ th pulse and the beginning of the  $m$ th+1 pulse is given by  $(2\ell + 1)\lambda_{Nm}/2$  ( $\ell = \text{integer}$ ). The maximum normalized electric field of the wake  $E_{\text{max}}/E_0$ , for an optimized train of  $m$  square pulses of equal amplitudes  $a_m = a_0$ , is plotted in Fig. 8 versus the quantity  $a_T^2 = ma_0^2$  [49, 50]. The curves show the results for 1, 3, 4, 10, and 100 pulses. In the linear regime,  $E_{zm} = mE_{z1} = ma_0^2 E_0$ , i.e., these curves are just straight lines. Figure 8, however, shows that in the nonlinear regime,  $m$  pulses are more efficient than the linear result, i.e.,  $E_{zm} > mE_{z1}$ . In the highly nonlinear regime, this enhancement can be quite dramatic. Furthermore, Fig. 8 indicates that just a few optimized square pulses are far more efficient than a single pulse.

For square pulse profiles, both the width of the pulse and the spacing between pulses increases for subsequent pulses in the train, since the nonlinear wavelength of the plasma wave is increasing. For more realistic pulse profiles, this is not necessarily the case. Consider the

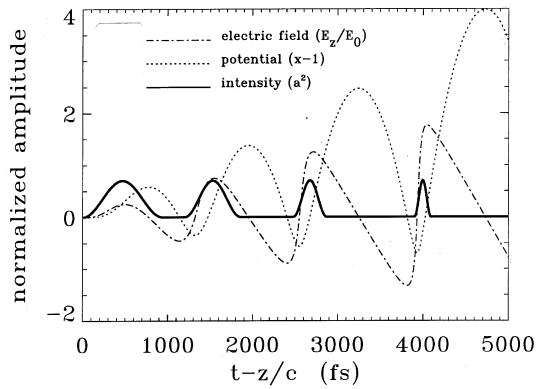


FIG. 9: Laser pulse train consisting of four optimized sine-shaped laser pulses with  $a_0 = 1.2$  and  $n_0 = 10^{16} \text{ cm}^{-3}$ . Normalized intensity profile  $a^2$  (solid curve), wake potential  $\phi$  (dotted curve), and axial field  $E_z/E_0$  (dashed curve) are plotted vs. the comoving variable  $t - z/c$ . Pulses are linearly polarized (moving to the left)

case in which the electric field envelope of each pulse is modeled by a half period of a sine function, e.g.,  $a = a_1 \sin(\pi\zeta/L_1)$ , with  $0 < \zeta < L_1$ , for the first pulse. The result from a numerical optimization [49, 50] of (13) for a train of four sine pulses is shown in Fig. 9. Here, the plasma density is  $n_0 = 10^{16} \text{ cm}^{-3}$  and the pulses are linearly polarized with equal amplitudes  $a_m = a_0 = 1.2$ . Notice that the pulse width is decreasing, i.e., the width of the first pulse is 940 fs, whereas the width of the fourth laser pulse is 200 fs. From Fig. 9, it can be seen that the pulses are optimized when they reside in the region of the plasma wave for which  $\phi < 0$  and  $d\phi/d\zeta < 0$ , where  $\zeta = z - ct$ . This is the phase region of the plasma wave for which the laser pulse drives the plasma wave most efficiently. As in the square wave case,  $\lambda_{Nm}$ , and thus the spacing between pulses, increases with each succeeding pulse. For this example, the total laser fluence for the pulse train is  $I\tau_{\text{tot}} = 2.2 \text{ MJ/cm}^2$  and the final accelerating field is  $E_{\text{max}} \simeq 1.9 E_0 = 18 \text{ GV/m}$ .

Several techniques may generate a train of short, intense pulses using CPA laser systems [49, 50]. One possible method is to divide the amplified stretched pulse by use of beam splitters, then send the separate pulses to separate compressors with adjustable lengths and delays. Alternatively, Fourier filtering can be used by placing a mask in the pulse stretcher to modify the phase and/or amplitude of the frequency components of the pulse in such a way that, when it is recompressed, a series of pulses with arbitrary spacings and widths will be produced. Preliminary experiments on similar methods have been reported [101].

#### D. Self-Modulated Laser Wakefield Accelerator

In the previous section it was described how a train of laser pulses can be used to generate a large amplitude

wakefield. Under appropriate conditions, however, it is possible for a single, long laser pulse to break up into a train of short pulses, each of these short pulses having a width on the order of  $\lambda_p$ . Associated with the break up of the long pulse and the formation of the pulse train is a large amplitude plasma wave. This process is referred to as self-modulation [12, 36–45, 52, 102, 103] and was first observed in fluid simulations [36–38] of relativistically guided laser pulses. Physically, self-modulation occurs from the plasma wave producing periodic regions of enhanced focusing and diffraction [104]. The self-modulation instability resembles a highly 2D version of a forward Raman instability. Forward Raman scattering occurs simultaneously, adding to the modulation, and in the 1D limit, pulse modulation can occur via forward Raman scattering alone [105].

The process by which a plasma wave can modulate a laser pulse by producing periodic regions of enhanced focusing and diffraction was first described and analyzed by Esarey et al. [94]. The self-modulation of relativistically-guided laser pulses was observed in the simulations of Andreev et al. [38], Sprangle et al. [36], and Antonsen and Mora [37, 106]. Krall et al. [73] simulated a self-modulated LWFA, including the acceleration of an injected electron beam, and showed that this configuration can have certain advantages over the standard LWFA. The self-modulation instability was subsequently analyzed by Esarey et al. [104] and Andreev et al. [107, 108] and, in the 1D limit, RFS was analyzed by Mori et al. [105]. Extensive particle-in-cell simulations of short, intense pulses propagating in the high density regime have been carried out by Decker et al. [71] and Bulanov et al. [72].

To operate in the self-modulated regime [36, 37, 52, 73, 104, 106–108], it is desirable that (i) the pulse length be long compared to the plasma wavelength,  $L > \lambda_p$ , and (ii) the pulse power to be larger than the power required to guide a long laser beam,  $P > P_c(1 - \Delta n/\Delta n_c)$ . Here,  $P_c = 17(\omega/\omega_p)^2 \text{ GW}$  is the critical power required for relativistic optical guiding,  $\Delta n$  is the depth of a preformed parabolic density channel (if present),  $\Delta n_c = 1/\pi r_e r_0^2$  is the critical channel depth, and  $r_e$  is the classical electron radius. The optical guiding of laser pulses by relativistic effects and density channels will be discussed more completely in the Sect. V. In the remainder of this section, it will be assumed that the laser pulse is propagating in an initially uniform plasma ( $\Delta n = 0$ ). Since  $\lambda_p \propto n_0^{-1/2}$  and  $P_c \propto n_0^{-1}$ , for fixed laser parameters, the conditions  $L > \lambda_p$  and  $P > P_c$  can usually be satisfied by operating at a sufficiently high plasma density.

Consider the possibility of generating wakefields with a 300 fs ( $L = 90 \mu\text{m}$ ) laser pulse of wavelength  $\lambda = 1 \mu\text{m}$  and power  $P = 10 \text{ TW}$ . To operate in the standard LWFA configuration,  $L \simeq \lambda_p$  implies a density of  $n_0 \simeq 1.4 \times 10^{17} \text{ cm}^{-3}$ . At this density  $P \ll P_c \simeq 140 \text{ TW}$  and the effects of relativistic guiding are unimportant. To operate in the self-modulated regime, it is desirable that  $L > \lambda_p$  and  $P > P_c$ . Choosing a plasma density

such that  $P = 1.5 P_c$  implies  $n_0 \simeq 2.8 \times 10^{18} \text{ cm}^{-3}$  and  $L \simeq 4.5 \lambda_p$ . Hence, for this laser pulse, the self-modulated regime can be reached by increasing the plasma density by a factor of 20 compared to the standard LWFA configuration. Furthermore, the corresponding energy gain can be enhanced by nearly a factor of 10 compared to the standard LWFA configuration, as is indicated by simulations discussed below.

The advantages of the self-modulated LWFA over the standard LWFA are simplicity and enhanced acceleration. Simplicity in that a matching condition of  $L \simeq \lambda_p$ , a preformed density channel, or special pulse tailoring are not required. Enhanced acceleration is achieved for several reasons: (i) The self-modulated LWFA operates at higher density, hence a larger wakefield will be generated, since  $E_z \propto 1/\sqrt{n_0}$ , as indicated by (11). (ii) Since  $P > P_c$ , the laser pulse will tend to focus to a higher intensity, thus increasing  $a_0$  and  $E_z$ . (iii) The wakefield is resonantly excited, i.e., excited by a series of beamlets as opposed to a single pulse as in the standard LWFA. (iv) Relativistic optical guiding allows the modulated pulse structure to propagate for several Rayleigh lengths, thus extending the acceleration distance. The disadvantages of the self-modulated LWFA are (i) at higher densities the laser pulse group velocity ( $\simeq$  the plasma wakefield phase velocity) decreases and, hence, electron dephasing from the plasma wakefield can limit the acceleration distance, and (ii) the modulated pulse structure eventually diffracts.

The properties of the self-modulated LWFA are illustrated by the following simulations [73]. For fixed laser pulse parameters, two cases will be considered: (1) a standard LWFA in which  $L \simeq \lambda_p$  and  $P < P_c$  and (2) a self-modulated LWFA, in which  $L > \lambda_p$  and  $P > P_c$ . The laser parameters for both these cases are identical: a Gaussian axial intensity profile with a pulse length  $L = 90 \mu\text{m}$  (300 fs),  $\lambda = 1 \mu\text{m}$ ,  $a_0 = 0.7$ ,  $r_0 = 31 \mu\text{m}$  (in vacuum, which corresponds to  $Z_R = 3 \text{ mm}$ ),  $P = 10 \text{ TW}$ , and a pulse energy of 1.5 J. The simulation begins at  $t = 0$  as the laser pulse enters the plasma, initially converging such that in vacuum it would focus to a minimum spot size of  $r_0 = 31 \mu\text{m}$  at  $ct = 3Z_R$ . The plasma density is initially increasing, reaching full density at  $ct = 2Z_R$ . The simulation continues until  $ct = 10Z_R = 3 \text{ cm}$ . In both cases, the acceleration and trapping of a continuous electron beam with initial energy of 3 MeV and normalized emittance  $\varepsilon_n = 130 \text{ mm-mrad}$  is considered. The electron beam is initially converging such that in vacuum it would focus to a minimum RMS radius  $r_b = 200 \mu\text{m}$  at  $ct = 3Z_R$ . With such a large initial emittance, only a small fraction ( $\sim 1\%$ ) of the particles will be trapped and accelerated.

For the standard LWFA, Case (1), the requirement  $L = \lambda_p = 90 \mu\text{m}$  implies a density of  $n_0 = 1.4 \times 10^{17} \text{ cm}^{-3}$ . At this density,  $P \ll P_c = 140 \text{ TW}$ , such that relativistic guiding effects are unimportant. The presence of the plasma has little effect on the evolution of the laser pulse, which reaches a peak intensity of  $|a|^2 = 0.56$  at  $ct = 3Z_R$ .

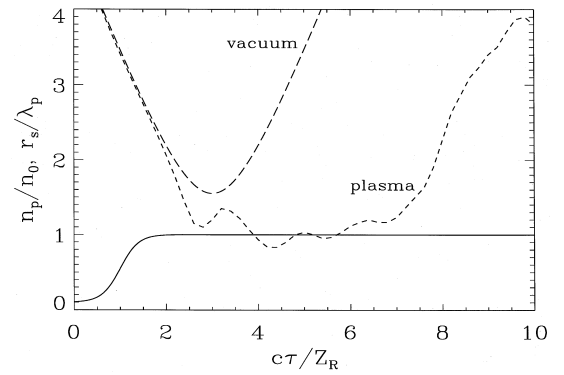


FIG. 10: Ambient plasma density  $n_p/n_0$  (solid curve) and spot size  $r_s/\lambda_p$  (dashed curve) versus normalized propagation distance  $ct/Z_R$  for a self-modulated LWFA with  $n_0 = 2.8 \times 10^{18} \text{ cm}^{-3}$ . Laser is initially converging such that the minimum spot size in vacuum is reached at  $ct = 3Z_R$

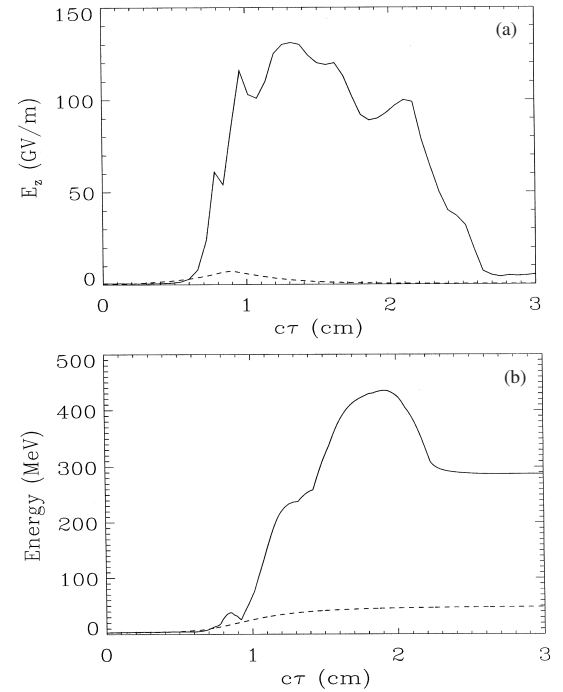


FIG. 11: (a) Peak accelerating field and (b) peak energy of the injected particles versus propagation distance  $ct$  for the standard LWFA (dashed curve) with  $n_0 = 1.4 \times 10^{17} \text{ cm}^{-3}$  and the self-modulated LWFA (solid curve) with  $n_0 = 2.8 \times 10^{18} \text{ cm}^{-3}$

The evolution of the spot size, Fig. 10, is very close to vacuum diffraction. This is also evident in Fig. 11(a) (dashed line), where the peak accelerating field, plotted versus time, is symmetric about the focus,  $ct = 3Z_R$ . After  $ct = 10Z_R = 3 \text{ cm}$ , a small fraction ( $\sim 0.1\%$ ) of the test electron beam particles have been trapped and accelerated. At  $ct = 2 \text{ cm}$ , the peak particle energy is 48 MeV, which implies an average acceleration of  $2.4 \text{ GeV/m}$ , as shown in Fig. 11(b) (dashed line).

For the self-modulated LWFA, Case (2), the density is increased such that  $P = 1.5P_c = 10$  TW, which implies  $n_0 = 2.8 \times 10^{18} \text{ cm}^{-3}$ , which is 20 times higher than in Case (1). At this density  $L > \lambda_p = 20 \mu\text{m}$ , i.e., the laser pulse now extends over  $\simeq 4.5 \lambda_p$ . Figure 12 shows the laser intensity at (a)  $ct = 2Z_R$  and (b)  $ct = 3.2Z_R$ . The axial electric field and the plasma density response on-axis at  $ct = 3.2Z_R$  are shown in Figs. 13(a) and 13(b), respectively. The laser pulse has become modulated (three peaks are observable, separated by  $\lambda_p$ ) and the plasma wave is highly nonlinear. In addition, relativistic optical guiding effects have focused the laser to a much higher intensity than was observed in Case (1). The evolution of the laser spot size is shown in Fig. 10 indicating that the pulse has focused to a smaller spot size and remains guided over  $\simeq 5.5Z_R$ . A plot of the peak accelerating field versus time, Fig. 11(a) (solid line), shows that the highly nonlinear fields persist as the laser pulse is optically guided. A maximum accelerating field of  $\simeq 130$  GV/m was obtained. Because of the larger fields, a greater fraction (2%) of the test electron beam particles were trapped and accelerated. The peak particle energy of 430 MeV is observed at  $ct = 6Z_R = 1.8$  cm. At  $ct = 10Z_R = 3$  cm, however, the peak particle energy has dropped to 290 MeV due to the reduced group velocity of the laser pulse, which causes the electrons to slip out of phase with the wakefield and become decelerated. Figure 11(b) (solid line) shows acceleration to 430 MeV over 1.8 cm which gives an average gradient of 24 GeV/m. This is an order of magnitude increase compared to the standard LWFA of Case (1). In the above fluid simulations, the excited plasma wave was below wavebreaking, and an externally injected electron beam was used. However, in the experiments discussed below, it is possible to drive the plasma wave in the self-modulated regime to wavebreaking, resulting in copious amounts of self-trapped electrons, albeit with large energy spread.

Evidence for plasma wave generation in the high-density, self-modulated regime was first detected by Coverdale et al. [40]. The presence of a plasma wave leads to the generation of Stokes and anti-Stokes lines in the frequency spectrum of the pump laser pulse. The first two anti-Stokes lines were observed by Coverdale et al., the appearance of which were correlated with production of fast electrons, as discussed below. Subsequently, multiple anti-Stokes lines in the forward spectrum of the pump laser have been observed by several other groups [41, 42, 109]. At the Naval Research Laboratory [109], plasma wave generation in the self-modulated regime was measured via coherent Thomson scattering with a frequency-doubled probe pulse. The evolution of the plasma wave was observed by varying the time delay between the pump and probe pulses.

Joshi et al. [39] detected fast electrons in an early experiment via forward Raman scattering. A single, long (700 ps),  $\text{CO}_2$  laser pulse of modest intensity ( $10^{15} \text{ W/cm}^2$ ) interacting with a thin Carbon foil was observed to produce 1.4 MeV electrons. Electron accel-

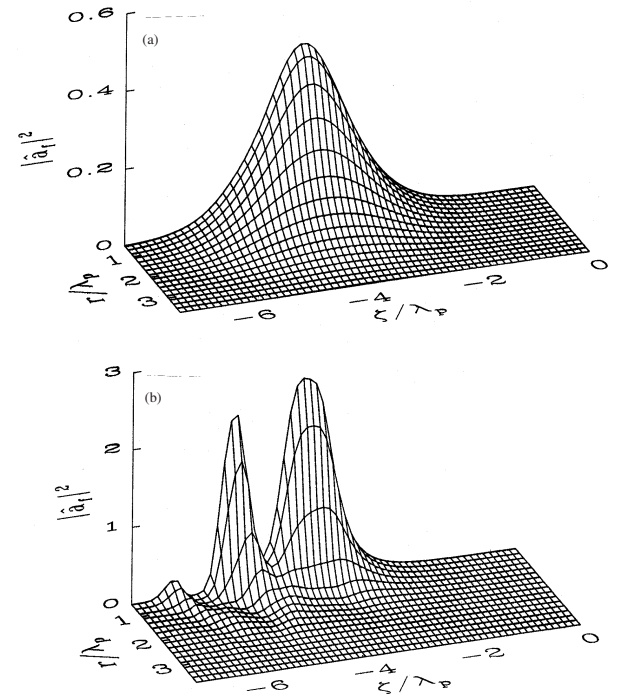


FIG. 12: Normalized laser intensity  $|a|^2$  for the self-modulated LWFA case at (a)  $ct = 2Z_R$  and (b)  $ct = 3.2Z_R$ . Laser pulse is moving to the right

ation in the high-density, self-modulated regime has been observed using ultrashort pulses ( $\lesssim 1$  ps). Nakajima et al. [102] observed electron acceleration to energies  $\geq 18$  MeV using a 3 TW, 1 ps,  $10^{17} \text{ W/cm}^2$  laser pulse in a plasma of density near  $10^{19} \text{ cm}^{-3}$ . A laser-solid interaction was used to produce a source of injected electrons with energies near 1 MeV. Particle simulations in 1D suggest acceleration gradients on the order of 30 GV/m. Coverdale et al. [40] observed 2 MeV electrons, which were trapped and accelerated from the background plasma, when a 600 fs, 5 TW,  $8 \times 10^{17} \text{ W/cm}^2$  laser pulse propagated in a plasma of density  $2 \times 10^{19} \text{ cm}^{-3}$ . The generation of electrons was also correlated with the occurrence of anti-stoke lines in the laser pulse spectrum, which indicates the presence of a plasma wave. Modena et al. [41] demonstrated the acceleration of self-trapped electrons to energies  $\geq 44$  MeV (limit of the detector) using a 1 ps, 20 TW,  $5 \times 10^{18} \text{ W/cm}^2$  laser pulse in a plasma of density  $1.5 \times 10^{19} \text{ cm}^{-3}$ . A large flux of electrons was observed ( $10^6$  electrons/MeV at 44 MeV) and the electron signal was correlated to the appearance of up to 5 anti-Stokes lines in the laser spectrum. Estimates based on the electron dephasing length imply an acceleration gradient  $> 100$  GV/m. Acceleration of self-trapped electrons has also been observed by Wagner et al. [42]. The electrons were emitted in a well-collimated beam in the forward direction (a divergence angle  $\simeq 8^\circ$ ) and the cross-section of the beam resembled the shape of the cross-section of the laser at focus. By varying the laser pulse energy,

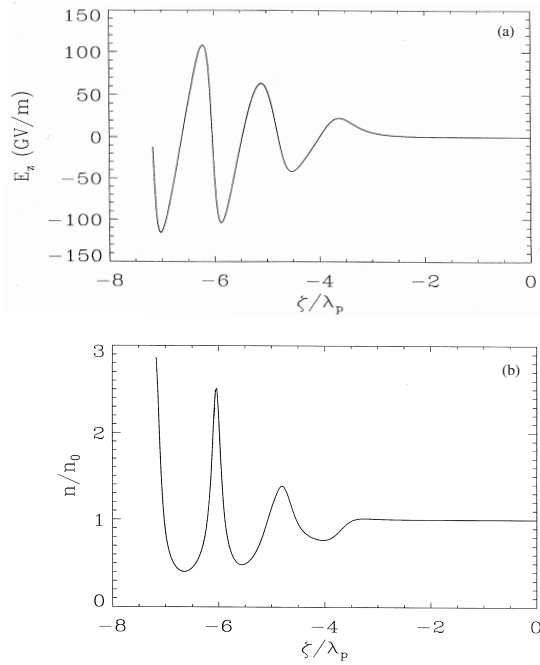


FIG. 13: (a) Axial electric field  $E_z$  and (b) normalized plasma electron density  $n/n_0$  versus  $\zeta$  at  $c\tau = 3.2Z_R$  for the self-modulated LWFA case

a threshold for electron acceleration was observed near  $P \simeq P_c$ . Subsequently, other research groups have measured energetic electron production in the self-modulated regime [12, 43–45].

Experiments at Lawrence Berkeley National Laboratory (LBNL) have shown the importance of pulse shape on self-modulation and electron production [103]. These experiments compared electron production for laser pulses with slow and fast rise times. For fast rise times the ponderomotive force is larger, resulting in a larger initial plasma wave, which acts as the seed for the self-modulation instability [110]. Experiments and simulations by Malka et al. [13] have discussed an intermediate regime between the standard and self-modulated LWFA, in which the laser pulse is only somewhat longer than the plasma wavelength. In this regime, the pulse undergoes significant self-steepening, resulting in enhanced plasma wave generation.

Another process that can contribute to acceleration in the self-modulated regime ( $\lambda_p < L$  and  $P > P_c$ ) is direct laser acceleration [111]. In this mechanism, it is necessary that the accelerated electrons undergo transverse betatron oscillations. When the betatron frequency  $\omega_\beta$  is near the laser frequency in the frame of the accelerated electrons,  $\omega \sim 2\omega_\beta\gamma^2/\gamma_\perp^2$ , energy can efficiently exchange between the electrons and the transverse laser field. This is the inverse process of the electromagnetic instability responsible for the ion channel laser [112]. The transverse betatron oscillations are produced by a transverse force that can result from a variety of mechanisms, e.g., the radial structure of the plasma wave

( $\phi = \phi_0 \exp(-2r^2/r_0^2) \cos[k_p(z - ct)]$ ) for a Gaussian laser in the linear regime), forces resulting from induced magnetic fields, or, in the blowout regime, from the formation of an ion channel through the expulsion of background plasma electrons by the radial ponderomotive force of the laser. In the blowout regime ( $\phi_0 \sim k_p^2 r_0^2/8$ ), the electrons oscillate with the betatron frequency  $\omega_\beta \simeq \omega_p/(2\gamma)^{1/2}$  [113]. Gahn et al. [114] have reported multi-MeV electrons accelerated by a 1.2 TW, 200 fs laser pulse channeling in a high-density ( $10^{20} \text{ cm}^{-3}$ ) plasma, and have attributed the dominant acceleration process to direct laser acceleration.

### E. Limits on Laser-Driven Acceleration

Several mechanisms can limit the energy gain in a laser driven accelerator: laser diffraction, electron dephasing, pump depletion, and laser-plasma instabilities. In vacuum a laser pulse undergoes Rayleigh diffraction, i.e., the laser spot size evolves according to  $r_s = r_0(1 + z^2/Z_R^2)^{1/2}$ , where  $r_0$  is the minimum spot size at the focal point  $z = 0$  and  $Z_R = kr_0^2/2$  is the Rayleigh length. Without some form of optical guiding, the laser-plasma interaction distance will be limited to a few  $Z_R$ . Electron dephasing, i.e., a highly relativistic electron outrunning the plasma wave, can limit the energy gain to a dephasing length  $L_d$ , as discussed in Sect. II F. As the laser driver excites a plasma wave, it loses energy, i.e., it pump depletes [89, 115–117]. The pump depletion length  $L_{pd}$  can be estimated by equating the laser pulse energy to the energy left behind in the wakefield,  $E_z^2 L_{pd} \simeq E_L^2 L$ , where  $E_L$  is the laser field.

As an illustration, consider a LWFA in the standard configuration driven by a circularly polarized, square profile laser pulse with  $L \simeq \lambda_{Np}/2$ . The dephasing and pump depletion lengths are given by [115–117]

$$L_d \simeq (\omega^2/\omega_p^2)\lambda_p \begin{cases} 1, & \text{for } a_0^2 \ll 1, \\ 2a_0^2/\pi, & \text{for } a_0^2 \gg 1, \end{cases} \quad (36)$$

$$L_{pd} \simeq (\omega^2/\omega_p^2)\lambda_p \begin{cases} a_0^{-2}, & \text{for } a_0^2 \ll 1, \\ a_0/3\pi, & \text{for } a_0^2 \gg 1. \end{cases} \quad (37)$$

For the parameters  $a_0 = 0.5$ ,  $\lambda = 1 \mu\text{m}$ , and  $r_0 = \lambda_p = 33 \mu\text{m}$  ( $P = 6 \text{ TW}$  and  $n_0 = 10^{17} \text{ cm}^{-3}$ ), the relevant propagation lengths are  $Z_R = 0.34 \text{ cm}$ ,  $L_d \simeq 3.6 \text{ cm}$ , and  $L_{pd} \simeq 14 \text{ cm}$ , i.e.,  $Z_R \ll L_d < L_{pd}$ . Furthermore, since  $L_d, L_{pd} \propto n_0^{-3/2}$ , the dephasing length and pump depletion lengths can be increased by operating at lower densities. Since  $L \sim \lambda_p$  in the standard LWFA, lower densities correspond to longer laser pulse durations  $L \propto 1/\sqrt{n_0}$ . In principle, a static magnetic field can be introduced to reduce dephasing [93]. Use of an active medium has also been proposed as a method to reduce pump depletion [118].

The energy gain in the standard LWFA for a laser pulse undergoing vacuum diffraction is given by  $\Delta W_v \simeq e\pi Z_R E_z$  which, in the limit  $a_0^2 \ll 1$ , can be written as [119]

$$\Delta W_v (\text{MeV}) \simeq 580(\lambda/\lambda_p)P(\text{TW}). \quad (38)$$

To increase the energy gain beyond this value in a single stage, some form of optical guiding, such as the use of a plasma density channel, is necessary in order to prevent diffraction. Various methods for optical guiding are discussed in Sect. V. If diffraction is overcome, dephasing will limit the energy gain. In the standard LWFA, the single-stage energy gain after a dephasing length  $\Delta W_d = eL_d E_z$  can be written in the limit  $a_0^2 \ll 1$  as [120]

$$\Delta W_d (\text{GeV}) \simeq I_0 (\text{W/cm}^2)/n_0 (\text{cm}^{-3}). \quad (39)$$

These estimates neglect pump depletion and assume that laser-plasma instabilities do not significantly degrade the laser pulse. The effects of various instabilities are discussed in Sect. VI.

In the linear regime ( $a_0^2 \ll 1$ ),  $L_d \ll L_{pd}$  and the electron energy gain is limited by dephasing, not pump depletion, assuming an axially uniform plasma. However, by appropriately tapering the axial plasma density profile, dephasing limitations can be overcome, resulting in a larger single-stage energy gain [121]. By slowly increasing the plasma density as a function of propagation distance, the phase velocity of the wakefield can be increased, as is described in Sect. IV C. In principle, an axial density taper can be found for which  $v_p = c$  at some point behind the drive laser pulse. In this case, acceleration would be limited by pump depletion,  $L_{pd} \sim (\lambda_p^3/\lambda^2)a_0^{-2}$ .

In the nonlinear regime ( $a_0^2 \gtrsim 1$ ),  $L_d \gtrsim L_{pd}$  and no density tapering is needed, since the electron energy gain is limited by pump depletion, not dephasing. In particular, the regime  $a_0^2 \sim 1$ , such that  $L_d \sim L_{pd}$ , has advantages over the linear regime. In addition to not requiring density tapering, a single channel-guided stage with  $a_0^2 \sim 1$  results in higher accelerating gradients, shorter channel lengths, efficient depletion of the laser pulse energy, while yielding comparable energy gains.

## F. Beam Loading

A relativistic, charged particle bunch moving through a plasma can excite a wake in a manner similar to that of an intense laser pulse. For a laser driver, the ponderomotive force expels plasma electrons and initiates a wake. For a relativistic electron bunch, the space charge force of the bunch (with a relativistically large mass) displaces plasma electrons (with a relativistically lighter mass) and initiates a wake. The larger the charge in the bunch, the larger the wake. In a plasma-based accelerator, the wake from the accelerated bunch will be out of phase with, and thus reduce, the wake generated by the drive beam. The

process by which the wake produced by the accelerated bunch significantly modifies the fields of the accelerating plasma wave is referred to as beam loading. Beam loading can place severe limitations on the beam current that can be accelerated, the quality of the accelerated particle bunch, and the efficiency of the plasma-based accelerator.

The wakefield generated by a relativistic electron bunch moving through a plasma can be calculated using linear perturbation theory of the cold fluid-Maxwell equations [56, 122]. The normalized density perturbation  $\delta n/n_0 < 1$  and normalized axial electric field  $E_z/E_0 < 1$  driven in an initially uniform plasma by a short electron bunch (with number density  $n_b$ ) are given by

$$\left(\frac{\partial^2}{\partial \zeta^2} + k_p^2\right) \frac{\delta n}{n_0} = -k_p^2 \frac{n_b}{n_0}, \quad (40)$$

$$(\nabla_{\perp}^2 - k_p^2) \frac{E_z}{E_0} = -k_p \frac{\partial}{\partial \zeta} \frac{\delta n}{n_0}, \quad (41)$$

using the quasi-static approximation and assuming a highly relativistic beam,  $\beta_b \simeq 1$ , where  $c\beta_b$  is the electron bunch velocity. Solving (40) yields

$$\delta n/n_0 = k_p \int_0^{\zeta} d\zeta' \sin[k_p(\zeta - \zeta')] n_b(\zeta')/n_0, \quad (42)$$

and, for a cylindrically-symmetric beam, solving (41) yields

$$E_z/E_0 = k_p^3 \int_{-\infty}^{\zeta} d\zeta' \int_0^{\infty} dr' r' \cos[k_p(\zeta - \zeta')] \times I_0(k_p r_{<}) K_0(k_p r_{>}) n_b(r', \zeta')/n_0, \quad (43)$$

where  $I_0$  and  $K_0$  are the zeroth-order modified Bessel functions of the second kind, and  $r_{<}$  ( $r_{>}$ ) denote the smaller (larger) of  $r$  and  $r'$ , respectively. An electron bunch will excite a plasma wave provided that the length scale of the axial gradients in the bunch profile (e.g., the bunch length) is comparable to or shorter than the plasma period, e.g.,  $k_p \sigma_z < 1$ , where  $\sigma_z$  is the bunch length. For a uniform bunch profile of radius  $r_b$  and length  $\sigma_z$ , assuming  $k_p \sigma_z \ll 1$ , the amplitude of the perturbed plasma density is  $\delta n/n_0 \simeq k_p \sigma_z (n_b/n_0)$  and the amplitude of the axial wakefield is

$$E_z/E_0 \simeq k_p \sigma_z F_R(r) n_b/n_0, \quad (44)$$

where the radial profile function is

$$F_R(r) = \begin{cases} 1 - k_p r_b K_1(k_p r_b) I_0(k_p r), & \text{for } r < r_b \\ k_p r_b I_1(k_p r_b) K_0(k_p r), & \text{for } r > r_b \end{cases} \quad (45)$$

with  $I_1$  and  $K_1$  the first-order modified Bessel functions. For a wide beam  $k_p r_b \gg 1$ ,  $F_R(0) \simeq 1$ . For a narrow beam  $k_p r_b \ll 1$ ,  $F_R(0) \simeq k_p^2 r_b^2 [0.577 + \ln(k_p r_b/2)]$ .

The maximum number of bunch electrons that can be loaded into a small ( $\ll \lambda_p$ ) axial segment of a linear wakefield for acceleration (i.e., the number of electrons

required to produce a wakefield that will cancel the accelerating field, which defines the beam loading limit) is [122]

$$N_{\max} = \frac{n_0 A_b}{k_p} \frac{E_z}{E_0} \simeq 5 \times 10^5 \left( \frac{E_b}{E_0} \right) A_b [\text{cm}^2] \sqrt{n_0 [\text{cm}^{-3}]}, \quad (46)$$

assuming  $E_z/E_0 < 1$ , where  $A_b \gg \pi/k_p^2$  is the cross-sectional area of the bunch. As the number of bunch electrons  $N$  approaches  $N_{\max}$ , the energy spread scales as  $N/N_{\max}$  and the efficiency of converting wake energy to electron energy scales as  $(N/N_{\max})(2 - N/N_{\max})$ .

## IV. ELECTRON TRAPPING AND INJECTION

### A. Trapping in the Self-Modulated LWFA

Perhaps the most basic and simplest form of a laser-plasma injector is the self-modulated LWFA, in which a single laser pulse results in self-trapping and generation of a sub-ps electron bunch, however, with a large energy spread. Typically the self-trapped bunch is of high charge (up to 10 nC), with an energy distribution characterized by a Boltzmann distribution with a few MeV temperature. One possible mechanism for self-trapping is the direct wavebreaking of the plasma wakefield [12, 41, 123]. Since the phase velocity of the wakefield is very near the speed of light, it is difficult to trap the background fluid electrons, which are undergoing the fluid oscillation that sustains the wakefield. The wake will trap the background electrons when the separatrix of the wake overlaps the plasma fluid orbit, which is the definition of wavebreaking, as discussed in Sect. IID. Wavebreaking of a cold plasma wave in 1D occurs at  $E_{\text{WB}} = [2(\gamma_p - 1)]^{1/2} E_0 \gg E_0$ . As discussed in Sect. IID thermal and 2D effects can lower this value, but typically wavebreaking requires nonlinear plasma waves with  $E_z > E_0$ . The observed wakefield amplitude, however, as measured in several experiments [109], appears to be in the range  $E_z/E_0 \sim 10\text{--}30\%$ , well below wavebreaking. This suggests that additional laser-plasma instabilities may play a role in lowering the effective wave breaking amplitude.

Alternatively, self-trapping and acceleration can result from the coupling of Raman backscatter (RBS) and Raman sidescatter (RSS) to the wakefield [124]. As the pump laser self-modulates, it also undergoes RBS, which is the fastest growing laser-plasma instability (cf. Sect. VIA). RBS is observed in intense short pulse experiments, with reflectivities as high as 10–30% [109, 125]. RBS generates red-shifted backward light of frequency  $\omega_0 - \omega_p$  and wavenumber  $-k_0$ , which beats with the pump laser  $(\omega_0, k_0)$  to drive a ponderomotive wave  $(\omega_p, 2k_0)$ . As the instability grows, the Raman backscatter beat wave, which has a slow phase velocity  $v_p \simeq \omega_p/2k_0 \ll c$ , can trap and heat background plasma electrons [39, 126]. These electrons can gain sufficient

energy and be displaced in phase by the beat wave such that they are trapped and accelerated to high energies in the wakefield. Simulations [124] indicate that coupling to RBS can lead to self-trapping at modest wakefield amplitudes,  $E_z/E_0 \simeq 0.25$ , much lower than the cold 1D threshold for direct wavebreaking.

In 2D, this process can be enhanced by coupling to RSS. As the scattering angle decreases from  $180^\circ$  (backscatter), the Raman growth rate decreases and the phase velocity of the Raman plasma wave increases. The electrons that are initially trapped and heated by RBS can be subsequently trapped by RSS modes propagating at smaller angles, which will accelerate the electrons to higher energies (owing to the higher phase velocity of the RSS modes) [39, 124]. Eventually, these background electrons can be trapped and accelerated to very high energies by the plasma wave associated with the forward Raman instability or the self-modulation instability, which has  $v_p \simeq c$ .

When electrons become trapped in the fast wakefield, they become accelerated to high energies as they circulate inside the separatrix of the wake. A large energy spread for the trapped electrons results because (i) some fraction of the background electrons are continually being swept up and trapped in the wakefield as the laser pulse propagates into fresh plasma, and (ii) typically the self-guided propagation distance of the laser pulse is much greater than the dephasing length for trapped electrons, cf. Sect. IIF. In the self-modulated regime the dephasing length can be very short, e.g.,  $L_d < 50 \mu\text{m}$ . This implies that deeply trapped electrons will circulate many revolutions within the separatrix, again resulting in a large energy spread. The maximum energy of the trapped electrons is given by the maximum of the separatrix, which corresponds to an energy  $W_{\max} \simeq 4\gamma_p^2 \gamma_\perp^{1/2} m_e c^2 E_z/E_0$ , for  $E_z/E_0 \ll 1$ , where  $\gamma_p$  is the phase velocity of the plasma wave.

For many applications, a small energy spread is desired. One method for improving the self-modulated bunch quality is by post-acceleration. For example, the self-modulated bunch could be immediately injected into a second-stage composed of a standard LWFA with  $L \sim \lambda_p$  in which the wakefield is produced in a controlled manner at an amplitude below the wavebreaking or self-trapping threshold. This could be achieved by using a plasma that transitions from a high plasma density ( $\lambda_p \ll L$ , self-modulated LWFA) to a low plasma density ( $\lambda_p \sim L$ , standard LWFA). Simulations [127] show that in this two-stage acceleration scheme, about 40% of the injected bunch charge can be trapped and accelerated in the LWFA with a reduce energy spread.

### B. Optical Injection Techniques

In principle, if a small energy spread electron bunch of duration small compared to  $\lambda_p$  is injected into the wakefield at the proper phase, then the bunch can be ac-

celerated while maintaining a small energy spread. This becomes problematic in the LWFA, since the wavelength of the accelerating field is small, e.g.,  $\lambda_p \simeq 30 \mu\text{m}$  for  $n_0 \simeq 10^{18} \text{cm}^{-3}$ . Hence, a low energy spread requires an ultrashort bunch duration  $\tau_b < \lambda_p/c$  that is injected at the optimal plasma wave phase with femtosecond timing accuracy. These requirements are beyond the capabilities of conventional electron beam injector technology (e.g., RF photo-injectors). On the other hand, the production of ultrashort laser pulses and the femtosecond timing of multiple pulses is routine with compact CPA technology. As discussed below, ultrashort, high intensity laser pulses can be used to inject electrons into a single bucket (plasma wave period) of a standard LWFA [128–131].

### 1. Ponderomotive injection

Umstadter et al. [128] first proposed using an additional laser pulse to inject background plasma electrons into the wake for acceleration to high energies. To generate ultrashort electron bunches with low energy spreads, the original laser injection method of [128] uses two laser pulses which propagate perpendicular to one another. The first pulse (pump pulse) generates the wakefield via the standard LWFA mechanism, and the second pulse (injection pulse) intersects the wakefield some distance behind the pump pulse. The ponderomotive force  $\mathbf{F}_p \simeq -(m_e c^2/\gamma)\nabla a^2/2$  of the injection pulse can accelerate a fraction of the plasma electrons such that they become trapped in the wakefield. Specifically, the axial (direction of propagation of the pump pulse along the  $z$ -axis) ponderomotive force of the injection pulse (propagating along the  $x$ -axis) scales as

$$F_z = -(m_e c^2/\gamma)(\partial/\partial z)a_1^2/2 \sim (m_e c^2/\gamma)a_1^2/r_1, \quad (47)$$

where  $a_1^2$  and  $r_1$  are the normalized intensity and spot size of the injection pulse, respectively. A simple estimate for the change of momentum that an electron will experience owing to the ponderomotive force of the injection pulse is  $\Delta p_z \simeq F_z \tau_1 \sim (m_e c^2/\gamma)a_1^2 \tau_1/r_1$ , where  $\tau_1$  is the injection pulse duration. It is possible for  $\Delta p_z$  to be sufficiently large that electrons are injected into the separatrix of the wakefield such that they become trapped and accelerated to high energies. To inject into a single plasma wave bucket, it is necessary for both the injection pulse spot size and pulse length to be small compared to the plasma wavelength, i.e.,  $r_1^2 \ll \lambda_p^2$  and  $c^2 \tau_1^2 \ll \lambda_p^2$ . Simulations [128], which were performed for ultrashort pulses at high densities ( $\lambda_p/\lambda = 10$  and  $E_z/E_0 = 0.7$ ), indicated the production of a 10 fs, 21 MeV electron bunch with a 6% energy spread. However, high intensities ( $I > 10^{18} \text{W/cm}^2$ ) are required in both the pump and injection pulses ( $a_0 \simeq a_1 \simeq 2$ ). In the work of Umstadter et al. [128], the pump and injection pulses do not overlap in space and time, and a laser beat wave is not generated, as discussed below.

Simulations by Hemker et al. [130] point out that additional electron injection into one or more wake buckets can result through the influence of the wake associated with the injection pulse, which can be significant because of the high intensity of the injection pulse ( $a_1 \gtrsim 1$ ). Umstadter et al. [128] also discuss the possibility of injection using an injection pulse that propagates parallel, but some distance behind, the pump pulse. The injection pulse would have a tighter focus (and hence smaller Rayleigh length) than the pump pulse, and would be phased appropriately such that it locally drives the wakefield to an amplitude that exceeds wavebreaking, thus resulting in local trapping and acceleration of electrons. In addition, [128] discusses the possibility of the injection pulse being focused to sufficiently high intensity such that it produces locally additional ionization. The ionized electrons, which are born dephased from the background plasma electron in the wake, could become trapped and accelerated by the wake. Injection by laser-induced ionization and ponderomotive acceleration has also been discussed by Moore et al. [132].

### 2. Colliding pulse injection

Beat wave injection using colliding laser pulses [129, 131, 133] differs intrinsically from the method of ponderomotive injection discussed above in that the source and form of the ponderomotive force differs in these two methods. In ponderomotive injection, injection is the result of the ponderomotive force associated with the *envelope* (time-averaged intensity profile) of a single pulse. In beat wave injection, injection is the result of the ponderomotive force associated with the *slow beat wave* of two intersecting pulses. Beat wave injection was first proposed and analyzed by Esarey et al. [129] in a concept referred to as colliding pulse injection.

Colliding pulse injection [129, 131, 133] uses three short laser pulses: an intense ( $a_0^2 \simeq 1$ ) pump pulse (denoted by subscript 0) for plasma wave generation, a forward going injection pulse (subscript 1), and a backward going injection pulse (subscript 2), as shown in Fig. 14. The frequency, wavenumber, and normalized intensity are denoted by  $\omega_i$ ,  $k_i$ , and  $a_i$  ( $i = 0, 1, 2$ ). Furthermore, it is assumed that  $k_1 \simeq k_0$ ,  $k_2 \simeq -k_0$ , and  $\omega_1 - \omega_2 = \Delta\omega \gg \omega_p$ . The pump pulse generates a plasma wave with phase velocity near the speed of light ( $v_{p0} \simeq c$ ). The forward injection pulse travels at a fixed distance behind the pump pulse, which determines the position (i.e., phase) of the injected electrons. The injection pulses are orthogonally polarized to the pump laser pulse, such that the pump pulse and backward going injection pulse do not beat. When the injection pulses collide some distance behind the pump, they generate a slow ponderomotive beat wave of the form  $a_1 a_2 \cos(\Delta k z - \Delta\omega t)$  (here  $\Delta k = k_1 - k_2 \simeq 2k_0$ ) with a phase velocity  $v_{pb} \simeq |\Delta\omega|/2k_0 \ll c$ . The axial force

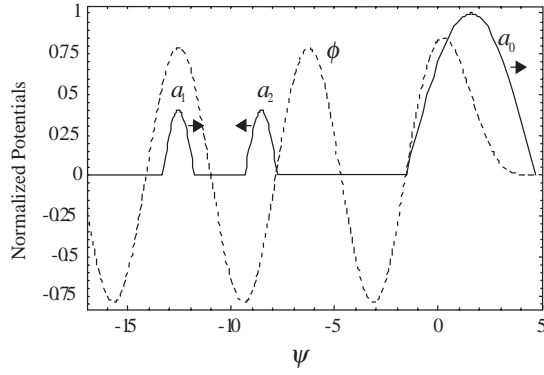


FIG. 14: Profiles of the pump laser pulse  $a_0$ , the wake  $\phi$ , and the forward  $a_1$  injection pulse, all of which are stationary in the  $\psi = k_p(z - v_p t)$  frame, and the backward injection pulse  $a_2$ , which moves to the left at  $\simeq 2c$

associated with this beat wave scales as

$$F_z = -(m_e c^2 / \gamma) (\partial / \partial z) a_1 a_2 \cos(2k_0 z - \Delta \omega t) \quad (48)$$

$$\sim (m_e c^2 / \gamma) 2k_0 a_1 a_2 .$$

During the time in which the two injection pulses overlap, a two-stage acceleration process can occur, i.e., the slow beat wave traps and heats background plasma electrons which, as a result of shifts in their momentum and phase, can be injected into the fast wakefield for acceleration to high energies.

The ratio of the axial force of the beat wave to that of a single pulse in the ponderomotive injection scheme (owing to the gradient in the envelope of the laser intensity) scales as

$$\frac{F_{z,\text{beat}}}{F_{z,\text{env}}} \sim \frac{2k_0 a_1 a_2}{a_p^2 / r_p} , \quad (49)$$

where the subscript  $p$  refers to the single ponderomotive injection pulse and the contribution of the relativistic Lorentz factor  $\gamma$  (which is different for the two cases) is neglected. For comparable injection pulse intensities ( $a_1 \simeq a_2 \simeq a_p$ ), the ratio scales as  $4\pi r_p / \lambda_0 \gg 1$ , i.e., the axial force of the beat wave is much greater than the ponderomotive force from the intensity envelope of a single pulse. Consequently, colliding pulses can result in electron injection at relatively low intensities ( $a_1 \sim a_2 \sim 0.2$ ), as well as at relatively low densities ( $\lambda_p / \lambda \sim 100$ ), thus allowing for high single-stage energy gains. Furthermore, the colliding pulse concept offers detailed control of the injection process: the injection phase can be controlled via the position of the forward injection pulse, the beat phase velocity via  $\Delta\omega$ , the injection energy via the pulse amplitudes, and the injection time (number of trapped electrons) via the backward pulse duration.

To help understand the injection mechanism, it is insightful to consider the electron motion in the wakefield and in the colliding laser fields individually. In the absence of the injection pulses, electron motion in

a 1D wakefield is described by the Hamiltonian  $H_w = \gamma - \beta_p (\gamma^2 - 1)^{1/2} - \phi(\psi)$ , cf. Sect. II F, where  $\phi = \phi_0 \cos \psi$ ,  $v_p = c\beta_p$  is the phase velocity of the plasma wave,  $\gamma_p = (1 - \beta_p^2)^{-1/2}$ , and  $\psi = k_p(z - v_p t)$ . The electron orbits in phase space  $(u_z, \psi)$  are given by  $H_w(u_z, \psi) = H_0$ , where  $H_0$  is a constant,  $\gamma^2 = 1 + u_z^2$ , and  $u_z = \gamma\beta_z$  is the normalized axial momentum, which is given by

$$u_z = \beta_p \gamma_p^2 [H_0 + \phi(\psi)] \pm \gamma_p \left\{ \gamma_p^2 [H_0 + \phi(\psi)]^2 - 1 \right\}^{1/2} . \quad (50)$$

The 1D separatrix (the boundary between trapped and untrapped orbits) is given by  $H_w(\beta_z, \psi) = H_w(\beta_p, \pi)$ , i.e.,  $H_0 = H_{1D} = 1/\gamma_p - \phi(\pi)$ . The maximum and minimum electron momentum on the 1D separatrix occur at  $\psi = 0$  and are (in the limits  $2\phi_0\gamma_p \gg 1$  and  $\gamma_p \gg 1$ )  $u_{w,\text{max}} \simeq 4\gamma_p^2\phi_0$  and  $u_{w,\text{min}} \simeq (4\phi_0)^{-1} - \phi_0$ . The 1D theory neglects the effects of transverse focusing. Associated with a 3D wake is a periodic radial field which is  $\pi/2$  out of phase with the accelerating field, i.e., there exists a phase region of  $\lambda_p/4$  for which the wake is both accelerating and focusing (as opposed to the  $\lambda_p/2$  accelerating region in 1D). If an electron is to remain in this phase region, it must lie within the “3D separatrix” defined by  $H_w(\beta_z, \psi) = H_w(\beta_p, \pi/2)$ , i.e., (50) with  $H_0 = H_{3D} = 1/\gamma_p - \phi(\pi/2)$ . The extremum on the 3D separatrix are given by  $u_{w,\text{max}} \simeq 2\gamma_p^2\phi_0$  and  $u_{w,\text{min}} \simeq (\phi_0^{-1} - \phi_0)/2$ . This value of  $u_{w,\text{max}} \simeq 2\gamma_p^2\phi_0$  gives the usual maximum energy gain due to linear dephasing in a 3D wake.

The background plasma electrons lie on an untrapped orbit (below the separatrix)  $u_{zf}$  given by  $H_w(u_{zf}, \psi) = 1$ , i.e., (50) with  $H_0 = 1$ . At wavebreaking, the bottom of the separatrix  $u_{w,\text{min}}$  coalesces with the plasma fluid orbit,  $u_{zf} = u_{w,\text{min}}$ . This occurs at the well-known wavebreaking field of  $E_{\text{WB}}/E_0 = [2(\gamma_p - 1)]^{1/2}$ .

Consider the motion of electrons in the colliding laser fields in the absence of the wakefield. The beat wave leads to formation of phase space buckets (separatrices) of width  $2\pi/\Delta k \simeq \lambda_0/2$ , which are much shorter than those of the wakefield ( $\lambda_p$ ). In the colliding laser fields, the electron motion is described by the Hamiltonian [129]  $H_b = \gamma - \beta_b [\gamma^2 - \gamma_\perp^2(\psi_b)]^{1/2}$ , where the space charge potential is neglected. Circular polarization is assumed such that  $\gamma_\perp^2 = 1 + a_0^2 + a_1^2 + 2a_0a_1 \cos \psi_b$ , where  $\psi_b = (k_1 - k_2)(z - v_b t)$  and  $v_b = c\beta_b = \Delta\omega/(k_1 - k_2) \simeq \Delta\omega/2k_0$  is the beat phase velocity, assuming  $\omega_p^2/\omega_0^2 \ll 1$ . The beat separatrix is given by  $H_b(\beta_z, \psi_b) = H_b(\beta_b, 0)$  with a maximum and minimum axial momenta of

$$u_{b,m} = \gamma_b \beta_b [1 + (a_0 + a_1)^2]^{1/2} \pm 2\gamma_b (a_0 a_1)^{1/2} . \quad (51)$$

An estimate for the threshold for injection into the wakefield can be obtained by a simple phase-space island overlap criteria. This is done by considering the effects of the wakefield and the beat wave individually, as done above, and by requiring that the beat wave separatrix overlap both the wakefield separatrix and the plasma

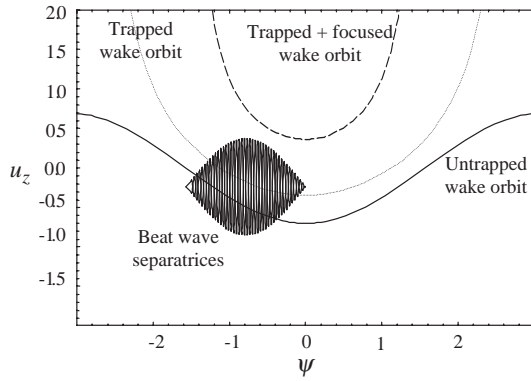


FIG. 15: Longitudinal phase space showing beat wave separatrix, an untrapped plasma wave orbit (*solid line*), a trapped plasma wave orbit (*dotted line*), and a trapped and focused plasma wave orbit (*dashed line*)

fluid oscillation (illustrated in Fig. 15): (i) the maximum momentum of the beat wave separatrix  $u_{b,\max}$  exceed the minimum momentum of the wakefield separatrix  $u_{w,\min}$ , i.e.,  $u_{b,\max} \geq u_{w,\min}$ , and (ii) the minimum momentum of the beat wave separatrix  $u_{b,\min}$  be less than the plasma electron fluid momentum  $u_{zf}$ , i.e.,  $u_{b,\min} \leq u_{zf}$ . Conditions (i) and (ii) imply a beat wave threshold [129, 131]

$$(a_1 a_2)_{\text{th}}^{1/2} = \frac{(1 - H_0)}{4\gamma_b(\beta_p - \beta_b)}, \quad (52)$$

and an optimal wake phase for injection (location of the forward injection pulse)

$$\cos \psi_{\text{opt}} = \phi_0^{-1} [(1 - \beta_b \beta_p) \gamma_b \gamma_{\perp}(0) - (1 + H_0)/2], \quad (53)$$

where  $H_0 = H_{1D} = 1/\gamma_p + \phi_0$  for the 1D wake separatrix and  $H_0 = H_{3D} = 1/\gamma_p$  for the 3D wake separatrix (trapped and focused). In the limits  $\gamma_p^2 \gg 1$ ,  $\beta_b^2 \ll 1$ , and  $a_i^2 \ll 1$ , (52) and (53) become  $4(a_1 a_2)_{\text{th}}^{1/2} \simeq (1 - H_0)(1 + \beta_b)$  and  $2\phi_0 \cos \psi_{\text{opt}} \simeq 1 - H_0 - 2\beta_b$  with  $H_{1D} \simeq \phi_0$  and  $H_{3D} \simeq 0$ . As an example,  $\phi_0 = 0.7$ ,  $\beta_b = -0.02$ , and  $\gamma_p = 50$  imply a threshold of  $(a_1 a_2)_{\text{th}}^{1/2} \simeq 0.25$  and an optimal injection phase of  $\psi_{\text{opt}} \simeq 0$  for injection onto a trapped and focused orbit.

To further evaluate the colliding laser injection method, the motion of test particles in the combined wake and laser fields was simulated in 3D [131]. In the numerical studies, the laser pulse axial profiles were half-period sine waves (linearly polarized with Gaussian radial profiles) with peak amplitude  $a_i$  and length  $L_i$ . The wakefield is assumed to be nonzero for  $\psi \leq 3\pi/4$  (see Fig. 14) and the test particles are loaded uniformly with  $\psi > 3\pi/4$  (initially at rest).

An example of the injection process is given in Fig. 16, which shows the evolution in longitudinal phase space ( $u_z, \psi$ ) of the test electron distribution (a) before the collision of the injection laser pulses (in the untrapped fluid orbit of the wake) at  $\omega_p t = 36$ , (b) during the collision (crossing the wake separatrix) at  $\omega_p t = 39$ , (c) after

the collision at  $\omega_p t = 50$ , and (d) the resulting energetic electron bunch at  $\omega_p t = 150$ . Also shown in Fig. 16 is the 1D wake separatrix. The parameters are  $a_1 = a_2 = 0.32$ ,  $L_0 = 4L_1 = 4L_2 = \lambda_p = 40 \mu\text{m}$ ,  $\phi_0 = 0.7$ ,  $\lambda_0 = \lambda_2 = 0.8 \mu\text{m}$ ,  $\lambda_1 = 0.83 \mu\text{m}$ , and  $r_0 = r_1 = r_2 = 15 \mu\text{m}$ , with the position of the forward injection pulse centered at  $\psi_{\text{inj}} = -12.6$ . After  $z \simeq 0.7 \text{ mm}$  of propagation following the collision, Fig. 16(d), the bunch length is 1 fs with a mean energy of 38 MeV, a fractional energy spread of 0.2%, and a normalized transverse emittance of 0.9 mm-mrad. The trapping fraction  $f_{\text{trap}}$  is 3%, corresponding to  $2.6 \times 10^6$  bunch electrons. Here,  $f_{\text{trap}}$  is defined as the fraction of electrons trapped that were initially loaded in a region of length  $\lambda_p/4$  with  $r \leq 2 \mu\text{m}$  (simulations indicate that electrons loaded outside this region are not trapped). Note that the bunch number can be increased by increasing the laser spot sizes (i.e., laser powers). For example, when the laser spot sizes are doubled,  $r_i = 30 \mu\text{m}$  in the simulation of Fig. 16 (all other parameters as in Fig. 16), the number of trapped electrons increases to  $1.5 \times 10^7$  and the normalized transverse emittance increases to 3.9 mm-mrad. Estimates indicate that space charge effects can be neglected while the bunch remains inside the plasma [131].

Experiments on laser injection methods are being pursued at several laboratories world-wide. For example, at LBNL, experiments are underway on the colliding pulse method [134]. The initial set of experiments uses only two pulses: a pump pulse for wakefield generation and a single near-backward propagating injection pulse. Here the pump and injection pulses have the same polarization such that injection results from the slow ponderomotive beat wave that is produced when the injection pulse collides with the tail of the pump pulse.

### C. Density Transitions

Bulanov et al. [135] describe how a downward transition in the plasma density with a scale length  $L_{tr}$  long compared to  $\lambda_p$  could be used to induce local wavebreaking of the plasma wave. Consider the position of a phase peak on a plasma wave of the form  $\phi = \phi_0 \cos k_p \zeta$  (where  $-\zeta = ct - z$  is the distance behind the drive beam) located  $N$  periods behind the drive beam. Before the density transition, the phase peak is located at  $|\zeta_1| = N\lambda_{p1}$ , and after the transition, the phase peak is located at  $|\zeta_2| = N\lambda_{p2}$ , where  $\lambda_{p1}$  ( $n_1$ ) and  $\lambda_{p2}$  ( $n_2$ ) are the plasma wavelengths (densities) before and after the transition with  $\lambda_{p1} < \lambda_{p2}$  ( $n_1 > n_2$ ). The density transition changes the location of the phase peak by the relative amount  $\Delta|\zeta_p| = N(\lambda_{p1} - \lambda_{p2})$ . If this transition occurs over a length  $L_{tr}$ , then the change in the phase velocity is  $\Delta v_p/c \simeq N(\lambda_{p1} - \lambda_{p2})/L_{tr}$ . This effect increases proportional to the distance behind the driver (increasing  $N$ ), as well as the magnitude of the density gradient,  $(\lambda_{p1} - \lambda_{p2})/L_{tr} \simeq d\lambda_p/dz = -(\lambda_p/2n)dn/dz$ .

More rigorously, the phase velocity of the wake during

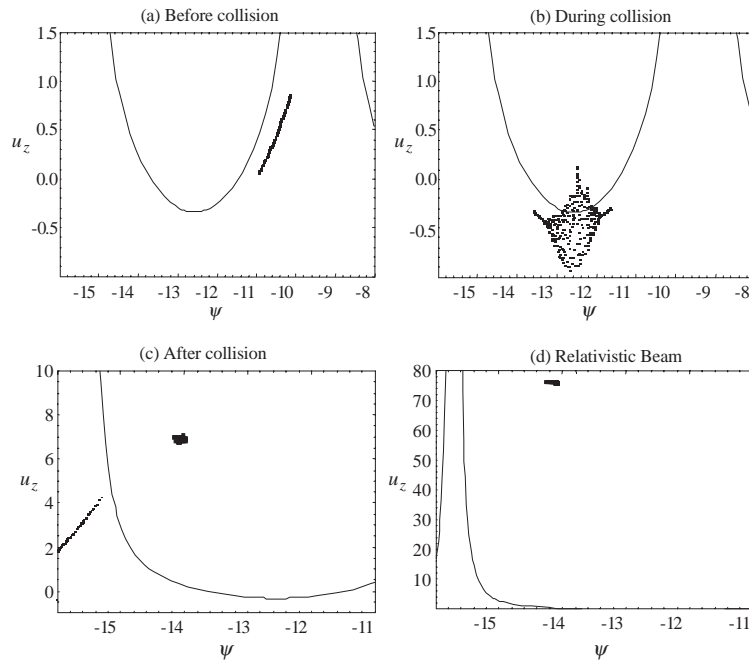


FIG. 16: Electron distribution in longitudinal ( $u_z, \psi$ ) phase space (a) before injection pulse collision ( $\omega_p \Delta t = 0$ ), (b) during collision ( $\omega_p \Delta t = 3$ ), (c) just after collision ( $\omega_p \Delta t = 14$ ), and (d) at  $\omega_p \Delta t = 114$  (38 MeV electron bunch with 1 fs duration, 0.2% energy spread, and 0.9 mm-mrad normalized transverse emittance). The separatrix between trapped and untrapped wake orbits (solid line) is shown

a density transition can be calculated by considering the local phase of the wake, which is given to leading order by  $\psi = k_p(z)(z - ct)$ , where  $v_g \simeq c$  has been assumed since changes to the group velocity due to a slow variation in density are small in an underdense plasma  $\omega_p^2/\omega^2 \ll 1$ . Using the definitions of the effective frequency  $\omega_{p,\text{eff}} = -\partial\psi/\partial t$  and wavenumber  $k_{p,\text{eff}} = \partial\psi/\partial z$  of the plasma wave, the local phase velocity of the wake is given by  $v_p = \omega_{p,\text{eff}}/k_{p,\text{eff}}$ , i.e.,

$$v_p/c = [1 + (\zeta/k_p)dk_p/dz]^{-1}. \quad (54)$$

For a small variation,  $v_p/c - 1 \simeq -(\zeta/k_p)dk_p/dz = -(\zeta/2n)dn/dz$ . Since  $\zeta < 0$  behind the drive pulse, the wake phase velocity will decrease for decreasing density  $dn/dz < 0$ .

Local wave breaking of the wake will occur at the point at which the local phase velocity equals the fluid velocity of the plasma electrons. To leading order, the size of the fluid oscillation depends on the intensity of the drive pulse, the pulse length, and the local plasma density. Since the “resonance” for exciting a large amplitude wake is rather broad,  $L \sim \lambda_p$  (weakly dependent on density), a large wake can be excited on the density ramp with a fluid velocity given approximately by  $v_e/c \simeq E_z/E_0$ , where  $E_z/E_0 \ll 1$  is the normalized electric field amplitude of the wake. According to fluid theory, wavebreaking of a wake will always occur on a density down ramp at a sufficiently large distance behind the drive pulse (assuming the wake is not damped by some other mechanism), since (54) indicates that the wake phase velocity will continue

to decrease as a function of time for a fixed point on the density down ramp. Using (54), wavebreaking ( $v_p = v_e$ ) will occur at a distance behind the drive pulse given by  $\zeta = 2(c/v_e - 1)n/(dn/dz)$ . For example, if  $v_e/c = 1/3$  and  $L_{tr} = n|dn/dz|^{-1} = 3\lambda_p$ , then wavebreaking occurs at  $|\zeta| = 12\lambda_p$ .

Bulanov et al. [135] performed 1D particle-in-cell simulations of a laser pulse with  $a_0 = 2$  and  $L = 12\lambda$  propagating in a plasma with  $\lambda_{p1} = 23.4\lambda$ ,  $\lambda_{p2} = 25\lambda$ , and  $L_{tr} = 24\lambda$ . These simulations found that the plasma wave breaks on the ramp and injects a significant number of electrons into the wake, in apparently the second bucket behind the laser pulse, which are accelerated to high energy but with a large energy spread.

Suk et al. [136] consider the limit of a step function downward plasma density transition ( $n_1 = 5 \times 10^{13} \text{ cm}^{-3}$  and  $n_2 = 3.5 \times 10^{13} \text{ cm}^{-3}$ ) and a wake generated by an electron beam driver of energy 16 MeV, bunch length  $0.16\lambda_{p2}$ , bunch radius  $0.089\lambda_{p2}$ , and peak density  $n_b = 2.4n_1 = 3.4n_2$ . Using 2D particle-in-cell simulations, the trapped electron bunch, after propagating a few plasma wavelengths past the transition, had a total charge near 0.5 nC, a bunch length near  $0.09\lambda_{p2}$ , and electron energies in the range 5–15 MeV.

## V. PULSE PROPAGATION AND GUIDING

To describe laser pulse propagation in a fully-ionized plasma, it is convenient to represent the electric  $\mathbf{E}$  and

magnetic fields  $\mathbf{B}$  by the scalar  $\Phi$  and vector  $\mathbf{A}$  potentials,  $\mathbf{E} = -\nabla\Phi - \partial\mathbf{A}/\partial ct$  and  $\mathbf{B} = \nabla \times \mathbf{A}$ , and to use Coulomb gauge,  $\nabla \cdot \mathbf{A} = 0$ . In terms of the normalized potentials  $\phi = e\Phi/m_e c^2$  and  $\mathbf{a} = e\mathbf{A}/m_e c^2$ , the wave equation and the Poisson equation are given by, respectively,

$$\left(\nabla^2 - \frac{1}{c^2} \frac{\partial^2}{\partial t^2}\right) \mathbf{a} = k_p^2 \frac{n}{n_0} \mathbf{u} + \frac{1}{c} \frac{\partial}{\partial t} \nabla \phi, \quad (55)$$

$$\nabla^2 \phi = k_p^2 (n - n_i) / n_0, \quad (56)$$

where  $\mathbf{u} = \gamma \mathbf{v} / c = \mathbf{p} / m_e c$  is the normalized electron fluid momentum,  $\gamma = (1 - \beta^2)^{-1/2} = (1 + u^2)^{-1/2}$  is the relativistic Lorentz factor,  $n$  is the plasma electron density,  $n_i$  is the initial density profile (prior to the passage of the laser pulse),  $n_0 = n_i(r = 0)$  with  $r = 0$  corresponding to the direction of propagation (the  $z$ -axis), and  $\omega_{p0} = ck_p = (4\pi n_0 e^2 / m_e)^{1/2}$ . Here and in the following, it is assumed that the ions remain stationary, which is typically the case for short pulse lasers ( $\lesssim 1$  ps) propagating in underdense plasma ( $\omega_{p0}^2 / \omega^2 \ll 1$ ). Furthermore, collisions and thermal effects are neglected, since the collision time is typically much greater than the laser pulse length and the thermal velocity is typically much less than the quiver velocity of an electron in the laser field.

The first term on the right-hand side of (55) is the contribution due to the plasma current  $\mathbf{J}$ . In the cold fluid limit,  $\mathbf{J} = -en\mathbf{u}/\gamma$ , where the plasma density  $n$  and momentum  $\mathbf{u}$  satisfy the continuity and momentum equations, which are given by, respectively,

$$\partial n / \partial ct + \nabla \cdot (n\mathbf{u}/\gamma) = 0, \quad (57)$$

$$[\partial / \partial ct + (\mathbf{u}/\gamma) \cdot \nabla] \mathbf{u} = \nabla \phi + \partial \mathbf{a} / \partial ct - (\mathbf{u}/\gamma) \times (\nabla \times \mathbf{a}). \quad (58)$$

It is also convenient to introduce the independent variables  $\zeta = z - ct$  and  $\tau = t$ , where  $\zeta$  is an approximate measure of the distance back from the head of the pulse (which is moving with a group velocity  $v_g \simeq c$ ). Initially, the front of the laser pulse is assumed to be at  $\zeta = 0$  and the pulse body extends into the region  $\zeta \leq 0$  (the plasma is unperturbed in the region  $\zeta > 0$ ). In terms of the  $\zeta, \tau$  coordinates, the wave equation is given by [52]

$$\left(\nabla_{\perp}^2 + \frac{2}{c} \frac{\partial^2}{\partial \zeta \partial \tau} - \frac{1}{c^2} \frac{\partial^2}{\partial \tau^2}\right) \mathbf{a} \simeq k_p^2 \frac{n}{n_0} \mathbf{u}. \quad (59)$$

On the right-hand side of (59), the term  $\nabla \partial \phi / \partial ct$  has been neglected, since the fast part of the electrostatic potential,  $\phi \sim \exp(ik\zeta)$ , is typically small compared to relevant terms contributing to the fast part of the plasma current. Typically, the third term on the left-hand side of (59) can be neglected. As discussed in Sect. II, the leading order transverse motion is the quiver motion. Hence, for a wide variety of phenomena, it is sufficient to approximate  $\mathbf{u} = \mathbf{a}$  on the right-hand side of (59).

The wave equation can be further simplified by the slowly varying envelope approximation. Assuming a linearly polarized laser field with a transverse component of the form  $\mathbf{a}_f = \hat{\mathbf{a}}_s(r, \zeta, \tau) \exp(ik\zeta)/2 + \text{c.c.}$ , the wave equation describing the evolution of the slowly varying amplitude  $\hat{\mathbf{a}}_s$  is given by

$$\left(\nabla_{\perp}^2 + 2i\omega \frac{\partial}{\partial \tau} + \frac{2}{c} \frac{\partial^2}{\partial \zeta \partial \tau}\right) \hat{\mathbf{a}}_s = k_p^2 \rho_s \hat{\mathbf{a}}_s, \quad (60)$$

where  $\rho_s = (n/n_0)/\gamma$ ,  $\mathbf{u}_{\perp f} \simeq \mathbf{a}_f$ ,  $\omega = ck$  is the laser frequency, and the subscripts  $f$  and  $s$  denote the fast and slow components, respectively. The small term  $\partial^2 / \partial \tau^2$  has been neglected in the wave operator, however, the  $\partial^2 / \partial \zeta \partial \tau$  term is retained so as to correctly describe variations in the laser pulse group velocity. The paraxial approximation is the result of neglecting the term  $\partial^2 / \partial \zeta \partial \tau$ . Throughout the following, the subscripts  $s$  and  $f$  will be dropped for convenience.

A useful approximation in the study of short pulse interactions with plasmas is the quasi-static approximation (QSA), which was first applied to nonlinear laser-plasma interactions by Sprangle et al. [60, 61]. In the QSA, the plasma fluid equations are written in terms of the independent variables  $\zeta$  and  $\tau$ , as above. The QSA assumes that in the time it takes the laser pulse to transit a plasma electron, the laser pulse does not significantly evolve. In other words,  $\tau_L \ll \tau_E$ , where  $\tau_L = L/c$  is the laser pulse duration and  $\tau_E$  is the laser pulse evolution time, which is typically one the order of a Rayleigh (diffraction) length. Thus, the plasma electrons experience a static (independent of  $\tau$ ) laser field. In the QSA, the  $\partial / \partial \tau$  derivatives are neglected in the plasma fluid equations which determine the plasma response to the laser pulse. The  $\partial / \partial \tau$  derivatives, however, are retained in the wave equation which describes the evolution of the laser pulse. The QSA allows the laser-plasma interaction to be calculated in an iterative fashion. For a fixed  $\tau$ , the plasma response to the laser field is determined as a function of  $\zeta$  by solving the QSA fluid equations [e.g., (12) in the 1D limit]. Using this fluid response, the wave equation is then solved to update the laser pulse in  $\tau$ .

The fluid quantity  $\rho = n/\gamma n_0$  in (60) can be determined from the quasi-static fluid equations. For example, in the 1D limit, it can be shown [57] that  $\rho \simeq (1 + \phi)^{-1}$ , where  $\phi$  satisfies (12). In 2D and assuming  $v_g \simeq c$ , it can be shown [137] that

$$\rho \simeq (1 + \Psi)^{-1} (\rho_0 + k_p^{-2} \nabla_{\perp}^2 \Psi), \quad (61)$$

where  $\rho_0$  is the initial value of  $\rho$  (prior to the laser pulse) and the quantity  $\Psi = \phi - a_z$  satisfies

$$\frac{\partial^2 \Psi}{\partial \zeta^2} = (k_p^2 \rho - \nabla_{\perp}^2) u_z + \frac{\partial}{\partial \zeta} \nabla_{\perp} \cdot \mathbf{u}_{\perp}, \quad (62)$$

with  $\mathbf{u}_{\perp} = (k_p^2 \rho)^{-1} \partial_{\zeta} (\nabla_{\perp} \Psi)$  and  $u_z = [u_{\perp}^2 + a^2 - \Psi(2 + \Psi)] / [2(1 + \Psi)]$ . The wake potential  $\Psi$  is related to the axial electric field  $E_z$  induced in the plasma by  $k_p \hat{E}_z =$

$-\partial\Psi/\partial\zeta$ , where  $\hat{E}_z = E_z/E_0$  and  $E_0 = m_e c \omega_{p0}/e$  is the cold, nonrelativistic wavebreaking field.

A useful quantity in discussing phenomena such as optical guiding is the index of refraction  $\eta_r$ . The effective index of refraction  $\eta_r$  is defined by setting the right-hand side of (60) equal to  $k^2(1-\eta_r^2)\mathbf{a}$ , which yields  $\eta_r \simeq 1 - k_p^2\rho/2k^2$ .

### A. Optical Guiding in Plasmas

The optical guiding mechanisms discussed below are based on the principle of refractive guiding. Refractive guiding becomes possible when the radial profile of the index of refraction,  $\eta_r(r)$ , exhibits a maximum on-axis, i.e.,  $\partial\eta_r/\partial r < 0$ . Since  $\eta_r \simeq ck_z/\omega$ ,  $\partial\eta_r/\partial r < 0$  implies that the phase velocity along the propagation axis is less than it is off-axis. This causes the laser phase fronts to curve such that the beam focuses towards the axis.

The index of refraction for a small amplitude electromagnetic wave propagating in a plasma of uniform density  $n = n_0$ , in the 1D limit, is given by  $\eta_r = (1 - \omega_p^2/\omega^2)^{1/2}$ . For large amplitude waves, however, variations in the electron density and mass will occur, i.e.,  $\omega_p^2 \rightarrow (\omega_{p0}^2/\gamma)n/n_0$ . Hence, the general expression for the index of refraction for a large amplitude electromagnetic wave in a plasma is given by [36, 60]

$$\eta_r(r) \simeq 1 - \frac{\omega_{p0}^2}{2\omega^2} \frac{n(r)}{n_0\gamma(r)}, \quad (63)$$

assuming  $\omega_{p0}^2/\omega^2 \ll 1$ . The index of refraction profile  $\eta_r(r)$  can be modified by the relativistic factor  $\gamma(r)$  or the radial density profile  $n(r)$ . The leading order motion of the electrons in the laser field is the quiver motion  $\mathbf{p}_\perp = m_e c \mathbf{a}$  and, hence,  $\gamma \simeq \gamma_\perp = (1 + a^2)^{1/2}$ . A laser intensity profile peaked on-axis  $\partial a^2/\partial r < 0$  leads to  $\partial\eta_r/\partial r < 0$  and the possibility of guiding (i.e., relativistic self-focusing). The density profile can have contributions from a preformed density channel  $\Delta n_p \sim \Delta n r^2/r_0^2$  or a plasma wave  $\delta n \sim \delta \hat{n}(r) \cos k_p \zeta$ , where  $n = n_0 + \Delta n_p + \delta n$ . A radial density profile which has a minimum on-axis (i.e., a channel) implies  $\partial\eta_r/\partial r < 0$  and the possibility of guiding. In the limits  $a^2 \ll 1$ ,  $|\Delta n_p/n_0| \ll 1$  and  $|\delta n/n_0| \ll 1$ , the refractive index is [120]

$$\eta_r \simeq 1 - \frac{\omega_{p0}^2}{2\omega^2} \left( 1 - \frac{a^2}{2} + \frac{\Delta n_p}{n_0} + \frac{\delta n}{n_0} \right). \quad (64)$$

In the above expression, the  $a^2/2$  term is responsible for relativistic optical guiding [138–141], the  $\Delta n_p/n_0$  term is responsible for preformed density channel guiding [36, 119, 142–147], and the  $\delta n/n_0$  term is responsible for self-channeling [36, 52, 140, 148], plasma wave guiding [61, 94, 115], and self-modulation of long laser pulses [36–38, 104].

### B. Relativistic Optical Guiding

The self-focusing of laser beams by relativistic effects was first considered by Litvak [138] and Max et al. [139]. In the standard theory of relativistic optical guiding [141], only the effects of the transverse quiver motion of the electrons are included in the expression for  $\eta_r$ , i.e.,  $n = n_0$  and  $\gamma = \gamma_\perp(r)$ , where  $\gamma_\perp^2 = 1 + a^2(r)$  and circular polarization is assumed. Inclusion of the self-consistent density response, however, indicates that relativistic self-focusing is ineffective in preventing the diffraction of short ( $L \lesssim \lambda_p$ ) laser pulses [36, 61].

In the weakly-relativistic limit ( $a^2 \ll 1$ ), the refractive index is given by

$$\eta_r \simeq 1 - (\omega_{p0}^2/2\omega^2)(1 - a^2/2), \quad (65)$$

where the density response has been neglected ( $n = n_0$ ). Refractive guiding requires  $\partial\eta_r/\partial r < 0$ , which is the case for a laser intensity profile peaked on-axis,  $\partial a^2/\partial r < 0$ . The paraxial wave equation with a refractive index given by (65) has the form of a Schrödinger equation with a third order nonlinearity, as is the case in nonlinear optics where  $\eta_r = \eta_0 + \eta_2 I$ . Hence, self-focusing will occur when the laser power  $P$  exceeds a critical power  $P_c$  [141].

An equation for the laser spot size  $r_s(\zeta, z)$  can be derived by applying a method such as the source dependent expansion (SDE) method [149] to the paraxial wave equation [(60) neglecting the term  $\partial^2/\partial\zeta\partial\tau$ ]. In effect, the SDE method assumes that the radial intensity profile is approximately Gaussian,  $|a|^2 = (a_0 r_0/r_s)^2 \exp(-2r^2/r_s^2)$ , and finds a best fit for the spot size  $r_s(\zeta, z)$  locally in space and time. Using the index of refraction given by (65), the laser spot size evolves according to [141]

$$\frac{d^2 R}{dz^2} = \frac{1}{Z_R^2 R^3} \left( 1 - \frac{P}{P_c} \right), \quad (66)$$

where  $R = r_s/r_0$  is the normalized spot size,  $r_0$  is the minimum spot size in vacuum, and  $Z_R = kr_0^2/2$  is the vacuum Rayleigh length. The first term on the right-hand side of (66) represents vacuum diffraction, whereas the second term represents relativistic self-focusing. Here,  $P/P_c = k_p^2 a_0^2 r_0^2/16$  for circular polarization (for linear polarization,  $a_0^2 \rightarrow a_0^2/2$ ). The critical power for relativistic self-focusing is  $P_c = 2c(e/r_e)^2(\omega/\omega_{p0})^2$ , where  $r_e = e^2/m_e c^2$ , or in practical units,

$$P_c(\text{GW}) \simeq 17.4 (\omega/\omega_{p0})^2. \quad (67)$$

The solution to (66) with  $dr_s/dz = 0$  at  $z = 0$  is

$$r_s^2/r_0^2 = 1 + (1 - P/P_c)z^2/Z_R^2, \quad (68)$$

which indicates that the spot size diffracts for  $P < P_c$ , remains guided or “matched” ( $r_s = r_0$ ) for  $P = P_c$ , and focuses for  $P > P_c$ . Equation (66) predicts “catastrophic” focusing for  $P > P_c$ . This results from the approximation

$(1+a^2)^{-1/2} \simeq 1 - a^2/2$  in the  $a^2 \ll 1$  limit. Higher-order nonlinearities will prevent the laser from focusing indefinitely [141].

The above discussion of relativistic guiding neglected the electron density response  $\delta n$  in the expression for the index of refraction. The effectiveness of relativistic guiding can be strongly influenced by the plasma response. In particular, it can be shown that relativistic optical guiding is ineffective in preventing the diffraction of sufficiently short pulses,  $L \lesssim \lambda_p/\gamma_\perp$  [36, 61]. This is because the index of refraction becomes modified by the laser pulse on the plasma frequency time scale, not the laser frequency time scale. Typically, relativistic guiding only effects the body of long pulses,  $L > \lambda_p$ .

In the 1D ( $r_s^2 k_p^2 \gg 1$ ) and weakly-relativistic ( $a^2 \ll 1$ ) limits, nonlinear quasi-static theory [61] indicates that the self-consistent electron density response satisfies  $\delta n/n_0 - a^2/2 \simeq -\delta\phi$ , hence,

$$\eta_r \simeq 1 - (\omega_{p0}^2/2\omega^2)(1 - \delta\phi), \quad (69)$$

where  $\delta\phi$  is the normalized electrostatic potential which satisfies

$$(\partial^2/\partial\zeta^2 + k_p^2) \delta\phi = k_p^2 a^2/2. \quad (70)$$

For long laser pulses with sufficiently smooth envelopes,  $|\partial a^2/\partial\zeta| \ll |k_p a^2|$ ,  $\partial^2\phi/\partial\zeta^2$  can be neglected in (70) (which neglects the generation of plasma waves) and  $\delta\phi \simeq a^2/2$ . Hence, in the long pulse limit  $L \gg \lambda_p$ , the index of refraction has the form given by (64) and the standard theory of relativistic focusing discussed above can be applied to the body of long pulses. Although long pulses can be guided by relativistic effects, they can also be unstable to self-modulation [36–38] and laser-hose instabilities [150, 151], which are discussed in more detail in the Sect. VI B.

The fact that short pulses  $L \lesssim \lambda_p$  diffract even when  $P \gtrsim P_c$  can be most easily shown as follows. For very short pulses  $L < \lambda_p$ , the  $k_p^2$  term can be neglected on the left-hand side of (70). For example, a short pulse with a constant intensity profile ( $a^2 = a_0^2$ ) induces a space charge potential given by  $\phi \simeq k_p^2 a_0^2 \zeta^2/4$ , and the refractive index becomes

$$\eta_r \simeq 1 - (\omega_{p0}^2/2\omega^2)(1 - k_p^2 a_0^2 \zeta^2/4), \quad (71)$$

as opposed to (65). This indicates that the effective critical power for a short pulse [61] is  $P_{c,sp} \simeq 2P_c/(k_p^2 \zeta^2) \gg P_c$ , since  $k_p^2 \zeta^2/2 \ll 1$  for a short pulse. In particular,  $P_{c,sp}$  becomes infinite at the leading edge of the pulse  $\zeta \rightarrow 0$ . Hence, the leading portion  $L < \lambda_p$  of a laser pulse will diffractively erode even when  $P \simeq P_c$ .

Simulations [36], based on a 2D-axisymmetric quasi-static fluid model, confirm the inability of relativistic guiding to prevent the diffraction of short laser pulses. The results are shown in Fig. 17 for the parameters  $\lambda_p = 0.03$  cm ( $n_0 = 1.2 \times 10^{16}$  cm $^{-3}$ ),  $r_0 = \lambda_p$  (Gaussian radial profile),  $\lambda = 1$   $\mu$ m ( $Z_R = 28$  cm), and  $P = P_c$ . The initial axial laser profile is given by  $|\hat{a}_i(\zeta)| = a_0 \sin(-\pi\zeta/L)$

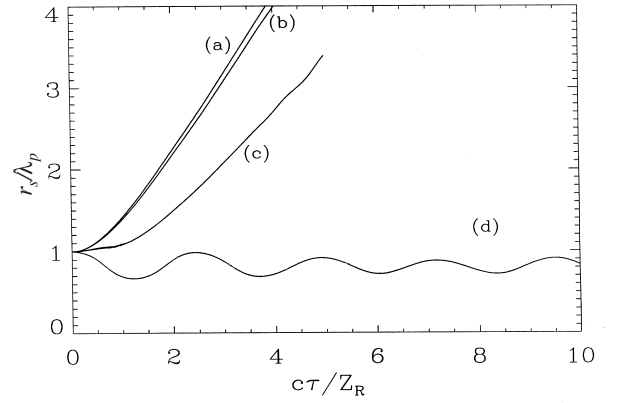


FIG. 17: Laser spot size  $r_s$  versus normalized propagation distance  $c\tau/Z_R$  for (a) vacuum diffraction, (b)  $L = \lambda_p/4$ , and (c)  $L = \lambda_p$ , with parameters  $P = P_c$ ,  $a_0 = 0.9$ , and  $\lambda_p = 0.03$  cm. (d) Guiding of  $L = \lambda_p$  pulse in a preformed parabolic plasma density channel with  $\Delta n = 1/(\pi r_e r_s^2)$

for  $0 < -\zeta < L = c\tau_L$ , where  $a_0 = 0.9$  for the above parameters. Simulations are performed for two laser pulse lengths,  $L = \lambda_p$  ( $\tau_L = 1$  ps) and  $L = \lambda_p/4$  ( $\tau_L = 0.25$  ps). The spot size at the pulse center versus normalized propagation distance  $c\tau/Z_R$  is shown in Fig. 17 for (a) the vacuum diffraction case, (b) the  $L = \lambda_p/4$  pulse, and (c) the  $L = \lambda_p$  pulse. The  $L = \lambda_p/4$  pulse diffracts almost as if in vacuum. The  $L = \lambda_p$  pulse experiences a small amount of initial guiding before diffracting. A preformed parabolic plasma density channel, however, is effective in guiding the  $L = \lambda_p$  pulse, as shown in Fig. 17(d), where the channel depth is given by  $\Delta n = 1/\pi r_e r_0^2 = 1.3 \times 10^{15}$  cm $^{-3}$  and the density on-axis is  $n_0 = 1.2 \times 10^{16}$  cm $^{-3}$ .

### C. Preformed Plasma Density Channels

The concept of using a plasma density channel to guide a laser beam dates back to early studies of laser fusion [142, 143]. Density channels in plasmas have been created by a number of methods. An intense laser pulse propagating in a plasma can create a channel through a combination of ponderomotive and thermal effects. The creation of a density channel through the hydrodynamic expansion of the radial plasma profile was observed in the early 1970's in long-pulse (150 ns) CO $_2$  laser experiments [143]. The length of such a channel, however, is limited to the propagation distance of the laser pulse which creates the channel, and the utility of using such a channel to guide a laser pulse many Rayleigh lengths is limited. For high power, short laser pulses, the propagation length and, hence, the channel length can be increased by relativistic self-guiding, as has been observed in pump-probe experiments [152]. Alternatively, a long focal region can be created with an axicon or cylindrical lens, and this method has been used successfully to create extended plasma channels in which laser pulses have been guided

for many Rayleigh lengths [144–147]. Non-laser-based methods for creating plasma channels include capillary discharges [153–157], in which laser guiding over many Rayleigh lengths has been achieved [153, 154, 156, 157]. Other methods for plasma channel guiding have been explored, such as laser-ablation of a capillary [158].

A preformed plasma density channel can guide short, intense laser pulses [36, 119, 142–147, 155, 156]. Consider a parabolic density channel of the form  $n = n_0 + \Delta n r^2 / r_0^2$ , where  $\Delta n = n(r_0) - n(0)$  is the channel depth. For a low power  $P \ll P_c$ , low intensity  $a^2 \ll 1$  laser pulse, the index of refraction is given approximately by

$$n_r = 1 - \frac{\omega_{p0}^2}{2\omega^2} \left( 1 + \frac{\Delta n r^2}{n_0 r_0^2} \right). \quad (72)$$

Analysis of the paraxial wave equation with an index of refraction of this form indicates that the spot size  $r_s$  of a Gaussian laser beam with  $a^2 = (a_0 r_0 / r_s)^2 \exp(-2r^2 / r_s^2)$  evolves according to [104]

$$\frac{d^2 R}{dz^2} = \frac{1}{Z_R^2 R^3} \left( 1 - \frac{\Delta n}{\Delta n_c} R^4 \right). \quad (73)$$

The first term on the right-hand side represents the effects of vacuum diffraction and the second term represents the focusing effects of the channel. This indicates that a Gaussian beam will be guided at the matched beam spot size  $r_s = r_0$  provided that the channel depth  $\Delta n$  is equal to the critical channel depth given by [36, 119]

$$\Delta n_c = (\pi r_e r_0^2)^{-1}, \quad (74)$$

or  $\Delta n_c (\text{cm}^{-3}) = 1.13 \times 10^{20} / r_0^2 (\mu\text{m})$ , where  $r_e = e^2 / (m_e c^2)$  is the classical electron radius.

The general solution to (73) for the initial ( $z = 0$ ) conditions  $dr_s/dz = 0$  and  $r_s = r_i$  is [104]

$$2 \frac{r_s^2}{r_i^2} = 1 + \frac{\Delta n_c r_0^4}{\Delta n r_i^4} + \left( 1 - \frac{\Delta n_c r_0^4}{\Delta n r_i^4} \right) \cos(k_{\text{os}} z), \quad (75)$$

where  $k_{\text{os}} = (2/Z_R)(\Delta n / \Delta n_c)^{1/2}$  and  $r_i$  is the injected spot size. A matched beam requires  $\Delta n r_i^4 = \Delta n_c r_0^4$ , e.g.,  $r_i = r_0$  and  $\Delta n = \Delta n_c$ . If the beam is not matched within the channel, the spot size oscillates between  $r_s^2 = r_i^2$  and  $r_s^2 = \Delta n_c r_0^4 / \Delta n r_i^2$  with an average value  $\langle r_s^2 \rangle = (r_i^2 / 2)(1 + \Delta n_c r_0^4 / \Delta n r_i^4)$ . The oscillation period within the channel is  $\lambda_{\text{os}} = 2\pi / k_{\text{os}} = \pi Z_R (\Delta n_c / \Delta n)^{1/2}$ . The laser beam will remain confined within the channel provided that the maximum radius of the channel  $r_{\text{ch}}$  is sufficiently large, i.e.,  $r_{\text{ch}} > r_s$ .

To illustrate the effectiveness of optical guiding using preformed density channels, the results of three simulations are presented, all based on the 2D-axisymmetric fluid model discussed in Sect. V. The first simulation [52] is of a channel-guided LWFA with an ultrashort ( $L \simeq \lambda_p$ ), high-intensity ( $a_0 \sim 1$ ) laser pulse, the results of which are shown in Figs. 18, 19, and 20. In this example, the initial axial laser profile is given by

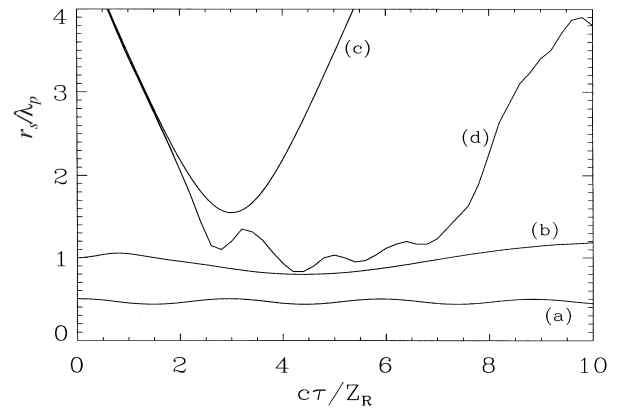


FIG. 18: Laser spot size  $r_s$  versus propagation distance  $c\tau$  for (a) a channel-guided LWFA, (b) a tailored-pulse LWFA, (c) vacuum diffraction, and (d) the self-modulated LWFA shown in Figs. 11–13

$|\hat{a}(\zeta)| = a_0 \sin(-\pi\zeta/L)$  for  $0 < -\zeta < L$ , with  $a_0 = 0.72$  and  $L = 120 \mu\text{m}$  (400 fs). Also,  $\lambda = 1 \mu\text{m}$  and  $r_0 = 60 \mu\text{m}$  (Gaussian radial profile), which implies  $Z_R = 1.1 \text{ cm}$  and  $P = 40 \text{ TW}$ . The density on-axis is chosen such that  $L = \lambda_p$  ( $n_0 = 7.8 \times 10^{16} \text{ cm}^{-3}$ ) and a parabolic profile is assumed with  $\Delta n = (\pi r_e r_0^2)^{-1} = 3.2 \times 10^{16} \text{ cm}^{-3}$ .

Figure 18(a) shows the evolution of the laser spot size versus normalized propagation distance  $c\tau/Z_R$ . The laser pulse remains guided by the density channel, the laser spot size exhibiting small oscillations about its initial value over the full  $20Z_R = 23 \text{ cm}$  simulation length. After  $c\tau = 20Z_R$ , the pulse profile shows very little distortion from its initial profile. A surface plot of the electron density profile at  $c\tau = 20Z_R$  is shown in Fig. 19. The initial, unperturbed parabolic profile can be seen at  $\zeta = 0$ , and the distortion of the channel by the laser pulse, including the excitation of a large amplitude wakefield along the axis, is evident in the region  $\zeta < 0$ . In this example nearly all the electrons have been expelled from the vicinity of the laser pulse. The radial variation in the channel density causes a radial variation in the plasma wavelength and curvature of the plasma wavefronts. A slight axial damping of the plasma wave also occurs, as evident in Fig. 20, where the axial electric field  $E_z$  is plotted versus  $\zeta$  along the axis at  $c\tau = 20Z_R$ . The effects of the wakefields on a continuous 2 MeV electron beam with an initial normalized transverse emittance  $\varepsilon_n = 1.0 \text{ mm-mrad}$  and RMS radius  $r_b = 10 \mu\text{m}$  was also simulated. After  $c\tau = 20 \text{ cm}$ , approximately 70% of the beam electrons were trapped and accelerated. The peak electron energy increases nearly linearly with propagation distance with an average acceleration gradient of  $5.25 \text{ GeV/m}$  (1 GeV in 20 cm).

The second simulation [120] is of a channel-guided LWFA in the self-modulated regime with  $L > \lambda_p$ , the results of which are shown in Figs. 21–24. Here, the initial laser parameters are  $\tau_L = 100 \text{ fs}$  ( $L = 30 \mu\text{m} = 2.5\lambda_p$ ),  $P = 0.3 \text{ TW}$  (30 mJ),  $\lambda = 1 \mu\text{m}$ ,  $r_0 = 10 \mu\text{m}$  ( $Z_R =$

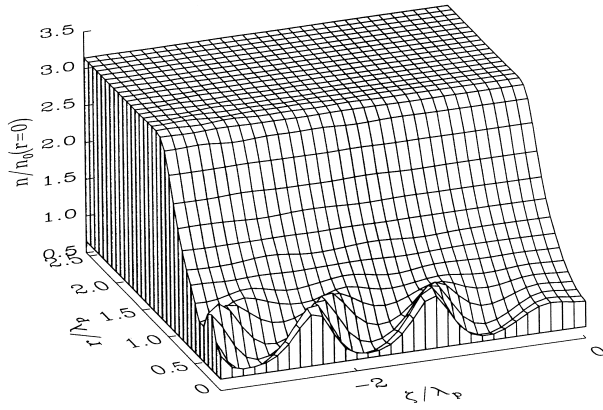


FIG. 19: Plasma electron density  $n/n_0$  at  $c\tau = 20Z_R$  for a channel-guided LWFA. Initial density profile is parabolic with a depth  $\Delta n = \Delta n_c = 1/(\pi r_e r_0^2)$

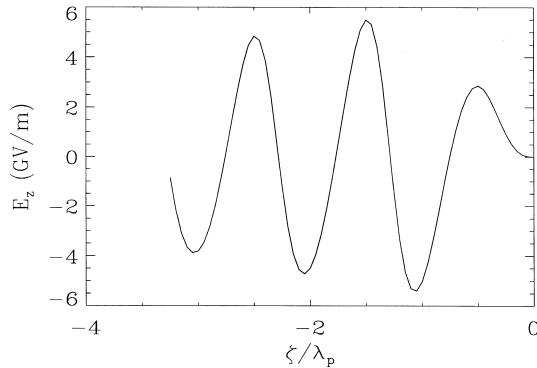


FIG. 20: Axial electric field  $E_z$  on axis at  $c\tau = 20Z_R$  for the channel-guided LWFA shown in Fig. 19

0.3 mm), and  $I_0 = 2 \times 10^{17}$  W/cm<sup>2</sup> ( $a_0 = 0.38$ ); the channel parameters are  $n_0 = 8 \times 10^{18}$  cm<sup>-3</sup> ( $\lambda_p = 12$   $\mu$ m),  $\Delta n_p(r_{\text{ch}}) = 2n_0$ , and  $r_{\text{ch}} = 40$   $\mu$ m. Also, the on-axis density is slightly tapered such that it rises to  $2n_0$  over a length of 1 cm. The pulse remains guided after  $c\tau = 0.75$  cm ( $24Z_R$ ) of propagation, but a large modulation (in  $\zeta$  with period  $\sim \lambda_p$ ) in intensity (Fig. 21) and power (Fig. 22) has developed through self-modulation and forward Raman instabilities (discussed in Sect. VI). The density profile at  $c\tau = 0.75$  (Fig. 23), along with the corresponding on-axis electric field (Fig. 24), clearly shows a well-defined wakefield of amplitude  $E_z = 50$  GV/m.

The third simulation [159] is an example of mismatched laser propagation in a channel, which extends from  $0.5$  cm  $< z < 1.5$  cm with  $n_0 = 5 \times 10^{18}$  cm<sup>-3</sup>,  $\Delta n_p(r_{\text{ch}}) = 4n_0/5$ , and  $r_{\text{ch}} = 150$   $\mu$ m (parameters near those of the experiment in [159]). Here, a  $\lambda = 0.8$   $\mu$ m, 100 fs, 30 GW (3 mJ), 1.6 times-diffraction-limited laser pulse is focused on the channel entrance with spot size  $r_s = 15$   $\mu$ m. Owing to the low laser power, the pulse does not become self-modulated. Figure 25 shows that the laser spot size oscillates about its matched value of  $r_0 = 28$   $\mu$ m, emerging from the 1 cm long channel with

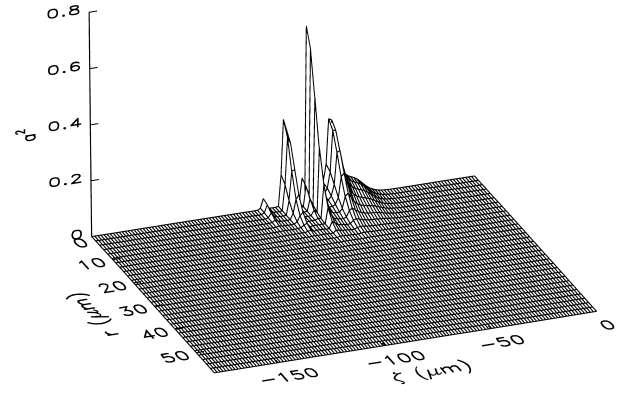


FIG. 21: Normalized laser intensity  $|a|^2$  after propagating  $c\tau = 24Z_R$  for a channel-guided self-modulated LWFA

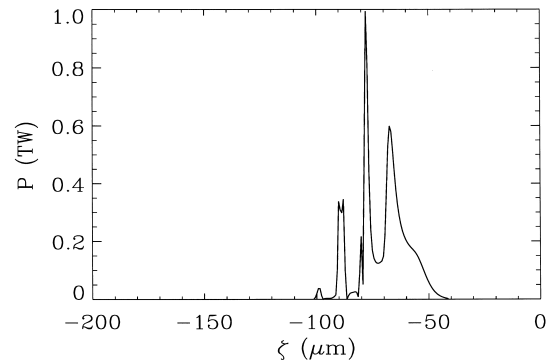


FIG. 22: Laser power versus  $\zeta$  at  $c\tau = 24Z_R$  for a channel-guided self-modulated LWFA

a radius of 45  $\mu$ m and a divergence angle of 14 mrad, in approximate agreement with the experiment of [159].

The above discussion concerned parabolic channel profiles. Other channel profiles, however, may offer different advantages. Durfee et al. [145] discuss the formation of “leaky” channels, in which the channel is approximately parabolic out to some radius, after which the density falls off to zero. Such a profile occurs naturally in the creation of plasma channels by hydrodynamic expansion of a hot plasma core in a gas. Higher order transverse modes may not be guided by such a channel, and Antonsen and Mora [160] have described how leaky channels can stabilize certain instabilities, such as small angle forward Raman scattering [105, 106], self-modulation [36, 38, 104], and laser-hosing [150, 151]. Hollow channels (e.g., a square channel with density zero on-axis out to the channel radius) may have beneficial properties with regard to particle acceleration [161, 162]. Within the hollow channel, where the plasma density is essentially zero, the transverse profile of the axial wakefield is uniform, thus providing uniform acceleration of an injected beam. The wakefield in such a channel, however, may be damped through resonant absorption in the channel walls [163].

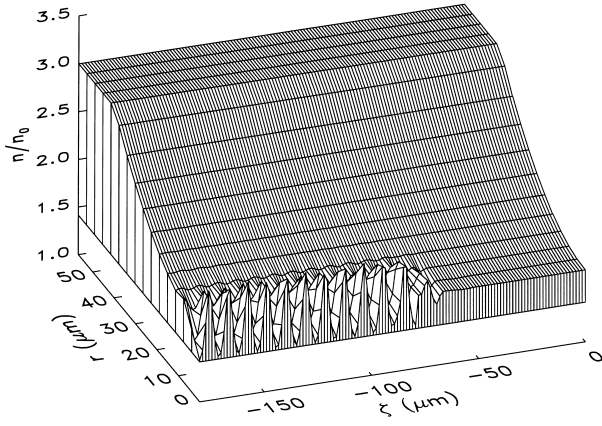


FIG. 23: Electron plasma density  $n/n_0$  at  $c\tau = 24Z_R$  for a channel-guided self-modulated LWFA

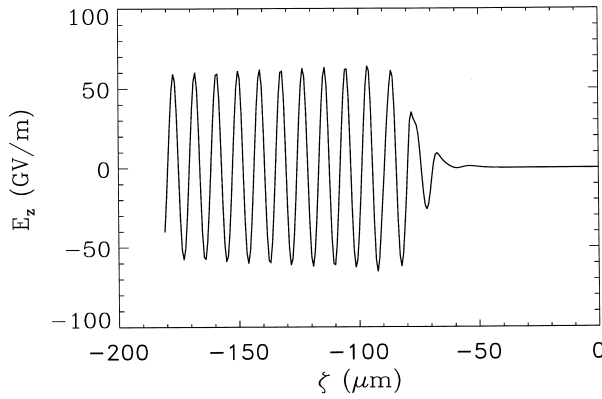


FIG. 24: Axial electric field  $E_z$  of the plasma wave at  $c\tau = 24Z_R$  for a channel-guided self-modulated LWFA

#### D. Ponderomotive Self-Channelling

The radial ponderomotive force of a long laser pulse ( $L > \lambda_p$ ) propagating in an initially uniform plasma can expel electrons from the axis thus creating a density channel (i.e., self-channelling or electron cavitation) [36, 52, 119, 140, 148]. This can enhance the effects of relativistic self-focusing. Consider a long ( $L \gg \lambda_p$ ) axially uniform laser pulse propagating in an initially uniform plasma. The steady-state radial force balance indicates that the space charge force is equal to the ponderomotive force, i.e.,  $\nabla_{\perp} \phi = \nabla_{\perp} \gamma_{\perp}$ , where  $\gamma_{\perp} = (1 + a^2)^{1/2}$  (with circular polarization). This implies a density perturbation via the Poisson equation  $\nabla_{\perp}^2 \phi = k_p^2 \delta n/n_0$  given by [36, 140, 148]

$$\delta n/n_0 = k_p^{-2} \nabla_{\perp}^2 (1 + a^2)^{1/2}, \quad (76)$$

assuming  $|\delta n/n_0| \leq 1$ . The corresponding index of refraction is given by

$$\eta_r \simeq 1 - \frac{\omega_{p0}^2}{2\omega^2} \left[ \frac{1 + k_p^{-2} \nabla_{\perp}^2 (1 + a^2)^{1/2}}{(1 + a^2)^{1/2}} \right]. \quad (77)$$

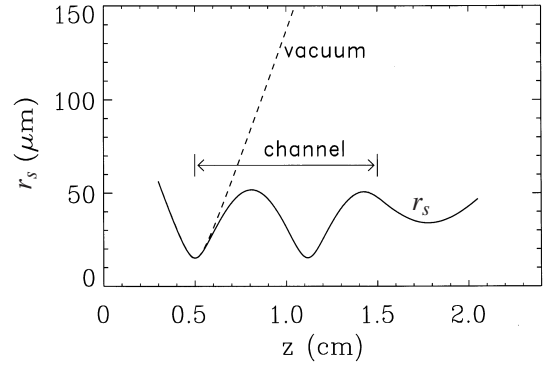


FIG. 25: Laser spot size versus propagation distance  $z = c\tau$  in vacuum (dashed curve) and in a plasma channel (solid curve) located at  $0.5 \text{ cm} < z < 1.5 \text{ cm}$  for a low-power  $P \ll P_c$  mismatched pulse

This can also be derived from 2D nonlinear plasma theory via (61). In the long pulse limit  $L \gg \lambda_p$ ,  $|\partial \Psi / \partial \zeta| \ll |k_p \Psi|$  and  $(1 + \Psi) \simeq (1 + a^2)^{1/2}$ , which yields (77). Neglected in (77) is the generation of plasma waves, which can lead to the self-modulation of long pulses.

In the limit  $a^2 \ll 1$ , a Gaussian laser profile  $a^2 = a_0^2 \exp(-2r^2/r_0^2)$  creates a density profile  $\delta n = -\delta n(0)(1 - 2r^2/r_0^2) \exp(-2r^2/r_0^2)$ . Along the axis, the depth of the ponderomotive channel is given by  $\delta n(0) = a_0^2 \Delta n_c$ , where  $\Delta n_c$  is given by (74). Analysis of the paraxial wave equation with a density perturbation given by  $\delta n/n_0 = k_p^{-2} \nabla_{\perp}^2 a^2/2$  indicates that the normalized spot size of a Gaussian laser pulse evolves according to [164]

$$\frac{d^2 R}{dz^2} = \frac{1}{Z_R^2 R^3} \left( 1 - \frac{P}{P_c} - \frac{\delta n(0)}{2\Delta n_c} R^{-2} \right). \quad (78)$$

where  $\delta n(0) = a_0^2 \Delta n_c$  and  $a^2 \ll 1$  is assumed. Hence, in the limit  $P/P_c \ll 1$ , the ponderomotive channel depth required to guide a laser pulse is  $\delta n(0) \geq 2\Delta n_c$ . Clearly, when  $a_0 < 1$ , the ponderomotive self-channel alone will not guide the laser pulse. Furthermore,  $|\delta n/n_0| < 1$  implies  $a_0^2 < 2(P/P_c)^{1/2}$  and  $\delta n(0) < 2(P/P_c)^{1/2} \Delta n_c$ . Hence,  $P/P_c \leq 1$  implies  $\delta n(0) < 2\Delta n_c$ , which again indicates that the ponderomotive channel alone will not guide the laser pulse. For laser powers approaching the critical power  $P \rightarrow P_c$ , guiding is achieved predominantly by relativistic self-focusing. Ponderomotive self-channelling can enhance this effect, but does not dramatically alter the power threshold for guiding. More detailed studies [140], which include the effects of relativistic self-focusing and ponderomotive self-channelling, conclude that the threshold power for guiding is  $P(\text{GW}) \geq 16.2(\omega^2/\omega_{p0}^2)$ .

#### E. Plasma Wave Guiding

An ultrashort ( $L < \lambda_p$ ) laser pulse can be guided by a plasma wave, provided that the laser pulse is properly phased within the wakefield and the wakefield amplitude

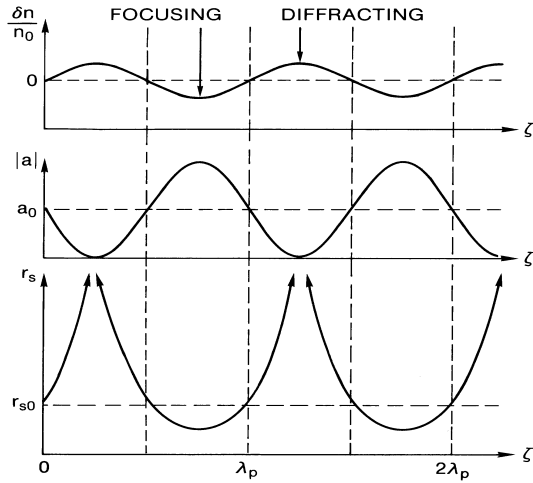


FIG. 26: Schematic of focusing effects of an externally generated plasma wave on an initially uniform low-intensity laser pulse

is sufficiently large [61, 94, 115]. The effective index of refraction for a low power ( $P/P_c \ll 1$ ), low intensity ( $a^2 \ll 1$ ) laser pulse propagating in a plasma wave is given by

$$\eta_r \simeq 1 - (\omega_{p0}^2/2\omega^2)(1 + \delta n/n_0), \quad (79)$$

where  $\delta n$  is the density oscillation of the plasma wave, which is assumed to be unaffected by the low intensity laser pulse. Consider a plasma wave of the form  $\delta n = \delta \hat{n}(r) \sin(k_p \zeta)$ , where  $\delta \hat{n} > 0$  and  $d\delta \hat{n}/dr < 0$ . In regions where  $\sin(k_p \zeta) < 0$ , the plasma wave acts as a local density channel and enhances focusing, and in regions where  $\sin(k_p \zeta) > 0$ , the plasma wave enhances diffraction. Notice that a test laser pulse experiences maximum focusing at the minimum of  $\delta n$  (i.e.,  $\zeta = -\pi/2$ ). As discussed in Sect. IIH, it can be shown that a short laser pulse can be frequency upshifted by a plasma wave wakefield provided that it resides in the phase region where  $\partial \delta n / \partial \zeta < 0$ . In particular, maximum frequency upshifting occurs at the maximum of  $-\partial \delta n / \partial \zeta$  (i.e.,  $\zeta = -\pi$  for the above example). In general, for a sinusoidal plasma wave, a test laser pulse will experience both enhanced focusing and frequency upshifting over a  $|k_p \Delta \zeta| = \pi/4$  phase region of the plasma wave. Furthermore, (79) describes how a plasma wave can lead to the modulation of a long ( $L > \lambda_p$ ) laser pulse [94], as illustrated schematically in Fig. 26.

In addition to a plasma wave acting as a local density channel and providing periodic regions of enhanced focusing and diffraction as described above, a plasma wave can enhance the self-focusing of long ( $L \gg \lambda_p$ ) laser pulses by several other methods. For example, the electric field profile  $E_{pw}$  of the plasma wave can provide an additional radial ponderomotive force via  $\nabla E_{pw}^2$  [165]. In addition, the oscillatory motion of the plasma electrons in the plasma wave can contribute to the relativistic Lorentz factor [5]. Furthermore, the plasma

wave can lead to the generation of higher-order Stokes and anti-Stokes light waves (i.e., energy cascading) which can affect self-focusing [92]. These effects have been observed in experiments [165] and simulations [5, 92] of two-frequency laser-plasma interactions, in which the plasma wave is resonantly driven by the laser beat wave.

## VI. LASER-PLASMA INSTABILITIES

Laser plasma instabilities can limit the laser propagation distance and degrade the performance of a laser-driven accelerator. This section will provide a brief overview of a few instabilities that are relevant to short-pulse laser-driven accelerators: stimulated forward and backward Raman scattering [51, 166–168], self-modulation [36–38, 104, 106], and laser-hose instabilities [150, 151]. In particular, this section will consider instabilities relevant to laser pulses short compared to the ion response time. Other instabilities present in long-pulse laser-plasma interactions, such as parametric coupling to ion modes, which have been observed in PBWA experiments [96], will not be discussed.

### A. Stimulated Raman Scattering

Stimulated Raman scattering involves the interaction of a light wave with an electron plasma wave [51]. In its most basic form, it consists of the decay of the pump laser field, of frequency and wavenumber  $(\omega_0, \mathbf{k}_0)$ , into an electron plasma wave  $(\omega, \mathbf{k})$  and two daughter light waves, namely a Stokes wave  $(\omega_0 - \omega, \mathbf{k}_0 - \mathbf{k})$  and an anti-Stokes wave  $(\omega_0 + \omega, \mathbf{k}_0 + \mathbf{k})$ . Typically,  $\omega \simeq \omega_p + i\Gamma$  where the growth rate  $\Gamma$  is obtained through a standard linear instability analysis. In such an analysis, the pump laser field is assumed to be a 1D plane wave of the form  $a \sim a_0 \exp(i\mathbf{k}_0 \cdot \mathbf{r} - i\omega_0 t)$ . Perturbations are introduced  $\delta a \sim \exp[i(\mathbf{k}_0 \pm \mathbf{k}) \cdot \mathbf{r} - i(\omega_0 \pm \omega)t]$  and the linearized equations are then solved to determine the behavior of the instability. Since the pump laser is assumed to be a 1D plane wave, the 3D evolution of the pump laser is not taken into consideration. In particular, the effects of diffraction and self-focusing are neglected. Strictly speaking, the resulting analysis is only valid for times short compared to the characteristic evolution time  $\tau_E$  of the pump laser, e.g.,  $t < \tau_E \sim Z_R/c$ . In practice, however, the growth rates obtained from such an analysis can be adequate estimates provided that the mode frequency and growth rate are large compared to  $\tau_E^{-1}$ .

For an infinite, 1D plane wave pump field, the purely temporal Raman growth rates, i.e.,  $\delta a \sim \exp(\Gamma t)$  with growth rate  $\Gamma$  independent of  $t$ , can be obtained in a straightforward manner. The basic treatment of forward and backward Raman scattering is presented in the monograph by Kruer [51]. Temporal growth rates for the various Raman modes in various regimes has been summarized by Antonsen and Mora [106]. For short laser

pulses, however, the growth and propagation of the instability with respect to the laser pulse front must be correctly taken into consideration. Antonsen and Mora [37, 106] first applied convective instability analysis, or a spatiotemporal analysis, to Raman instabilities in order to account for the short-pulse character of the instability.

### 1. Backward Raman scattering

In Raman backscattering (RBS), the pump wave  $(\omega_0, k_0)$  decays into a plasma wave  $(\omega, k)$  and a backward going scattered wave  $(\omega_0 - \omega, k_0 - k)$ , where  $\omega \simeq \omega_p$  and  $k \simeq 2k_0$ . The standard temporal growth rate [51], in the limits  $a_0^2 \ll 1$  and  $\omega_p \ll \omega_0$ , i.e., the weakly-coupled regime, is  $\Gamma = (a_0/2)(\omega_p\omega_0)^{1/2}$ . In general, the scattered mode can propagate at some angle  $\theta$  with respect to the pump wave, i.e., sidescatter, and the growth rate is given by  $\sin(\theta/2)$  times the RBS result. The spatiotemporal analysis indicates that the number of e-folds  $N_e$  of the instability,  $\delta a \sim \exp(N_e)$ , is given by [106]

$$N_e \simeq (a_0^2 k_p k_0 / 8)^{1/2} |\zeta|. \quad (80)$$

In effect, since the scattered wave is moving opposite to the pump, the temporal growth is modified by  $ct \rightarrow |\zeta|/2$ , where  $\zeta = z - ct$  is a measure of the distance back from the front of the laser pulse.

Typically, RBS is the fastest growing of the Raman scattering instabilities. In laser-plasma accelerators, RBS is significant for a number of reasons. At low pump laser intensities, the spectrum of the backscattered radiation can be used to determine  $\omega - \omega_p$ , and hence the plasma density can be determined experimentally. For high pump intensities, however, it has been observed that the backscattered spectrum broadens [169, 170] and, in some cases, becomes extremely broad, such that the  $\omega - \omega_p$  peak can no longer be distinguished. Raman sidescatter and backscatter can erode the back of a long pulse,  $L > \lambda_p$ , since energy is being transported out of the pulse. This has been observed in fluid [106, 108] and particle simulations [72, 171].

As the RBS mode grows to large amplitude, it can trap the background plasma electrons, thus heating the plasma and creating a fast tail on the electron distribution. The phase velocity of the RBS plasma wave is  $v_p = \omega/k = \omega_p/2k_0 \ll c$ . Since  $v_p/c \ll 1$ , the plasma wave can trap the background thermal electrons. The resulting fast electrons can be subsequently trapped by Raman scattered modes propagating at smaller angles  $\theta$ , which will accelerate the electrons to higher energies [39, 124, 126]. Eventually, these background electrons can be trapped and accelerated to very high energies by the plasma wave associated with the forward Raman instability or the self-modulation instability, which has  $v_p \simeq c$ . This mechanism may explain how background plasma electrons can be trapped and accelerated to high energies, as is observed in experiments [12, 40, 42, 44, 45, 102, 114, 172] and simulations

[72, 171] in the self-modulated or forward Raman scattering regimes. Direct wavebreaking of a relativistic plasma wave can also result in the acceleration of background plasma electrons [41].

For high pump intensities, theory predicts that stimulated backscattering occurs in the strongly coupled or Compton regime [106, 173], for which  $\omega \sim \Gamma \gg \omega_p$  and the number of e-folds is  $N_e = (\sqrt{3}/2)(\omega_p^2 \omega_0 a_0^2 / 4)^{1/3} |\zeta| / \gamma_\perp$ . In addition, 1D nonlinear theory predicts that for a linearly polarized pump laser field, stimulated backscattered harmonic radiation can be generated [166] at frequencies given approximately by  $(2\ell + 1)\omega_0$  ( $\ell = \text{integer}$ ), i.e., odd harmonics. Although the growth rate for the higher harmonics can be significant when  $a_0^2 \gg 1$ , thermal effects, i.e., trapping of the background plasma electrons, can severely limit the generation of higher harmonics [166].

### 2. Forward Raman scattering

In Raman forward scattering (RFS) [51], the scattered waves propagate parallel (or nearly parallel) to the pump wave, and the associated plasma wave has a phase velocity  $v_p \simeq c$ . Hence, the plasma wave can be used to accelerate electrons to high energies. The RFS instability can serve as the basis for a LWFA [1, 39, 105, 120], in which a single long ( $L > \lambda_p$ ) laser pulse becomes modulated via RFS and drives a large amplitude plasma wave. A LWFA based on RFS can be viewed as the 1D analogue to the self-modulated LWFA.

The physical mechanism of RFS can be understood by the following 1D description [174]. Consider a long uniform laser pulse propagating in the presence of an initially small amplitude plasma wave of the form  $\delta n = \delta n_0 \sin k_p \zeta$  with  $\delta n_0 > 0$ . Since the local group velocity  $v_g$  is given by  $v_g/c \simeq 1 - \omega_p^2(\zeta)/2\omega_0^2$ , the local group velocity decreases in regions where  $\delta n > 0$  and increases in regions where  $\delta n < 0$ . This tends to modulate the laser pulse such that the intensity modulations are  $\pi/2$  out of phase with the density wave, i.e.,  $a \simeq a_0 + \delta a$ , where  $\delta a = \delta a_0 \cos k_p \zeta$  and  $\delta a_0 > 0$ . This intensity modulation feeds back via  $(\partial^2/\partial \zeta^2 + k_p^2)\delta n/n_0 = (\partial^2/\partial \zeta^2)a^2/2$  and drives the plasma wave to larger amplitudes, resulting in the RFS instability.

Several regimes of the RFS can be identified [106, 167, 173, 175], such as a 4-wave regime, in which both  $\omega_0 \pm \omega_p$  modes are resonant, and a 3-wave regime, in which only  $\omega_0 - \omega_p$  is resonant with the pump laser and the plasma wave. The temporal growth rate in the 4-wave resonant regime is  $\Gamma_4 = \omega_p^2 a_0 / 2\sqrt{2}\omega_0$ , the temporal growth rate in the 4-wave nonresonant regime is  $\Gamma_{4nr} = \sqrt{3}\omega_p (a_0 \omega_p^2 / 4\omega_0^2)^{2/3} / 2$ , and the temporal growth rate in the 3-wave regime is  $\Gamma_3 = \omega_p a_0 (\omega_p / \omega_0)^{1/2} / 4$ . The spatiotemporal analysis [106, 173, 175] indicates, however, that as the RFS instability grows, it passes through these various regimes, depending on the relative value of

$|\zeta|/c\tau$ , where  $\zeta = z - ct$  and  $\tau = t$  are the independent coordinates. The number of e-foldings for these three RFS modes and the corresponding spatiotemporal regimes are roughly given by [106, 173, 175]

$$N_e \simeq 2\Gamma_4(|\zeta|\tau/c)^{1/2}, \quad \text{for } a_0^2 \frac{|\zeta|}{c\tau} \gg 2 \frac{\omega_p^2}{\omega_0^2}, \quad (81)$$

$$N_e \simeq \frac{3}{2}\Gamma_{4nr}(2|\zeta|\tau^2/c)^{1/3}, \quad \text{for } 8 \frac{\omega_p^5}{\omega_0^5} \ll \frac{a_0^2 |\zeta|}{2 c\tau} \ll \frac{\omega_p^2}{\omega_0^2}, \quad (82)$$

$$N_e \simeq 2\Gamma_3(|\zeta|\tau/c)^{1/2}, \quad \text{for } a_0^2 \frac{|\zeta|}{c\tau} \ll 16 \frac{\omega_p^5}{\omega_0^5}, \quad (83)$$

where  $a_0^2 \ll 1$  and  $\omega_p^2/\omega_0^2 \ll 1$  are assumed. Decker et al. [175] describe that for a fixed  $\zeta$  within the pulse, the RFS instability transitions through the various regimes as a function of time. A similar analysis has been applied by Antonsen and Mora [106] to describe small angle RFS, the resulting growth rate is proportional to  $\Gamma_3$ , similar to (83). As a side note, the paraxial approximation to the wave operator ( $\nabla_{\perp}^2 + 2ik_0\partial/\partial c\tau$ ) is not sufficient to describe direct ( $\theta = 0$ ) RFS; retention of the term  $2\partial^2/\partial\zeta\partial c\tau$  is necessary to describe on-axis RFS. This was done in the fluid simulation of the self-modulated LWFA presented in Sect. III D, i.e., the effects of both the RFS and self-modulation instabilities are included. A nonparaxial theory [176], describing the nonlinear coupling of RFS and self-modulation instabilities, has found that the self-modulation instability often dominates in regimes of interest to the self-modulated LWFA.

In addition, it is also possible for a RFS mode to undergo multiple scattering, sometimes referred to as cascading [39, 92], resulting in multiple waves with frequencies  $\omega_0 \pm \ell\omega_p$  ( $\ell = \text{integer}$ ). It is possible to interpret this as photon acceleration, or phase-modulation by the plasma wave, of the scattered light wave [105]. Numerous high-order Stokes and anti-Stokes lines have been observed in simulations of RFS [71]. Multiple [40, 42, 43] (up to the fifth [41]) anti-Stokes lines have been observed in RFS or self-modulated LWFA experiments.

## B. Self-Modulation and Laser-Hose Instabilities

A formalism has been developed [104, 150, 176] to describe the 3D evolution of laser pulses in plasmas, including the effects of diffraction, relativistic and channel guiding, finite pulse duration, and coupling to the self-consistent plasma wave generated by the pulse structure. This formalism has been used to describe a class of “whole-beam” instabilities, which includes self-modulation [104, 150] and laser-hose [150] instabilities. In this formalism, equations are derived to describe the evolution of the local laser pulse spot size  $x_s(\zeta, t)$  and the local laser pulse centroid  $x_c(\zeta, t)$ , where the transverse profile of the laser field is assumed to be a Gaussian of the form  $a \sim \exp[-(x - x_c)^2/x_s^2]$  (the  $y$  profile can be similarly defined). The self-modulation instability consists of

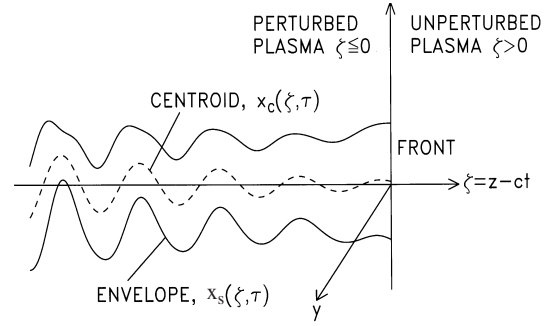


FIG. 27: Schematic of the hose-modulation instability showing the laser pulse centroid  $x_c$  and spot size  $x_s$ .

a periodic “sausaging” of the laser spot size  $x_s$  and the laser-hose consists of a periodic “kinking” of the laser centroid  $x_c$ , as show schematically in Fig. 27. In their most basic forms, the self-modulation and laser-hose instabilities are described by spot size and centroid perturbations of the forms  $\delta x_{s,c} \sim \exp(\Gamma_{s,c}t + ik_p\zeta)$ , i.e., having a period equal to the plasma wavelength  $\lambda_p = 2\pi/k_p$  and a spatiotemporal growth rate  $\Gamma_{s,c} = \Gamma_{s,c}(\zeta, t)$ . Intrinsically, these instabilities involve a coupling to a plasma wave, and the dynamics of the instabilities are determined by the enhanced diffraction and focusing of the laser pulse owing to the presence of the plasma wave.

The physical mechanism underlying self-modulation has been described previously in Sect. III D. The physical mechanism for laser hosing [150, 151] is somewhat similar. Consider a long,  $L > \lambda_p$ , guided laser pulse  $P/P_c = 1 - \Delta n/\Delta n_c$ , with a centroid which is initially perturbed at the plasma wavelength  $x_c \simeq x_{c0} \sin(k_p\zeta)$ . This periodic centroid displacement will drive an asymmetric plasma wave. Notice that for  $x_c^2/x_s^2 \ll 1$ , the intensity profile is approximately  $a^2 \simeq a_0^2(1 + 4xx_c/x_s^2) \exp(-2x^2/x_s^2)$ . At a fixed  $x$  position above the axis,  $x = x_0$ , the laser intensity modulation has the form  $a^2(x_0)/a_0^2 \sim 1 + 4(x_0x_{c0}/x_s^2) \sin(k_p\zeta)$ , which drives a plasma wave. At a fixed  $x$  position below the axis,  $x = -x_0$ , the laser intensity is similarly modulated, but  $\pi$  out of phase with respect to the  $x = x_0$  modulation. Hence, the plasma wave driven below the axis is  $\pi$  out of phase with respect to the plasma wave driven above the axis, i.e., an asymmetric (with respect to  $x$ ) plasma wave. Roughly speaking, the plasma wave has the form  $\delta n \sim -(x/x_s) \cos(k_p\zeta)$ . The laser pulse will tend to focus into the regions of reduced plasma density. For the asymmetric plasma wave, the laser pulse evolves in such a way as to enhance the initial centroid perturbation and the process proceeds in an unstable manner.

Equations describing the behavior of the spot size  $x_s(\zeta, \tau)$  and centroid  $x_c(\zeta, \tau)$  can be derived by analyzing the paraxial wave equation including the effects of a perturbed parabolic density channel and the self-consistent

plasma response given by

$$\frac{\delta n}{n_0} = \int_0^\zeta d\zeta' \cos[k_p(\zeta - \zeta')] \frac{\partial}{\partial \zeta'} \frac{a^2(\zeta')}{2}. \quad (84)$$

In the limits  $a^2 \ll 1$  and  $k_p^2 r_0^2 \gg 1$ ,  $x_s$  and  $x_c$  obey equations of the form [150]

$$\left( \frac{\partial^2}{\partial \hat{\tau}^2} + \frac{\Delta n}{\Delta n_c} \right) \hat{x}_c = -4k_p \int_0^\zeta d\zeta' \sin[k_p(\zeta' - \zeta)] [x_c(\zeta') - x_c(\zeta)] F_c(\zeta', \zeta) \frac{P(\zeta')}{P_c}, \quad (85)$$

and

$$\frac{\partial^2 \hat{x}_s}{\partial \hat{\tau}^2} - \left( 1 - \frac{\hat{x}_s P}{\hat{y}_s P_c} - \frac{\Delta n}{\Delta n_c} \hat{x}_s^4 \right) \hat{x}_s^{-3} = 4\hat{x}_s \int_0^\zeta d\zeta' \cos[k_p(\zeta' - \zeta)] \frac{\partial}{\partial \zeta'} \left[ F_s(\zeta', \zeta) \frac{P(\zeta')}{P_c} \right]. \quad (86)$$

Also,  $\hat{y}_c$  and  $\hat{y}_s$  obey equations similar to (85) and (86), respectively. In the above,  $\hat{x}_c = x_c/r_0$ ,  $\hat{y}_c = y_c/r_0$ ,  $\hat{x}_s = x_s/r_0$ ,  $\hat{y}_s = y_s/r_0$ ,  $\hat{\tau} = c\tau/Z_R$ ,  $Z_R = kr_0^2/2$  is the Rayleigh length,  $\Delta n_c = (\pi r_e r_0^2)^{-1}$  is the critical channel depth,  $P(\zeta)/P_c = a^2 x_s y_s k_p^2 / 16$  is the laser power normalized to the critical power, and  $F_{s,c}(\zeta', \zeta)$  are functions which depend on  $x_s$ ,  $y_s$ ,  $x_c$ , and  $y_c$  and couple the spot size dynamics to the centroid dynamics [150].

The right-hand side of (85) indicates that if  $x_c(\zeta) = x_c(\zeta')$  initially (i.e., a uniform centroid),  $x_c(\zeta)$  will not increase. Hence, the laser-hose instability requires a non-uniform head-to-tail centroid displacement [150]  $\partial x_c / \partial \zeta \neq 0$ . The right-hand side of (86) indicates that axial gradients in the laser power  $\partial P / \partial \zeta \neq 0$  will lead to modulations in the laser envelopes ( $x_s, y_s$ ), which can grow in an unstable manner as discussed in Sect. III D. Both the self-modulation and laser-hose instabilities can occur in either a uniform plasma ( $\Delta n = 0$ ) or in a pre-formed density channel.

In the absence of a centroid perturbation, i.e.,  $x_c = 0$  (no hosing), self-modulation is described by (86). For an axisymmetric pulse ( $x_s = y_s = r_s$ ),  $F_{s,c} = [R^2(\zeta) + R^2(\zeta')]^{-2}$  with  $R = r_s/r_0$  [104]. The second, third, and fourth terms on the left-hand side of (86) represent the effects of vacuum diffraction, relativistic focusing, and channel focusing, respectively, whereas the term on the right-hand side represents the nonlinear coupling of the laser envelope to the plasma wave. Equation (86) describes well-known laser pulse evolution, such as the inability of relativistic guiding to prevent the diffraction of short pulses  $L < \lambda_p$  [36, 60, 61, 115].

The evolution of a long, axially uniform laser beam can be examined in the limit where the effect of the plasma wave is neglected, i.e., the nonlinear coupling term on the right-hand side of (86) is set equal to zero. Neglecting the coupling term, the solution to (86) for the initial ( $z = 0$ )

conditions  $dr_s/dz = 0$  and  $r_s = r_i$  is [104]

$$\frac{r_s^2}{r_i^2} = \frac{\Delta n_c r_0^4}{2\Delta n r_i^4} \left[ 1 - \frac{P}{P_c} + \frac{\Delta n r_i^4}{\Delta n_c r_0^4} - \left( 1 - \frac{P}{P_c} - \frac{\Delta n r_i^4}{\Delta n_c r_0^4} \right) \cos(k_{os} z) \right], \quad (87)$$

where  $k_{os} = (2/Z_R)(\Delta n/\Delta n_c)^{1/2}$  and  $r_i$  is the injected spot size. For  $P \leq P_c$ , the spot size oscillates between  $r_s^2 = r_i^2$  and  $r_s^2 = (1 - P/P_c)\Delta n_c r_0^4 / (\Delta n r_i^2)$  with an oscillation period  $\lambda_{os} = 2\pi/k_{os} = \pi Z_R (\Delta n_c / \Delta n)^{1/2}$ . A matched beam with  $r_s = r_i = r_0$  requires  $P = P_M$ , where [104]

$$P_M = P_c (1 - \Delta n / \Delta n_c), \quad (88)$$

i.e., the effective critical power  $P_M$  for guiding is reduced by a finite density channel (assuming  $\Delta n \leq \Delta n_c$ ). Notice that for  $r_i = r_0$  and  $(k_{os} z)^2 \ll 1$ , (87) reduces to  $r_s^2 / r_0^2 = 1 + (1 - P/P_c - \Delta n / \Delta n_c)(z/Z_R)^2$ . This indicates that beam will initially focus for  $P > P_M$  or diffract for  $P < P_M$  with an effective Rayleigh length of  $Z_R(1 - P/P_c - \Delta n / \Delta n_c)^{-1/2}$ .

The effect of the plasma wave on the spot size evolution is described by the right-hand side of (86). The initial effect of the plasma wave can be estimated by approximating  $R(\zeta') = R(\zeta)$  within the integral in (86), i.e., initially the spot size is uniform throughout the pulse. In this limit the right-hand side of (86) can be written as  $(-\delta n / \Delta n_c) / (2R^3)$ , where  $\delta n$  is the initial density perturbation given by (84). The rise associated with the front of the pulse gives a nonzero value of  $\partial a^2 / \partial \zeta$  that generates a finite amplitude density wake. Throughout the body of a long, flat-top pulse, this density wake has the form  $\delta n = \delta \hat{n} \cos(k_p \zeta)$ . In particular, for a flat-top pulse with a fast rise,  $k_p^2 L_{\text{rise}}^2 \ll 1$ , (84) yields  $\delta n / n_0 = -(a_0^2 / 2) \cos(k_p \zeta)$  and the right-hand side of (86) can be written as  $(-\delta n / 2\Delta n_c) R^{-3} = R^{-3} (P/P_c) \cos(k_p \zeta)$ . Hence, at the phase regions where  $\cos(k_p \zeta) = -1$ , focusing requires  $P \geq P_M / 2$  (for  $k_p^2 L_{\text{rise}}^2 \gg 1$ , the initial wake  $\delta n$  vanishes and focusing requires  $P \geq P_M$ ). Clearly, the effect of the initial density wake  $\delta n(\zeta)$  is to produce

$\zeta$ -periodic regions of enhanced focusing and diffraction. This causes the laser intensity to become modulated at  $\lambda_p$ , which subsequently enhances the density wake at later times. This is the basis of the self-modulation instability.

For sufficiently small perturbations,  $x_s/r_0 \ll 1$  and  $x_c/r_0 \ll 1$ , (85) and (86) decouple and self-modulation and the laser-hose instability can be analyzed independently. The growth of the instabilities for a long ( $L \gg \lambda_p$ ), optically-guided ( $P = P_M$ ) laser pulse can be analyzed by perturbing (86) about the matched-beam equilibrium. Asymptotic growth rates can be obtained in various regimes using standard methods. The number of e-folds  $N_e = \Gamma_{c,s}\tau$  in the various regimes are given by [104, 150]:

Long pulse regime:  $k_p|\zeta|Z_R/z \gg 4\alpha_1 P_c/P$

$$N_e = \frac{3\sqrt{3}}{4} \left( \alpha_2 \frac{P}{P_c} k_p |\zeta| \frac{z^2}{Z_R^2} \right)^{1/3}, \quad (89)$$

Intermediate regime:  $(\alpha_3/4)(P/P_c) \ll k_p|\zeta|Z_R/z \ll 4\alpha_1 P_c/P$

$$N_e = \left( \alpha_3 \frac{P}{P_c} k_p |\zeta| \frac{z}{Z_R} \right)^{1/2}, \quad (90)$$

Short pulse regime:  $k_p|\zeta|Z_R/z \ll (\alpha_3/4)(P/P_c)$

$$N_e = \frac{3\sqrt{3}}{4} \left( \alpha_3 \frac{P}{P_c} k_p^2 |\zeta|^2 \frac{z}{Z_R} \right)^{1/3}. \quad (91)$$

For the laser-hose instability,  $\alpha_1 = \alpha_2 = \alpha_3 = 1$ . For self-modulation,  $\alpha_1 = \sqrt{2}(2 - P/P_c)^{3/2}$  ( $\sqrt{2} \leq \alpha_1 \leq 4$ ),  $\alpha_2 = 2$ , and  $\alpha_3 = \sqrt{2}(2 - P/P_c)^{-1/2}$  ( $1 \leq \alpha_3 \leq \sqrt{2}$ ). Hence, the number of e-folds is a function of the dimensionless parameters  $P/P_c$ ,  $k_p|\zeta|$ , and  $z/Z_R$ .

Some insight can be gained by comparing  $N_e$  for self-modulation in the long-pulse regime to that of RFS in the 4-wave nonresonant regime (discussed in Sect. VI A). Equations (82) and (89) indicate the self-modulation is dominant provided  $k_p^2 r_0^2 \ll k_0^2/k_p^2$ . This supports the assertion that self-modulation dominates in the 2D limit, whereas RFS dominates in the 1D limit, roughly speaking, when  $k_p r_0 \gg k_0/k_p$ . These two growth rates, however, occur in different spatiotemporal regimes, hence, comparison of the growth of self-modulation and RFS is more complicated [176].

To illustrate the behavior of the coupled self-modulation and laser-hose instabilities, (85) and (86) are solved numerically [150]. Consider an initially uniform plasma with a 16 TW, 1 ps laser pulse with wavelength  $\lambda = 1 \mu\text{m}$  and initial spot size  $r_0 = 60 \mu\text{m}$  ( $Z_R = 1.1 \text{ cm}$ ) in a plasma of density  $n_0 = 1.2 \times 10^{18} \text{ cm}^{-3}$  ( $\lambda_p = 30 \mu\text{m}$ ). For these parameters,  $P(\zeta) = P_c$  at the center of the pulse. Initially,  $\hat{x}_s = \hat{y}_s = 1$  and the centroid has a 1% random perturbation such that  $|\partial \ln x_c / \partial \zeta| \ll 1/\lambda_0$ .

As the laser propagates, the high intensity center of the pulse remains guided ( $\hat{x}_s \simeq 1$ ). However, the front

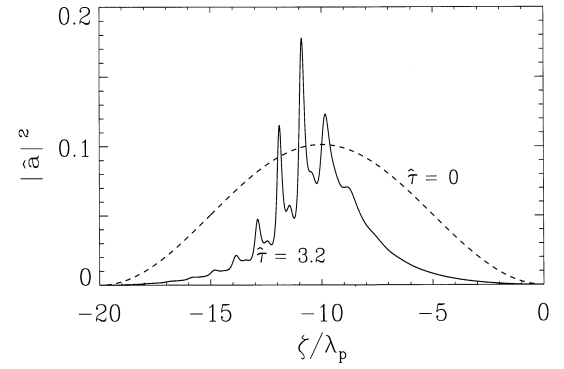


FIG. 28: Normalized laser intensity  $|a|^2$  versus  $\zeta/\lambda_p$  at  $\tau\tau = 0$  (dashed curve) and  $\tau\tau = 3.2Z_R$  (solid curve) for the parameters  $\lambda_p = r_0/2 = 30 \mu\text{m}$ . Laser is moving to the right

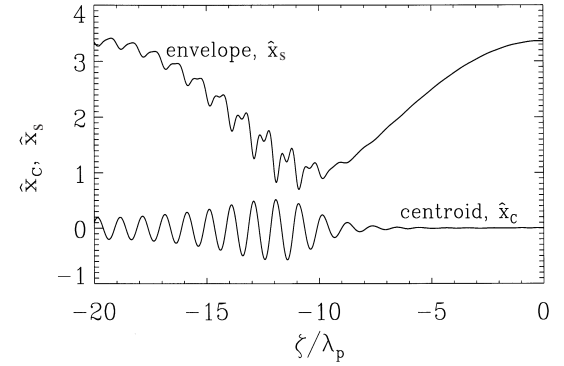


FIG. 29: Laser envelope  $x_s$  (upper curve) and centroid  $x_c$  (lower curve) versus  $\zeta/\lambda_p$  at  $\tau\tau = 3.2Z_R$  for an initial perturbation of 1% in  $x_c$ . Perturbations grow at  $\lambda_p = r_0/2 = 30 \mu\text{m}$

and back portions of the pulse, with  $P < P_c$ , diffract, and the coupled hose and modulation instabilities grow within the guided portion of the pulse as illustrated in Figs. 28 and 29. Figure 28 shows the normalized laser intensity on-axis  $|\hat{a}|^2 = 16P(\zeta)/(P_c \hat{x}_s \hat{y}_s k_p^2 r_0^2)$  at  $\hat{\tau} = 0$  and at  $\hat{\tau} = 3.2$ . Figure 29 plots  $\hat{x}_s(\zeta)$  and  $\hat{x}_c(\zeta)$  at  $\hat{\tau} = 3.2$  and shows a significant level of hosing, with  $|\hat{x}_c|$  as large as 0.5. In addition to the modulation of the envelope at  $\lambda_p$ , the second harmonic at  $\lambda_p/2$  is present, indicating the coupling between the hose and self-modulation instabilities. The spatial modulation of the laser envelope at  $\lambda_p/2$  is due to the dependence of the driving terms on the centroid motion. The second harmonic is not observed when the initial centroid perturbation is sufficiently small, 0.1% for the present parameters.

The presence of the laser-hose instability can strongly modify the structure of the wakefield generated by the laser pulse. To illustrate this point, consider the case when the initial centroid perturbation is 10% [150]. Here, the centroid motion dominates both the development of the wakefield and the evolution of the envelope. The spot size modulations are dominated by the second harmonic component. Figure 30 shows the transverse pro-

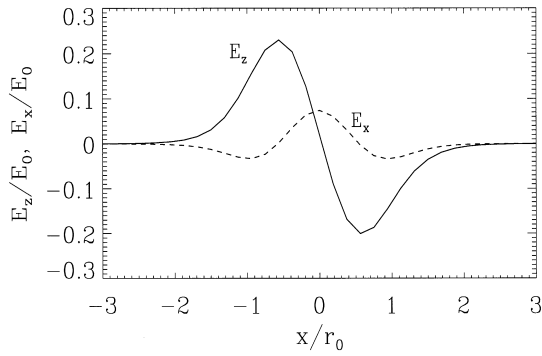


FIG. 30: Transverse profiles of the axial wakefield  $E_z/E_0$  (solid curve) and the transverse wakefield  $E_x/E_0$  (dashed curve) at  $c\tau = 1.8Z_R$  and  $\zeta = -18\lambda_p$  for a hose-dominated case

files of both the longitudinal and transverse wakefields, at  $\hat{\tau} = 1.8$ , near the back of the pulse. The transverse field  $E_x$  is nearly symmetric and peaked on-axis while the longitudinal field  $E_z$  is nearly antisymmetric and vanishes on-axis. This wakefield symmetry is opposite to that which occurs without hosing, i.e., in the absence of the hose instability,  $E_x$  is antisymmetric and vanishes on-axis, while  $E_z$  is symmetric and peaked on-axis.

Although the modulation instability can enhance the wakefield amplitude and acceleration in the LWFA, the laser-hose instability should generally be avoided. To avoid significant levels of hosing, the initial laser centroid must be sufficiently smooth. Equations (89)–(91) indicate that the growth of the hose instability can be reduced by decreasing the pulse length ( $k_p|\zeta|$ ), the laser power ( $P/P_c$ ), or the interaction distance ( $c\tau/Z_R$ ). Further simulations [150] indicate that by appropriately varying (i.e., detuning) either the plasma density and/or the depth of the preformed plasma channel as a function of  $\zeta$  in the laboratory frame, the laser-hose and self-modulation instability can be substantially reduced.

## VII. SUMMARY AND PROSPECTS

Perhaps the three most fundamental physics issues concerning plasma-based accelerators are (i) can an ultrahigh accelerating field be generated, (ii) can this accelerating field be sustained over a sufficiently long propagation distance so as to provide a substantial single-stage electron energy gain, and (iii) can an ultrashort electron bunch be injected and accelerated while maintaining high bunch quality? Theory and simulation indicate that these requirements can be met. Experimental progress is proceeding at a rapid pace, and the generation of ultrahigh accelerating fields, the production of relativistic electrons, and the optical guiding of laser pulse over many diffraction (Rayleigh) lengths have been demonstrated. Much of the experimental success can be attributed to the development of chirped-pulse amplification [8–10],

which has revolutionized laser technology by providing compact sources of multi-TW, sub-ps laser pulses. Nevertheless, numerous accelerator applications will benefit from high-average power sources of intense laser pulses, which requires further technological advances.

The problem of generating a large amplitude plasma wave by an intense laser pulse, for the most part, is well-understood. Theoretically, wakefield generation can be examined by assuming a non-evolving drive laser pulse and by calculating the plasma response to the ponderomotive force. This ponderomotive force can be associated with the envelope of a single laser pulse (e.g., standard LWFA), a laser pulse train, envelope variations on an unstable laser pulse (e.g., self-modulated LWFA), or the beat wave produced by two co-propagating laser pulses of different frequencies (e.g., PBWA). Wakefield generation is optimized when the laser envelope spatial gradients are on the order of the plasma wavelength  $\lambda_p$ . Analytical solutions or simple numerical models exist in the 3D linear regime ( $a_0^2 \ll 1$ ) and in the 1D nonlinear ( $a^2 \gtrsim 1$ ) regime. In the 2D and 3D nonlinear regime, wakefield generation can be examined with a variety of quasi-static fluid and particle-in-cell codes. Unresolved theoretical issues pertaining to wakefield generation include the detailed study of wavebreaking, especially in 2D and 3D, wakefield decay in nonuniform plasmas, thermal effects, and self-trapping.

The problem of sustaining a large accelerating field over a sufficiently long distance requires that a suitable plasma be generated over this distance and that the laser pulse intensity be sustained as it propagates through this plasma. Generating suitable long plasmas requires further technological advancements, such as the development of elongated gas jets, gas jet arrays, or capillaries. Detailed control of the plasma density profile is also required, and tailoring of the plasma density may be achieved using laser ionization or heating methods.

Laser pulse propagation in fully-ionized, underdense ( $\lambda/\lambda_p \ll 1$ ) plasma is affected by a variety of phenomena, including relativistic self-focusing, ponderomotive self-channeling, plasma wave generation, preformed density channels, and instabilities, as discussed in Secs. V and VI. Relativistic self-guiding, which occurs when  $P \geq P_c \simeq 17\lambda_p^2/\lambda^2$  GW, only affects the body of a long ( $L > \lambda_p$ ) laser pulse. The leading portion of the pulse ( $\lesssim \lambda_p$ ), however, will diffractively erode due to the self-consistent response of the plasma density to the laser field. The self-focusing of a long pulse can be enhanced by the ponderomotive blowout of the plasma electrons from the axis, i.e., electron cavitation. In addition, the body of long, relativistically-guided pulse is subject to instabilities (Raman scattering, self-modulation, and laser hosing). In the self-modulated LWFA regime, these instabilities play a dramatic effect, and are responsible for the axial modulation of the pulse profile at  $\lambda_p$ , wakefield excitation, as well as electron self-trapping and acceleration. Preformed plasma density channels are effective in the guiding of short ( $L < \lambda_p$ ) laser pulses when  $\Delta n \geq$

TABLE I: Parameters and results for laser-driven plasma-based accelerator experiments. The laser power  $P$ (TW), laser intensity  $I_0$ (W/cm<sup>2</sup>), laser pulse duration  $\tau_L$ (ps), laser wavelength  $\lambda$ ( $\mu$ m), plasma density  $n_0$ (cm<sup>-3</sup>), energy gain of the accelerated particles  $\Delta W$ (MeV), and accelerating gradient  $E_z$ (GV/m) are listed for each experiment

	$P$ (TW)	$I_0$ (W/cm <sup>2</sup> )	$\tau_L$ (ps)	$\lambda$ ( $\mu$ m)	$n_0$ (cm <sup>3</sup> )	$\Delta W$ (MeV)	$E_z$ (GV/m)
PBWA:							
ILE (Japan) [28]	0.3	$10^{13}$	1000	9.6, 10.6	$10^{17}$	10	1.5
UCLA (USA) [29]	0.2, 0.05	$10^{14}$	300	10.3, 10.6	$10^{16}$	28	2.8
CRL (Canada) [30]	0.1	$10^{14}$	500	10.3, 10.6	$10^{16}$	17	1.7
LULI (France) [31]	0.1, 0.02	$10^{17}$	90	1.05, 1.06	$10^{17}$	1.4	0.6
LWFA:							
KEK (Japan) [34]	2	$10^{17}$	0.09	0.8	$10^{17}$	>100	-
LULI (France) [35]	3.5	$4 \times 10^{17}$	0.4	1.05	$2 \times 10^{16}$	1.6	1.5
SM-LWFA:							
LANL (USA) [39]	0.4	$10^{15}$	700	1.6	-	1.4	-
LLNL (USA) [40]	5	$10^{18}$	0.6	1.05	$10^{19}$	2	-
KEK (Japan) [102]	3	$10^{17}$	1.0	1.05	$10^{19}$	17	30
CUOS (USA) [42]	5	$4 \times 10^{18}$	0.4	1.05	$4 \times 10^{19}$	20	-
NRL (USA) [43]	2.5	$10^{19}$	0.4	1.05	$10^{19}$	30	50
RAL (UK) [12]	20	$6 \times 10^{19}$	1	1.05	$10^{19}$	94	240
MPI (Germany) <sup>a</sup> [114]	1.2	$4 \times 10^{18}$	0.2	0.8	$10^{19}$ - $10^{20}$	>12.5	-
LBNL (USA) [44]	10	$10^{19}$	0.05	0.8	$10^{19}$	>25	-
LOA (France) [45]	17	$2 \times 10^{19}$	0.035	0.8	$10^{18}$	70	58
LOL (France) <sup>b</sup> [13]	30	$3 \times 10^{18}$	0.03	0.8	$4 \times 10^{19}$	200	100

<sup>a</sup> Acceleration mechanism attributed to direct laser acceleration.

<sup>b</sup> Acceleration mechanism attributed to forced laser wakefield acceleration.

$\Delta n_c = 1/(\pi r_e r_0^2)$ . For long pulses ( $L > \lambda_p$ ), relativistic effects can reduce this criterion, i.e.,  $\Delta n/\Delta n_c \geq 1 - P/P_c$ . In addition, if the pulse is sufficiently short ( $L \lesssim \lambda_p$ ), the detrimental effects of various instabilities may be reduced, owing to the reduced growth of the mode within the pulse. Analytic studies of laser pulse evolution, for the most part, are limited to the linear regime in which, for example, analytic expressions for instability growth rates are readily obtained. The self-consistent problem of plasma wave generation by an evolving drive laser pulse is typically of sufficient complexity as to require numerical simulation. Self-consistent simulations of plasma-based accelerators have been performed in the 2D and 3D non-linear regime using both fluid and particle-in-cell codes.

To generate a high-quality electron bunch, it is highly desirable that a bunch be injected with a length short compared to  $\lambda_p$ . Due to the shortness of  $\lambda_p$  ( $\lesssim 100 \mu\text{m}$ ), this is not yet achievable using conventional photo-injectors, in which the production of femtosecond bunches is problematic. Alternatively, several novel methods for injecting electrons into a plasma wave using density transitions or additional laser pulses have been proposed. In particular, using ultrashort (short compared to  $\lambda_p$ ) laser pulses shows great promise, since the injection process can be controlled in detail by adjust-

ing the timing of the injection pulses with respect to the plasma wave phase, as well as by adjusting the injection pulse amplitude and duration. Once injected, it is important that the electron bunch be accelerated while maintaining high quality, e.g., maintaining a small energy spread and emittance. The issue of bunch quality has not been addressed in detail in this report, but this problem is being studied within the plasma-based accelerator community, primarily via simulations [177, 178].

Experimentally, several groups have measured ultra-high accelerating fields and accelerated electrons, as is summarized in Table I. Large accelerating fields have been measured directly from optical probing techniques or inferred from the measurement of accelerated electrons. To date, the largest accelerating fields (>200 GV/m [12]) and highest energy electrons (200 MeV [13]) have been produced in the self-modulated LWFA regime, in which the high plasma densities yield large wavebreaking fields. Except for the relativistic self-focusing and ponderomotive self-channeling effects present in the self-modulated regime, none of these accelerator experiments have used an external method for laser guiding. At lower intensities ( $< 10^{18}$  W/cm<sup>2</sup>), laser pulses have been guided over many Rayleigh lengths (up to  $45Z_R$  [145]) in preformed plasma channels, produced

either by capillary discharges or laser ionization and heating methods. The generation of large amplitude plasma waves and the subsequent acceleration of electrons within a preformed plasma channel have yet to be demonstrated. If a plasma channel is used in conjunction with an ultra-high intensity laser pulse in the standard LWFA configuration, then linear theory predicts a maximum single-stage energy gain of  $\Delta W(\text{GeV}) \simeq I_0(\text{W}/\text{cm}^2)/n_0(\text{cm}^{-3})$ . Hence, a picosecond laser pulse with an intensity of  $10^{18} \text{W}/\text{cm}^2$  in a plasma of density  $10^{16} \text{cm}^{-3}$  may provide a single-stage energy gain as high as 100 GeV.

### Acknowledgments

The authors acknowledge many insightful conversations with the members of the LOASIS Group (in particular Wim Leemans) at LBNL and many of the researchers in the plasma-based accelerator community.

This work was supported by the U.S. Department of Energy under Contract No. DE-AC03-76SF0098.

- 
- [1] T. Tajima and J. M. Dawson, *Phys. Rev. Lett.* **43**, 267 (1979).
  - [2] C. Joshi, W. B. Mori, T. Katsouleas, J. M. Dawson, J. M. Kindel, and D. W. Forslund, *Nature* **311**, 525 (1984).
  - [3] S. C. Wilks, J. M. Dawson, W. B. Mori, T. Katsouleas, and M. E. Jones, *Phys. Rev. Lett.* **62**, 2600 (1989).
  - [4] J. M. Dawson, *Rev. Mod. Phys.* **55**, 403 (1983).
  - [5] W. B. Mori, C. Joshi, J. M. Dawson, D. W. Forslund, and J. M. Kindel, *Phys. Rev. Lett.* **60**, 1298 (1988).
  - [6] C. K. Birdsall, A. B. Langdon, V. Vehedi, and J. P. Verboncoeur, *Plasma Physics via Computer Simulations* (Adam Hilger, Bristol, Eng., 1991).
  - [7] C. E. Clayton and P. Muggli, eds., *Advanced Accelerator Concepts*, vol. 647 (AIP, New York, 2002).
  - [8] P. Maine, D. Strickland, P. Bado, M. Pessot, and G. Mourou, *IEEE J. Quantum Electron.* **QE-24**, 398 (1988).
  - [9] G. Mourou and D. Umstadter, *Phys. Fluids B* **4**, 2315 (1992).
  - [10] M. D. Perry and G. Mourou, *Science* **264**, 917 (1994).
  - [11] J. M. Dawson, *Phys. Rev.* **113**, 383 (1959).
  - [12] D. Gordon, K.-C. Tzeng, C. E. Clayton, A. E. Dangler, V. Malka, K. A. Marsh, A. Modena, W. B. Mori, P. Muggli, Z. Najmudin, et al., *Phys. Rev. Lett.* **80**, 2133 (1998).
  - [13] V. Malka, S. Fritzler, E. Lefebvre, M.-M. Leonard, F. Burgy, J.-P. Chambaret, J.-F. Chemin, K. Krushelnick, G. Malka, S. P. D. Mangles, et al., *Science* **298**, 1596 (2002).
  - [14] E. Esarey, P. Sprangle, and J. Krall, *Phys. Rev. E* **52**, 5443 (1995).
  - [15] P. Sprangle, E. Esarey, and J. Krall, *Phys. Plasmas* **3**, 2183 (1996).
  - [16] P. M. Woodward, *J. Inst. Electr. Eng.* **93**, 1554 (1947).
  - [17] J. D. Lawson, *IEEE Trans. Nucl. Sci.* **NS-26**, 4217 (1979).
  - [18] R. B. Palmer, *Part. Accel.* **11**, 81 (1980).
  - [19] Y. C. Huang and R. L. Byer, *Appl. Phys. Lett.* **69**, 2175 (1996).
  - [20] W. D. Kimura, G. H. Kim, R. D. Romea, L. C. Steinhauer, I. V. Pogorelsky, K. P. Kusche, R. C. Fernow, X. Wang, and Y. Liu, *Phys. Rev. Lett.* **74**, 546 (1995).
  - [21] P. Sprangle, E. Esarey, and J. Krall, *Phys. Rev. E* **54**, 4211 (1996).
  - [22] B. Quesnel and P. Mora, *Phys. Rev. E* **58**, 3719 (1998).
  - [23] G. V. Stupakov and M. S. Zolotarev, *Phys. Rev. Lett.* **86**, 5274 (2001).
  - [24] G. Malka, E. Lefebvre, and J. L. Miquel, *Phys. Rev. Lett.* **78**, 3314 (1997).
  - [25] J. Pang, Y. K. Ho, X. Q. Yuan, N. Cao, Q. Kong, P. X. Wang, L. Shao, E. H. Esarey, and A. M. Sessler, *Phys. Rev. E* **66**, 066501 (2002).
  - [26] Y. Liu, X. J. Wang, D. B. Cline, M. Babzien, J. M. Fang, J. Gallardo, K. Kusche, I. Pogorelsky, J. Skaritka, and A. van Steenbergen, *Phys. Rev. Lett.* **80**, 4418 (1998).
  - [27] W. D. Kimura, A. van Steenbergen, M. Babzien, I. Ben-Zvi, L. P. Campbell, D. B. Cline, C. E. Dille, J. C. Gallardo, S. C. Gottschalk, P. He, et al., *Phys. Rev. Lett.* **86**, 4041 (2001).
  - [28] Y. Kitagawa, T. Matsumoto, T. Minamihata, K. Sawai, K. Matsuo, K. Mima, K. Nishihara, H. Azechi, K. A. Tanaka, H. Takabe, et al., *Phys. Rev. Lett.* **68**, 48 (1992).
  - [29] C. E. Clayton, M. J. Everett, A. Lal, D. Gordon, K. A. Marsh, and C. Joshi, *Phys. Plasmas* **1**, 1753 (1994).
  - [30] N. A. Ebrahim, *J. Appl. Phys.* **76**, 7645 (1994).
  - [31] F. Amiranoff, D. Bernard, B. Cros, F. Jacquet, G. Matthieussent, P. Miné, P. Mora, J. Morillo, F. Moulin, A. E. Specka, et al., *Phys. Rev. Lett.* **74**, 5220 (1995).
  - [32] L. M. Gorbunov and V. I. Kirsanov, *Sov. Phys. JETP* **66**, 290 (1987).
  - [33] P. Sprangle, E. Esarey, A. Ting, and G. Joyce, *Appl. Phys. Lett.* **53**, 2146 (1988).
  - [34] H. Dewa, H. Ahn, H. Harano, M. Kando, K. Kinoshita, S. Kondoh, H. Kotaki, K. Nakajima, H. Nakanishi, et al., *Nucl. Instrum. Methods Phys. Res. A* **410**, 357 (1998).
  - [35] F. Amiranoff, S. Baton, D. Bernard, B. Cros, D. Descamps, L. F. Dorchies, F. Jacquet, V. Malka, J. Marquès, G. Matthieussent, et al., *Phys. Rev. Lett.* **81**, 995 (1998).
  - [36] P. Sprangle, E. Esarey, J. Krall, and G. Joyce, *Phys. Rev. Lett.* **69**, 2200 (1992).
  - [37] T. M. Antonsen, Jr. and P. Mora, *Phys. Rev. Lett.* **69**, 2204 (1992).
  - [38] N. E. Andreev, L. M. Gorbunov, V. I. Kirsanov, A. A. Pogosova, and R. R. Ramazashvili, *Pis'ma Zh. Eksp. Teor. Fiz.* **55**, 551 (1992).
  - [39] C. Joshi, T. Tajima, J. M. Dawson, H. A. Baldis, and N. A. Ebrahim, *Phys. Rev. Lett.* **47**, 1285 (1981).
  - [40] C. A. Coverdale, C. B. Darrow, C. D. Decker, W. B. Mori, K. Tzeng, K. A. Marsh, C. E. Clayton, and

- C. Joshi, *Phys. Rev. Lett.* **74**, 4659 (1995).
- [41] A. Modena, Z. Najmudin, A. E. Dangor, C. E. Clayton, K. A. Marsh, C. Joshi, V. Malka, C. B. Darrow, C. Danson, D. Neely, et al., *Nature* **377**, 606 (1995).
- [42] R. Wagner, S.-Y. Chen, A. Maksimchuk, and D. Umstadter, *Phys. Rev. Lett.* **78**, 3125 (1997).
- [43] C. I. Moore, A. Ting, K. Krushelnick, E. Esarey, R. F. Hubbard, B. Hafizi, H. R. Burris, C. Manka, and P. Sprangle, *Phys. Rev. Lett.* **79**, 3909 (1997).
- [44] W. P. Leemans, D. Rodgers, P. E. Catravas, C. G. R. Geddes, G. Fubiani, E. Esarey, B. A. Shadwick, R. Donahue, and A. Smith, *Phys. Plasmas* **8**, 2510 (2001).
- [45] V. Malka, J. Faure, J. R. Marquès, F. Amiranoff, J. P. Rousseau, S. Ranc, J. P. Chambaret, Z. Najmudin, B. Walton, P. Mora, et al., *Phys. Plasmas* **8**, 2605 (2001).
- [46] V. I. Berezhiani and I. G. Murusidze, *Physica Scripta* **45**, 87 (1992).
- [47] K. Nakajima, *Phys. Rev. A* **45**, 1149 (1992).
- [48] D. Umstadter, E. Esarey, and J. Kim, *Phys. Rev. Lett.* **72**, 1224 (1994).
- [49] S. Dalla and M. Lontano, *Phys. Rev. E* **49**, R1819 (1994).
- [50] G. Bonnaud, D. Teychenné, and J. Bobin, *Phys. Rev. E* **50**, R36 (1994).
- [51] W. L. Kruer, *The Physics of Laser Plasma Interactions* (Addison-Wesley, Redwood City, 1988).
- [52] E. Esarey, P. Sprangle, J. Krall, A. Ting, and G. Joyce, *Phys. Fluids B* **5**, 2690 (1993).
- [53] X. L. Chen and R. N. Sudan, *Phys. Fluids B* **5**, 1336 (1993).
- [54] E. Esarey, A. Ting, P. Sprangle, and G. Joyce, *Comments Plasma Phys. Controlled Fusion* **12**, 191 (1989).
- [55] W. K. H. Panofsky and W. A. Wenzel, *Rev. Sci. Instrum.* **27**, 967 (1956).
- [56] R. Keinings and M. E. Jones, *Phys. Fluids* **30**, 252 (1987).
- [57] E. Esarey, A. Ting, P. Sprangle, D. Umstadter, and X. Liu, *IEEE Trans. Plasma Sci.* **21**, 95 (1993).
- [58] D. Teychenné, G. Bonnaud, and J. Bobin, *Phys. Rev. E* **48**, R3248 (1993).
- [59] S. V. Bulanov, V. I. Kirsanov, and A. S. Sakharov, *JETP Lett.* **50**, 198 (1989).
- [60] P. Sprangle, E. Esarey, and A. Ting, *Phys. Rev. Lett.* **64**, 2011 (1990).
- [61] P. Sprangle, E. Esarey, and A. Ting, *Phys. Rev. A* **41**, 4463 (1990).
- [62] V. I. Berezhiani and I. G. Murusidze, *Phys. Lett. A* **148**, 338 (1990).
- [63] K.-C. Tzeng, W. B. Mori, and C. D. Decker, *Phys. Rev. Lett.* **76**, 3332 (1996).
- [64] A. Pukhov and J. Meyer-ter-Vehn, *Phys. Rev. Lett.* **76**, 3975 (1996).
- [65] P. Mora and T. M. Antonsen, Jr., *Phys. Plasmas* **4**, 217 (1997).
- [66] C. Ren, R. G. Hemker, R. A. Fonseca, B. J. Duda, and W. B. Mori, *Phys. Rev. Lett.* **85**, 2124 (2000).
- [67] A. I. Akhiezer and R. V. Polovin, *Zh. Eksp. Teor. Fiz.* **30**, 915 (1956).
- [68] E. Esarey and M. Pilloff, *Phys. Plasmas* **2**, 1432 (1995).
- [69] T. Katsouleas and W. B. Mori, *Phys. Rev. Lett.* **61**, 90 (1989).
- [70] J. B. Rosenzweig, *Phys. Rev. A* **38**, 3634 (1988).
- [71] C. D. Decker, W. B. Mori, and T. Katsouleas, *Phys. Rev. E* **50**, R3338 (1994).
- [72] S. V. Bulanov, F. Pegoraro, and A. M. Pukhov, *Phys. Rev. Lett.* **74**, 710 (1995).
- [73] J. Krall, A. Ting, E. Esarey, and P. Sprangle, *Phys. Rev. E* **48**, 2157 (1993).
- [74] S. V. Bulanov, F. Pegoraro, A. M. Pukhov, and A. S. Sakharov, *Phys. Rev. Lett.* **78**, 4205 (1997).
- [75] M. N. Rosenbluth and C. S. Liu, *Phys. Rev. Lett.* **29**, 701 (1972).
- [76] C. M. Tang, P. Sprangle, and R. N. Sudan, *Phys. Fluids* **28**, 1974 (1985).
- [77] P. Mora, *Phys. Fluids B* **4**, 1630 (1992).
- [78] D. Teychenné, G. Bonnaud, and J.-L. Bobin, *Phys. Rev. E* **49**, 3253 (1994).
- [79] C. D. Decker and W. B. Mori, *Phys. Rev. Lett.* **72**, 490 (1994).
- [80] E. Esarey and W. P. Leemans, *Phys. Rev. E* **59**, 1082 (1999).
- [81] W. P. Leemans, C. W. Siders, E. Esarey, N. E. Andreev, G. Shvets, and W. B. Mori, *IEEE Trans. Plasma Sci.* **24**, 331 (1996).
- [82] E. Esarey, A. Ting, and P. Sprangle, *Phys. Rev. A* **42**, 3526 (1990).
- [83] J. R. Marquès, J. P. Geindre, F. Amiranoff, P. Audebert, J. C. Gauthier, A. Antonetti, and G. Grillon, *Phys. Rev. Lett.* **76**, 3566 (1996).
- [84] C. W. Siders, S. P. Le Blanc, D. Fisher, T. Tajima, M. C. Downer, A. Babine, A. Stepanov, and A. Sergeev, *Phys. Rev. Lett.* **76**, 3570 (1996).
- [85] H. Hamster, A. Sullivan, S. Gordon, W. White, and R. W. Falcone, *Phys. Rev. Lett.* **71**, 2725 (1993).
- [86] D. Bernard, F. Amiranoff, W. P. Leemans, E. Esarey, and C. Joshi, *Nucl. Instrum. Methods Phys. Res. A* **432**, 227 (1999).
- [87] C. E. Clayton, K. A. Marsh, A. Dyson, M. Everett, A. Lal, W. P. Leemans, R. Williams, and C. Joshi, *Phys. Rev. Lett.* **70**, 37 (1993).
- [88] M. Everett, A. Lal, D. Gordon, C. E. Clayton, K. A. Marsh, and C. Joshi, *Nature* **368**, 527 (1994).
- [89] W. Horton and T. Tajima, *Phys. Rev. A* **34**, 4110 (1986).
- [90] C. J. McKinstrie and D. W. Forslund, *Phys. Fluids* **30**, 904 (1987).
- [91] E. Esarey, A. Ting, and P. Sprangle, *Appl. Phys. Lett.* **53**, 1266 (1988).
- [92] P. Gibbon and A. R. Bell, *Phys. Rev. Lett.* **61**, 1599 (1988).
- [93] T. Katsouleas and J. M. Dawson, *Phys. Rev. Lett.* **51**, 392 (1983).
- [94] E. Esarey and A. Ting, *Phys. Rev. Lett.* **65**, 1961 (1990).
- [95] D. Umstadter, J. Kim, E. Esarey, E. Dodd, and T. Neubert, *Phys. Rev. E* **51**, 3484 (1995).
- [96] F. Amiranoff, M. Laberge, J. R. Marquès, F. Moulin, E. Fabre, B. Cros, G. Matthieussent, P. Benkheiri, F. Jacquet, J. Meyer, et al., *Phys. Rev. Lett.* **68**, 3710 (1992).
- [97] C. E. Clayton, C. Joshi, C. Darrow, and D. Umstadter, *Phys. Rev. Lett.* **54**, 2343 (1985).
- [98] M. J. Everett, A. Lal, C. E. Clayton, W. B. Mori, T. W. Johnston, and C. Joshi, *Phys. Rev. Lett.* **74**, 2236 (1995).
- [99] W. P. Leemans, C. E. Clayton, K. A. Marsh, and C. Joshi, *Phys. Rev. Lett.* **67**, 1434 (1991).

- [100] W. P. Leemans, C. E. Clayton, W. B. Mori, K. A. Marsh, P. K. Kaw, A. Dyson, C. Joshi, and J. M. Wallace, *Phys. Rev. A* **46**, 1091 (1992).
- [101] X. Liu, R. Wagner, A. Maksimchuk, E. Goodman, J. Workman, U. D. and A. Migus, *Opt. Lett.* **20**, 1163 (1995).
- [102] K. Nakajima, D. Fisher, T. Kawakubo, H. Nakanishi, A. Ogata, Y. Kato, Y. Kitagawa, R. Kodama, K. Mima, H. Shiraga, et al., *Phys. Rev. Lett.* **74**, 4428 (1995).
- [103] W. P. Leemans, P. Catravas, E. Esarey, C. G. R. Geddes, C. Toth, R. Trines, C. B. Schroeder, B. A. Shadwick, J. van Tilborg, and J. Faure, *Phys. Rev. Lett.* **89**, 174802 (2002).
- [104] E. Esarey, J. Krall, and P. Sprangle, *Phys. Rev. Lett.* **72**, 2887 (1994).
- [105] W. B. Mori, C. D. Decker, D. E. Hinkel, and T. Katsouleas, *Phys. Rev. Lett.* **72**, 1482 (1994).
- [106] T. M. Antonsen, Jr. and P. Mora, *Phys. Fluids B* **5**, 1440 (1993).
- [107] N. E. Andreev, L. M. Gorbunov, V. I. Kirsanov, A. A. Pogosova, and R. R. Ramazashvili, *Physica Scripta* **49**, 101 (1994).
- [108] N. E. Andreev, V. I. Kirsanov, and L. M. Gorbunov, *Phys. Plasmas* **2**, 2573 (1995).
- [109] A. Ting, K. Krushelnick, C. I. Moore, H. R. Burris, E. Esarey, J. Krall, and P. Sprangle, *Phys. Rev. Lett.* **77**, 5377 (1996).
- [110] C. B. Schroeder, E. Esarey, C. G. R. Geddes, C. Tóth, B. A. Shadwick, J. van Tilborg, J. Faure, and W. P. Leemans, *Phys. Plasmas* **10**, 2039 (2003).
- [111] A. Pukhov, Z.-M. Sheng, and J. Meyer-ter-Vehn, *Phys. Plasmas* **6**, 2847 (1999).
- [112] D. H. Whittum, A. M. Sessler, and J. M. Dawson, *Phys. Rev. Lett.* **64**, 2511 (1990).
- [113] E. Esarey, B. A. Shadwick, P. Catravas, and W. P. Leemans, *Phys. Rev. E* **65**, 056505 (2002).
- [114] C. Gahn, G. D. Tsakiris, A. Pukhov, J. Meyer-ter-Vehn, G. Pretzler, P. Thirolf, D. Habs, and K. J. Witte, *Phys. Rev. Lett.* **83**, 4772 (1999).
- [115] A. Ting, E. Esarey, and P. Sprangle, *Phys. Fluids B* **2**, 1390 (1990).
- [116] S. V. Bulanov, I. N. Inovenkov, V. I. Kirsanov, N. M. Naumova, and A. S. Sakharov, *Phys. Fluids B* **4**, 1935 (1992).
- [117] D. Teychenné, G. Bonnaud, and J.-L. Bobin, *Phys. Plasmas* **1**, 1771 (1994).
- [118] D. L. Fisher, T. Tajima, M. C. Downer, and C. W. Siders, *Phys. Rev. E* **51**, 4860 (1995).
- [119] P. Sprangle and E. Esarey, *Phys. Fluids B* **4**, 2241 (1992).
- [120] E. Esarey, P. Sprangle, J. Krall, and A. Ting, *IEEE Trans. Plasma Sci.* **24**, 252 (1996).
- [121] P. Sprangle, B. Hafizi, J. R. Peñano, R. F. Hubbard, A. Ting, C. I. Moore, D. F. Gordon, A. Zigler, D. Kaganovich, and T. M. Antonsen, Jr., *Phys. Rev. E* **63**, 056405 (2001).
- [122] T. Katsouleas, S. Wilks, P. Chen, J. M. Dawson, and J. J. Su, *Part. Accel.* **22**, 81 (1987).
- [123] K.-C. Tzeng, W. B. Mori, and T. Katsouleas, *Phys. Rev. Lett.* **79**, 5258 (1997).
- [124] E. Esarey, B. Hafizi, R. Hubbard, and A. Ting, *Phys. Rev. Lett.* **80**, 5552 (1998).
- [125] C. Rousseaux, G. Malka, J. L. Miquel, F. Amiranoff, S. D. Baton, and P. Mounaix, *Phys. Rev. Lett.* **74**, 4655 (1995).
- [126] P. Bertrand, A. Ghizzo, S. J. Karttunen, T. J. H. Pättikangas, R. R. E. Salomaa, and M. Shoucri, *Phys. Plasmas* **2**, 3115 (1995).
- [127] A. J. W. Reitsma, W. P. Leemans, E. Esarey, C. B. Schroeder, L. P. J. Kamp, and T. J. Schep, *Phys. Rev. ST Accel. Beams* **5**, 051301 (2002).
- [128] D. Umstadter, J. K. Kim, and E. Dodd, *Phys. Rev. Lett.* **76**, 2073 (1996).
- [129] E. Esarey, R. F. Hubbard, W. P. Leemans, A. Ting, and P. Sprangle, *Phys. Rev. Lett.* **79**, 2682 (1997).
- [130] R. G. Hemker, K.-C. Tzeng, W. B. Mori, C. E. Clayton, and T. Katsouleas, *Phys. Rev. E* **57**, 5920 (1998).
- [131] C. B. Schroeder, P. B. Lee, J. S. Wurtele, E. Esarey, and W. P. Leemans, *Phys. Rev. E* **59**, 6037 (1999).
- [132] C. I. Moore, A. Ting, S. J. McNaught, J. Qiu, H. R. Burris, and P. Sprangle, *Phys. Rev. Lett.* **82**, 1688 (1999).
- [133] E. Esarey, C. B. Schroeder, W. P. Leemans, and B. Hafizi, *Phys. Plasmas* **6**, 2262 (1999).
- [134] W. P. Leemans, P. Volfbeyn, K. Z. Guo, S. Chattopadhyay, C. B. Schroeder, B. A. Shadwick, P. B. Lee, J. S. Wurtele, and E. Esarey, *Phys. Plasmas* **5**, 1615 (1998).
- [135] S. Bulanov, N. Naumova, F. Pegoraro, and J. Sakai, *Phys. Rev. E* **58**, R5257 (1998).
- [136] H. Suk, N. Barov, J. B. Rosenzweig, and E. Esarey, *Phys. Rev. Lett.* **86**, 1011 (2001).
- [137] J. Krall, E. Esarey, P. Sprangle, and G. Joyce, *Phys. Plasmas* **1**, 1738 (1994).
- [138] A. G. Litvak, *Zh. Eksp. Teor. Fiz.* **57**, 629 (1969).
- [139] C. Max, J. Arons, and A. B. Langdon, *Phys. Rev. Lett.* **33**, 209 (1974).
- [140] G. Z. Sun, E. Ott, Y. C. Lee, and P. Guzdar, *Phys. Fluids* **30**, 526 (1987).
- [141] P. Sprangle, C. M. Tang, and E. Esarey, *IEEE Trans. Plasma Sci.* **PS-15**, 145 (1987).
- [142] L. C. Steinhauer and H. G. Ahlstrom, *Phys. Fluids* **14**, 1109 (1971).
- [143] L. C. Johnson and T. K. Chu, *Phys. Rev. Lett.* **32**, 517 (1974).
- [144] C. G. Durfee III and H. M. Milchberg, *Phys. Rev. Lett.* **71**, 2409 (1993).
- [145] C. G. Durfee III, J. Lynch, and H. M. Milchberg, *Phys. Rev. E* **51**, 2368 (1995).
- [146] P. Volfbeyn, E. Esarey, and W. Leemans, *Phys. Plasmas* **6**, 2269 (1999).
- [147] E. W. Gaul, S. P. Le Blanc, A. R. Rundquist, R. Zgadzaj, H. Langhoff, and M. C. Downer, *Appl. Phys. Lett.* **77**, 4112 (2000).
- [148] T. KurkiSuonio, P. J. Morrison, and T. Tajima, *Phys. Rev. A* **40**, 3230 (1989).
- [149] P. Sprangle, A. Ting, and C. M. Tang, *Phys. Rev. A* **36**, 2773 (1987).
- [150] P. Sprangle, J. Krall, and E. Esarey, *Phys. Rev. Lett.* **73**, 3544 (1994).
- [151] G. Shvets and J. S. Wurtele, *Phys. Rev. Lett.* **73**, 3540 (1994).
- [152] K. Krushelnick, A. Ting, C. I. Moore, H. R. Burris, E. Esarey, P. Sprangle, and M. Baine, *Phys. Rev. Lett.* **78**, 4047 (1997).
- [153] A. Zigler, Y. Ehrlich, C. Cohen, J. Krall, and P. Sprangle, *J. Opt. Soc. Am. B.* **13**, 68 (1996).
- [154] Y. Ehrlich, C. Cohen, D. Kaganovich, A. Zigler, R. F. Hubbard, P. Sprangle, and E. Esarey, *J. Opt. Soc. Am. B* **15**, 2416 (1998).

- [155] S. M. Hooker, D. J. Spence, and R. A. Smith, *J. Opt. Soc. Am. B* **17**, 90 (2000).
- [156] T. Hosokai, M. Kando, H. Dewa, H. Kotaki, S. Kondo, N. Hasegawa, K. Nakajima, and K. Horioka, *Opt. Lett.* **25**, 10 (2000).
- [157] A. Butler, D. J. Spence, and S. M. Hooker, *Phys. Rev. Lett.* **89**, 185003 (2002).
- [158] F. Dorchies, J. R. Marquès, B. Cros, G. Matthieussent, C. Courtois, T. Vélikorousov, P. Audebert, J. P. Geindre, S. Rebibo, G. Hamoniaux, et al., *Phys. Rev. Lett.* **82**, 4655 (1999).
- [159] Y. Ehrlich, C. Cohen, A. Zigler, J. Krall, P. Sprangle, and E. Esarey, *Phys. Rev. Lett.* **77**, 4186 (1996).
- [160] T. M. Antonsen, Jr. and P. Mora, *Phys. Rev. Lett.* **74**, 4440 (1995).
- [161] T. C. Chiou, T. Katsouleas, C. Decker, W. B. Mori, G. Shvets, and J. S. Wurtele, *Phys. Plasmas* **2**, 310 (1995).
- [162] C. B. Schroeder, J. S. Wurtele, and D. H. Whittum, *Phys. Rev. Lett.* **82**, 1177 (1999).
- [163] G. Shvets, J. S. Wurtele, T. C. Chiou, and T. C. Katsouleas, *IEEE Trans. Plasma Sci.* **24**, 351 (1996).
- [164] P. Sprangle, A. Zigler, and E. Esarey, *Appl. Phys. Lett.* **58**, 346 (1991).
- [165] C. Joshi, C. E. Clayton, and F. F. Chen, *Phys. Rev. Lett.* **48**, 874 (1982).
- [166] E. Esarey and P. Sprangle, *Phys. Rev. A* **45**, 5872 (1992).
- [167] C. J. McKinstrie and R. Bingham, *Phys. Fluids B* **4**, 2626 (1992).
- [168] A. S. Sakharov and V. I. Kirsanov, *Phys. Rev. E* **49**, 3274 (1994).
- [169] C. Darrow, C. Coverdale, M. Perry, W. Mori, C. Clayton, K. Marsh, and C. Joshi, *Phys. Rev. Lett.* **69**, 442 (1992).
- [170] K. Krushelnick, C. I. Moore, A. Ting, and H. R. Burris, *Phys. Rev. Lett.* **58**, 4030 (1998).
- [171] C. D. Decker, W. B. Mori, K. Tzeng, and T. Katsouleas, *Phys. Plasmas* **3**, 2047 (1996).
- [172] A. Ting, C. I. Moore, K. Krushelnick, C. Manka, E. Esarey, P. Sprangle, R. Hubbard, H. R. Burris, R. Fischer, and M. Baine, *Phys. Plasmas* **4**, 1889 (1997).
- [173] C. B. Schroeder, E. Esarey, B. A. Shadwick, and W. P. Leemans, *Phys. Plasmas* **10**, 285 (2003).
- [174] W. B. Mori, *IEEE J. Quantum Electron.* **33**, 1942 (1997).
- [175] C. D. Decker, W. B. Mori, T. Katsouleas, and D. E. Hinkel, *Phys. Plasmas* **3**, 1360 (1996).
- [176] E. Esarey, C. B. Schroeder, B. A. Shadwick, J. S. Wurtele, and W. P. Leemans, *Phys. Rev. Lett.* **84**, 3081 (2000).
- [177] T. C. Chiou and T. Katsouleas, *Phys. Rev. Lett.* **81**, 3411 (1998).
- [178] A. J. W. Reitsma, V. V. Goloviznin, L. P. J. Kamp, and T. J. Schep, *Phys. Rev. E* **63**, 046502 (2001).